DESIGN, FABRICATION AND TESTING OF HIERARCHICAL MICRO-OPTICAL STRUCTURES AND SYSTEMS

by

Aaron Thomas Cannistra

A dissertation submitted to the faculty of
The University of North Carolina at Charlotte
in partial fulfillment of the requirements
for the degree of Doctor of Philosophy in
Optical Science and Engineering

Charlotte

2011

Approved by:

_____
Dr. Thomas J. Suleski

_____
Dr. Angela D. Davies

_____
Dr. Matt A. Davies

_____
Dr. Eric G. Johnson

ABSTRACT

AARON THOMAS CANNISTRA. Design, fabrication and testing of hierarchical micro-optical structures and systems. (Under the direction of DR. THOMAS J. SULESKI)

Micro-optical systems are becoming essential components in imaging, sensing, communications, computing, and other applications. Optically based designs are replacing electronic, chemical and mechanical systems for a variety of reasons, including low power consumption, reduced maintenance, and faster operation. However, as the number and variety of applications increases, micro-optical system designs are becoming smaller, more integrated, and more complicated. Micro and nano-optical systems found in nature, such as the imaging systems found in many insects and crustaceans, can have highly integrated optical structures that vary in size by orders of magnitude. These systems incorporate components such as compound lenses, anti-reflective lens surface structuring, spectral filters, and polarization selective elements. For animals, these hybrid optical systems capable of many optical functions in a compact package have been repeatedly selected during the evolutionary process. Understanding the advantages of these designs gives motivation for synthetic optical systems with comparable functionality. However, alternative fabrication methods that deviate from conventional processes are needed to create such systems. Further complicating the issue, the resulting device geometry may not be readily compatible with existing measurement techniques.

This dissertation explores several nontraditional fabrication techniques for optical components with hierarchical geometries and measurement techniques to evaluate performance of such components. A micro-transfer molding process is found to produce high-fidelity micro-optical structures and is used to fabricate a spectral filter on a curved

surface. By using a custom measurement setup we demonstrate that the spectral filter retains functionality despite the nontraditional geometry. A compound lens is fabricated using similar fabrication techniques and the imaging performance is analyzed. A spray coating technique for photoresist application to curved surfaces combined with interference lithography is also investigated. Using this technique, we generate polarizers on curved surfaces and measure their performance. This work furthers an understanding of how combining multiple optical components affects the performance of each component, the final integrated devices, and leads towards realization of biomimetically inspired imaging systems.

ACKNOWLEDGMENTS

I would like to thank my advisor, Dr. Thomas J. Suleski, and members of my committee, Dr. Angela D. Davies, Dr. Matt A. Davies and Dr. Eric G. Johnson for their guidance and support. I would like to thank my group members, Dr. Brent Bergner, Dr. Yi-Chen Chuang and Paul Smilie for their advice and assistance. I would also like to acknowledge many researchers and staff at UNCC and elsewhere including Bruce Dudley, Dr. Lou Deguzman, Scott Williams, Dr. Bob Hudgins, Alec Martin, Zack Roth, Dr. Menelaos Poutous and Dr. Raymond Rumpf. I would like to thank Dr. Pradeep Srinivasan in particular for his knowledge, training and assistance with fabrication. I would also like to thank TIAA-CREF, the Giles Foundation, HEL-JTO, and NSF for their financial support throughout my graduate studies.

DEDICATION

To the people that tolerate me calling them friends, to good beer, and to my girlfriend Kelly Nadler, because without them, what would be the point of all this other nonsense…

TABLE OF CONTENTS

CHAPTER 1: INTRODUCTION

1.1 Dissertation overview

Micro-optics have become a critical part of modern technology, performing an ever increasing range of functions in advanced devices. As the diversity and number of these functions continues to increase, more and increasingly complex functions are being integrated into optical designs. Biologically inspired optical devices with desired functions multiplexed into a single element provide a path to satisfy demands of future technology [1, 2]. However, realizing these elements has proven challenging for current methods [3-6].

In this dissertation we explore ways to use both established and experimental methods to address many of the challenges related to designing, fabricating and testing functional hierarchical optical devices. We have developed fabrication techniques that are used to generate multiple devices that serve as demonstrators of nontraditional hierarchical components. We discuss issues related to the applied techniques, and where significant challenges exist. Experimental results are presented and performance of the devices is evaluated.

1.2 Micro and nano-optics

Advances in technology for consumer, medical, industrial, commercial and military applications depend on improvements in performance, efficiency, size, and cost [7]. Optical components have long been used to compliment devices centered around other

technologies, but have more recently shown promise in becoming the dominant technology for many devices [8-10]. This is in part due to advances in micro-optics, optical elements made at the scale of a human hair or a speck of dust. Micro-optics encompass components from simple miniature refractive lenses to complicated diffractive designs that can control polarization, wavelength, reflectivity, beam profile, modal properties, and more. Many of these optical functions have been enabled by the ability to create structures smaller than the wavelength of light they are designed to manipulate. These subwavelength structures allow us to create artificial materials (or metamaterials) whose optical properties, such as refractive index, dispersion and birefringence, are structure dependent [11, 12]. Micro-optics have already proven to be indispensable components in micro-imaging, laser beam shaping, encryption, and integrated optics [13-16]. New applications are regularly being explored with examples ranging from non-intrusive medical diagnostic and treatment tools, to improved solar energy collection, to metamaterials that can create 'invisibility cloaks.' [17-19]. Micro-optics are replacing or eliminating the need for mechanical, electrical and chemical components in many systems due to their lack of moving parts, low power consumption and fast operation [20, 21]. Refractive microlenses serve as a simple, representative example. These structures alone are widely used in optical communications [13], digital displays, optical data storage, detectors for cameras, biological/biomedical systems [14], and miniaturized camera systems [15, 16].

1.3 Biomimetic inspiration

Hierarchical optics are optical devices that combine functional structures with varying size scales into a single element. These designs exemplify integration and

functionality, often improving performance and efficiency while simultaneously reducing the device footprint. Interest in hierarchical designs has increased with technological advances in needs for miniaturization. Despite this recent trend, these types of designs have been around for millions of years in the natural world [22]. For small biological optical structures, such as those found in insects, evolution has repeatedly chosen hierarchical designs in the form of compound eyes for good reason. For small invertebrates with an exoskeleton, the weight and metabolic energy costs of having any type of optical vision system is substantial [23]. To address and minimize this issue, nature has repeatedly chosen to distribute visual function over a large number of small imaging sub-components. Resolution of such systems is typically much lower than single lens systems. In these cases, however, this may be inconsequential as the image processing capability of the animal's small brain would otherwise be overwhelmed. Also, additional functionality of compound eye structures such as wide field of view (FOV), fast motion detection, and polarization selectivity help to offset resolution limitations [23]. Perhaps not surprisingly, the compound eye is the most common type of visual organ in animal species [24]. This is in part due to the large number of insect species who possess them, but they are also found in other animal types such as crustaceans [25]. Single lens systems inherently provide better resolution and sensitivity, but are typically found in larger vertebrates such as humans where size and weight are not as critical. Perhaps then, to address the size and weight restrictions of new applications, research should pursue optical designs with similar hierarchical concepts. Several specific examples that demonstrate desirable hierarchical optical functions include the fly eye, moth eye and mantis shrimp eye. We briefly discuss these examples below, restricting

ourselves to the most general cases of each. Detailed discussion accounting for differences found among species of each example would be an exhaustive endeavor, well beyond the scope of this dissertation.

A typical fly eye is an example of a relatively simple and straightforward compound eye. The primary function of the fly eye is to capture visual information in daylight from a wide field of view in a compact and lightweight package. To do this, an array of imaging sub-components are tightly packed as a non-uniform hexagonal lattice contoured over a roughly spherical shell [23], as shown in Fig. 1.1 (image shown is of conceptually similar bee eye). The individual imaging components are made up of a micro-lens cap, a crystalline cone and a photoreceptor [2]. Together these are called an *ommatidium* as seen in Fig. 1.2. In the case of a diurnally active fly, the most common arrangement will be of an apposition compound eye. For an apposition fly eye, each ommatidium is structured to capture and partially focus light incident on the lens cap, then transmit and focus the light through the graded refractive index cone to a photoreceptor at the interior end of the structure. The brain combines the information from each ommatidium to form an image, facilitating fast motion detection with limited processing [23]. This structure has limitations in number of photons captured and resulting sensitivity of each individual ommatidium. However, achieving the nearly panoramic field of view of some insect species, and compact design with eye sizes often below 1 mm in diameter, is a significant challenge for other imaging systems [23, 26].

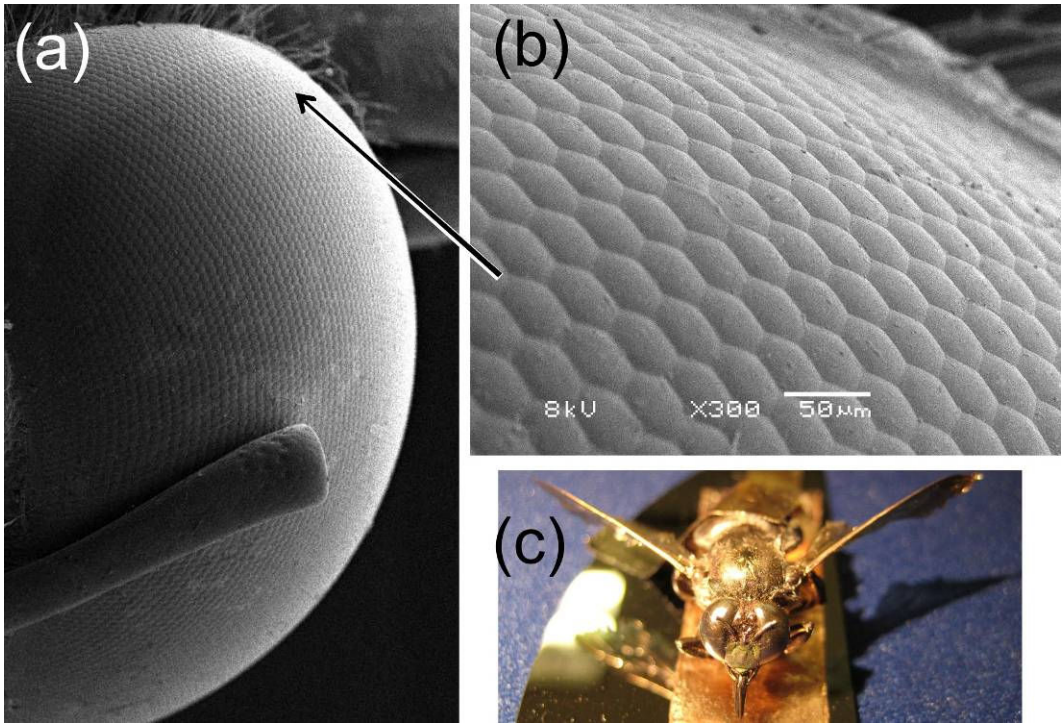

Fig. 1.1. (a) SEM image of bee eye, showing array of ommatidia arranged for wide FOV. (b) Close up of hexagonally packed lenses (c) Camera image of bee coated with a thin layer of gold for SEM.

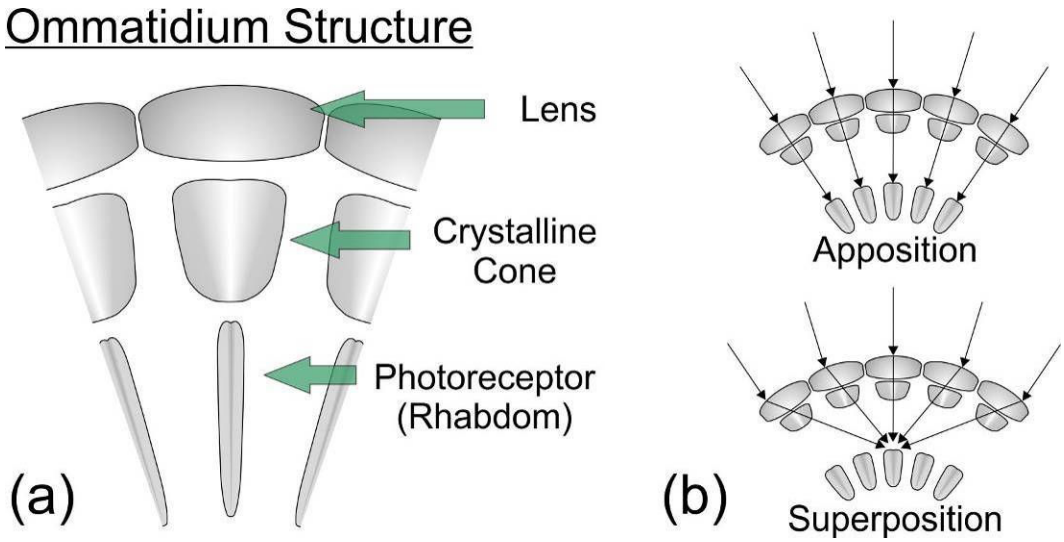

Fig. 1.2. Ommatidium structure for compound eyes common to insects and crustaceans. (a) The lens and graded index crystalline cone focus light onto a photoreceptor. A large number of tightly packed ommatidia are arranged over a curved surface to form the eye. (b) In the apposition configuration, each lens and cone are paired with a specific photoreceptor. For the superposition configuration, light from multiple lens/cone pairs are focused on a single photoreceptor.

A moth eye is very similar to the fly eye structure, as it shares an array of ommatidia in a compound eye arrangement. However, the nocturnal moth's eye uses a superposition

configuration, rather than the apposition eye found in most flies and other diurnal insects [27]. Unlike the apposition eye that dedicates a specific photoreceptor to each lens/cone unit, a superposition compound eye directs light focused by several lens/cone units onto a single photoreceptor. This design can significantly increase the light sensitivity, leading it to be primarily found in nocturnal insects and deepwater crustaceans [1]. Perhaps more interesting is the additional level of structural integration found in eyes of many species of moth. In these species, the surface of each ommatidium is covered by what essentially is a two dimensional subwavelength grating called a "nipple array" [28] as seen in Fig. 1.3. These structures provide a gradient refractive index at the surface of the microlenses, thereby reducing reflection from the eye. Although this could certainly benefit the moth's ability to see, it is believed that the primary function of these structures is to help reduce glare from the eyes. This is believed to be a defense mechanism intended to reduce visibility to would-be predators [28]. To further this argument, similar nipple array patterns found in diurnal butterflies (a probable moth ancestor) are significantly reduced in prominence reducing their function as an AR coating.

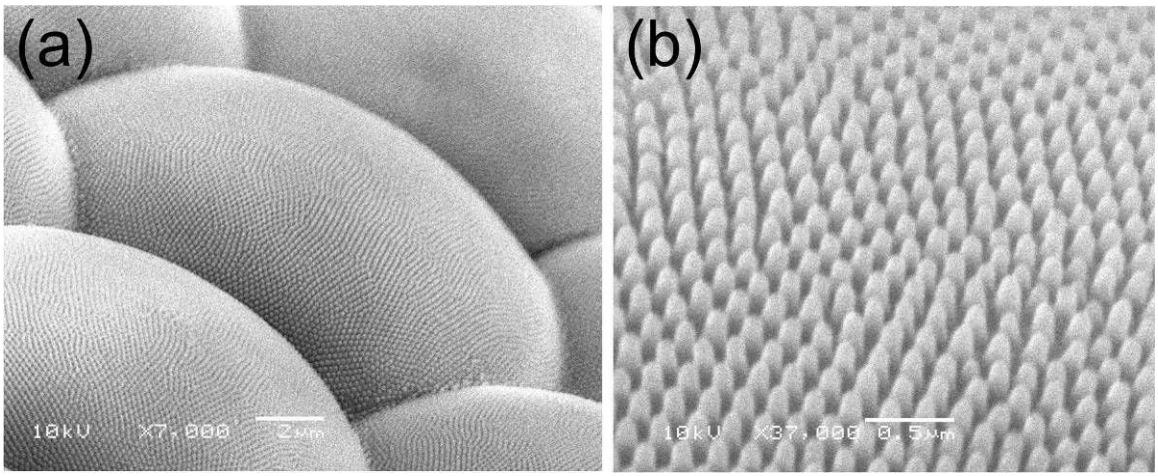

Fig. 1.3. (a) SEM image of moth ommatidium lens cap and (b) close up of nipple array that covers lens surface. The small protrusions function as an AR coating.

Another example of sophisticated and integrated designs for sensing and imaging is the mantis shrimp's vision system, shown in Fig. 1.4 [29]. Continuing with the theme of compound eyes, the mantis shrimp has an apposition configuration due his primary habitat being the well lit shallow water of tropical coral reefs [30]. However, this stomatopod has a highly sophisticated optical system, one of the most sophisticated found in nature. In this discussion, we consider mantis shrimp from the two superfamilies Gonodactyloidea and Lysiosquilloidea. These mantis shrimp possess differentiated ommatidia with varying size, structure and internal composition to perform specialized functions such as color vision, increased resolution or sensitivity, and polarization-selective vision [31]. The eye has 12 independent color channels spread over the wavelength range from 300 to 720 nm with spectral half bandwidths around 20 nm wide, some of the sharpest found in the animal kingdom. This level of hyperspectral color imaging is accomplished through pigment based filtering elements and a large number of wavelength specific photoreceptors. Vision capable of detecting linear and circular polarization is accomplished with anisotropically structured photoreceptor cells with differentiated cells for the various polarization states [29]. Advanced color and polarization detection occurs primarily in the mid-band of the mantis shrimp eye, a band of enlarged ommatidia facets separating the eye into two hemispheres. The larger lens facets in this region offset sensitivity reduction inherent in the specialized features found here to ensure sensitivity remains relatively uniform over all regions of the eye [31]. Although the reasons for such complexity and advanced imaging in this stomatopod are not fully understood, it is apparent the mantis shrimp's vision system enhances its ability

to see threats, acquire targets, and communicate, all in a compact package with reduced image processing.

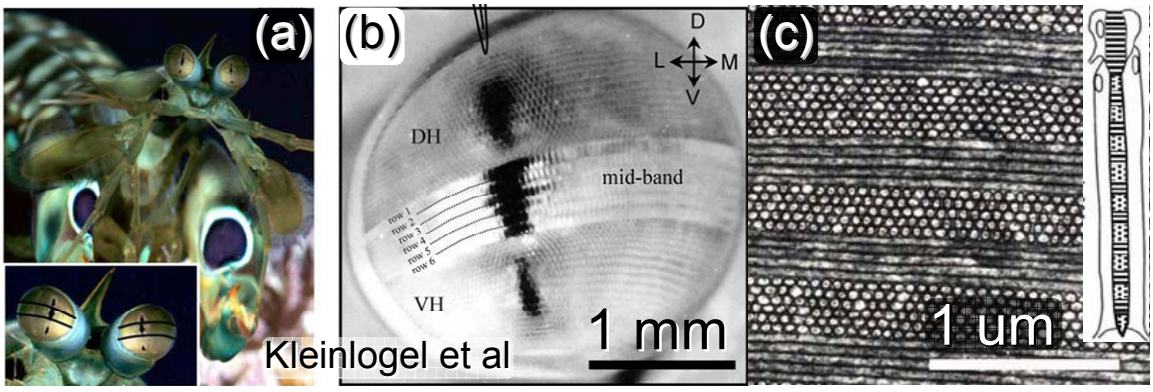

Fig. 1.4. (a) Mantis shrimp are known for their highly sophisticated eyes as shown in this figure by Kleinlogel et al. They have specialized optical functions in their equatorial mid-band shown by dark lines (inset) and (b) shown in more detail. The mid-band has enlarged ommatidium facets coupled with polarization and spectral filtering capability. (c) Electron micrograph of a longitudinal cross section of a polarization selective photoreceptor is shown with diagram of photoreceptor configuration inset [29].

These examples illustrate the wide range of solutions nature has provided to accomplish different optical functions in compact packages. Although our ability to fabricate components that exactly mirror these biological designs may be limited, these designs highlight some of the realizable advantages of borrowing from hierarchical optical concepts found in nature.

1.4 Optical modeling and challenges for hierarchical optics

Regardless of what inspires us, we rely on technology to turn a conceptual idea into a functioning device. This process begins with optical design. Optical design is essential to predict behavior prior to fabrication, and to understand and correct issues or limitations of the device after fabrication. For traditional refractive and reflective optics much larger than the involved wavelengths, geometric optical modeling software such as ZEMAX™, the package used in this dissertation, can provide the majority of relevant information

[32]. However, for smaller structures on the scale of the wavelength involved, diffraction and guided-wave effects play a larger role, so geometrical approaches do not adequately predict behavior. For these structures, many numerical modeling methods have been developed, however we restrict ourselves to two relevant examples. Rigorous coupled wave analysis (RCWA), is a commonly used technique for numerically modeling scattering from periodic structures, chosen for its speed and efficiency [33]. RCWA is a frequency domain method able to handle oblique angles of incidence and shown to be very stable. In this dissertation we implement RCWA through the commercially available software package G-Solver™, and through code written by Rumpf et al. in MATLAB [33-35]. Finite difference time domain (FDTD) is another popular modeling technique. One strength of FDTD results from its time-based calculation of the electric and magnetic fields at all points over the simulation space, giving it the ability to output visualizations of the electromagnetic fields [36]. Also, because it is a time domain method, a single simulation can characterize a device over a wide range of wavelengths.

The challenges of modeling hierarchical structures result from the need to simultaneously model the optical effects of structures that vary in size by orders of magnitude. RCWA is an excellent method for modeling wavelength-scale periodic structures that may provide additional functions to curved surfaces. However, RCWA is restricted to models of these structures on a flat surface due to requirements that structures be broken down into layers uniform in the direction normal to the propagating wave [33]. This is not an issue for continuously varying periodic structures, as they can be broken down into any number of layers to best approximate and model the structure. However, the very nature of hierarchical devices suggests non-periodic structural

variation (or at the minimum, structures whose periodicity is on a different scale) in each of these layers in addition to any periodic structure, restricting its use for hierarchical designs. Despite these limitations, RCWA is an attractive simulation method, and was the primary method for modeling subwavelength structures in this dissertation. We discuss how we applied this technique to structures fabricated on curves in later chapters. FDTD is capable of handling hierarchical structures, but can be computationally intensive with significant processing requirements for large three dimensional geometries [36]. Although not used in this dissertation, techniques such as FDTD may be necessary for more accurate simulation of true 3D structures.

1.5 Optical fabrication and challenges for hierarchical optics

After a device has been designed the next step in creating a functioning device is fabrication. Historically, optics have consisted of macro-scale elements with smooth surfaces intended to refract or reflect light. The fabrication processes for these elements most often use grinding and polishing to physically remove material by contact with a dynamic and abrasive surface on the scale of the optic being made [37]. Because both flats and spheres have symmetrical curvature over their surface (assuming infinite radius of curvature for the flat), an abrasive surface in the inverse of the desired optical shape can grind material away until the desired figure is attained (Fig. 1.5). As a result, grinding and polishing excels at making “large” flat and spherical surfaces [38].

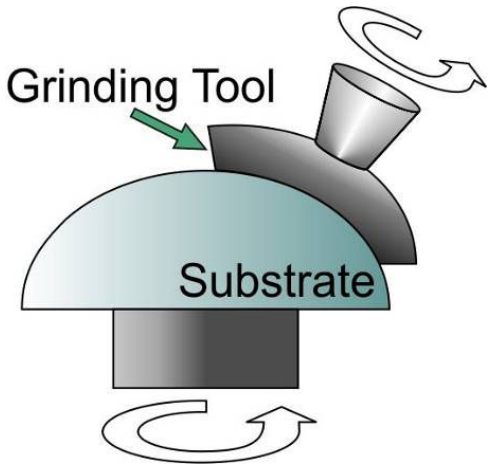

Fig. 1.5. Grinding and polishing arrangement intended to generate macro-scale traditional optics. Tools used to create the desired figure are on the scale of the optic fabricated.

As optical components have transitioned from the traditional to more intricate and complicated designs such as micro-optics, new techniques have been required to generate them. In this section, we discuss some current capabilities to generate conventional micro-optics and challenges related to these techniques when attempting more complicated designs. Despite the wide range of micro-optical components and techniques used to fabricate them, we can generally classify the most common fabrication methods into several broad categories, including photolithography, direct material removal, self-assembly, and replication. The fabrication approach is most often determined by the device application, as different techniques can have advantages and disadvantages related to resolution limits, realizable structures, cost, and speed [7, 13, 39]. Each technique is briefly introduced and discussed below. Understanding the strengths and weaknesses of these technologies helps us to choose the appropriate approaches for conventional micro-optical devices, and understand how these techniques can be leveraged to fabricate hierarchical designs.

1.5.1 Lithographic techniques

Photoresist lithography is the most common and conventional of the micro-optical fabrication techniques. It includes the use of binary lithographic masks in contact and projection systems [7], photoresist reflow [40], graytone lithography [41], phase mask lithography [42], interference lithography [43], e-beam lithography [44], laser direct writing [13], and two-photon photo polymerization [39]. Typically a light or electron beam sensitive material called photoresist is coated over the material to be patterned, or "substrate". The most common method for resist coating involves pouring the resist in liquid form onto the substrate, followed by spinning the substrate at high speeds (1,000 RPM or greater for reasonably uniform coatings) and then heating or "soft-baking" to remove remaining solvent (Fig. 1.6). The resist is then patterned by selective exposure to radiation, whether by masking portions of a collimated beam (contact lithography, projection lithography), using interfering beams of coincident coherent light (interference lithography), or focusing down a beam to a small spot (e-beam, laser direct writing). The resist is heated again in a "post exposure bake" (PEB) and can then be chemically developed. This causes selectively exposed regions to be either retained or removed, depending on whether the resist is negative or positive, respectively. In some cases, particularly for negative resists, the desired structure is the patterned resist itself. More often however, the patterned resist is used as an etch mask to transfer the pattern into the underlying substrate using wet or dry chemical etching. Mask based systems cater to high throughput, interference lithography has a large depth of field, and focused beam systems can precisely write complex arbitrary patterns.

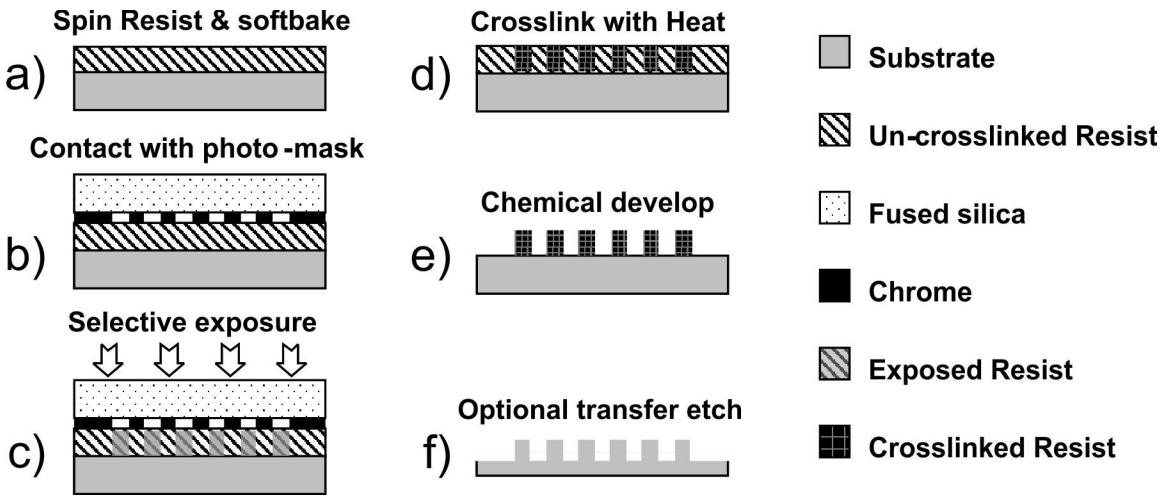

Fig. 1.6. Process diagram for contact lithography, a typical resist lithography process. (i) Resist is poured onto substrate, spun at high speed, then heated to remove excess solvent (ii) a chrome on glass photo-mask is brought into contact with resist (iii) light passes through unmasked sections, selectively exposing resist (iv) heat is applied to crosslink exposed resist (v) substrate is submersed in chemical developer that removes unexposed resist (in this case, the resist is negative) (vi) an optional etch step transfers resist features into the underlying substrate.

Fabrication requiring micro/nanostructuring of the curved surfaces common to hierarchical designs is a major challenge for traditional fabrication methods. For resist lithography, contact and projection lithography have limited depth of field (Fig. 1.7), introducing non-uniformity into any exposure on curved substrates [45].

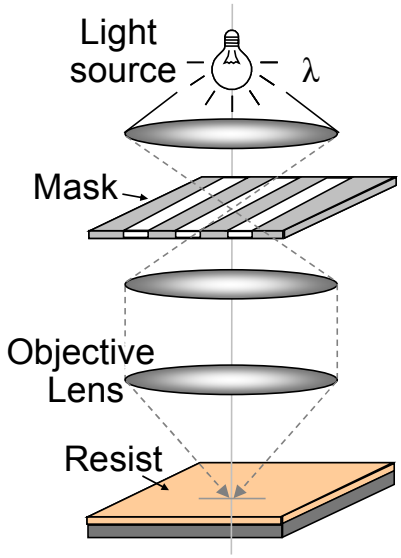

Fig. 1.7 Typical projection lithography setup. Designed and intended for flat substrates, this arrangement has little depth of field and has limited angular control, reducing its ability to generate hierarchical structures.

Techniques such as e-beam lithography can be used for exposure on contoured surfaces, but require significant hardware modifications to appropriately manipulate the substrate's position, and remain a slow and serial process [4]. Interference lithography has a sufficient depth of field, but is limited to periodic structures with a single grating orientation (the grating will stand normal to the exposure plane, rather than follow the surface curvature) [46]. In addition to the limitations involved in exposure of the resist discussed above, obtaining a uniform coating of the resist itself over contoured surfaces remains a significant challenge for conventional spin coating techniques (Fig. 1.8). During the spin coating process, the liquid resist will pool in recessed features and thin over raised ones [47]. This results in poor etch uniformity with etch depths that vary with the surface topography.

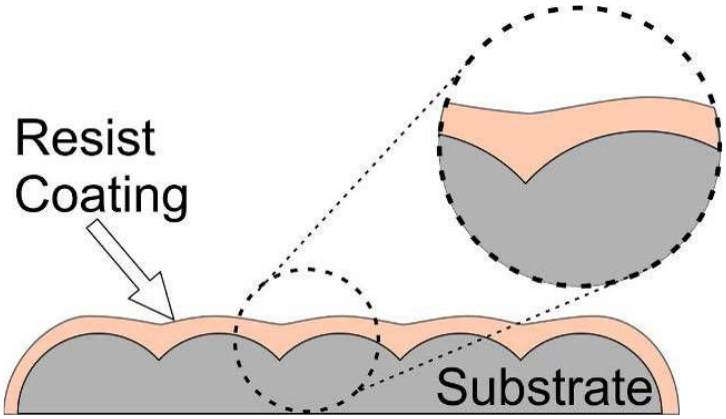

Fig. 1.8 Resist spin coating over contoured surfaces results in non-uniform resist thickness due to "pooling" in recessed features and thinning over prominent ones.

1.5.2 Direct material removal

Direct material removal methods pattern substrates by removing portions with machining techniques such as turning, fly-cutting and milling with diamond tools [48] (Fig. 1.9), or ion beam milling that uses a sputtering process [49]. These techniques are the most similar to traditional optic fabrication methods, and in fact are currently used to

generate components on both the macro and micro scales [38]. Direct material removal has the advantage that secondary steps such as development or etching are not needed. Due to their ability to cleanly cut many metals, precision diamond machining techniques are commonly used to fabricate master structures for replication processes, and can generate arbitrarily shaped metallic mirrors. Focused ion beam milling can be used on a wide variety of substrates with realizable structures similar to that fabricated by e-beam lithography [49].

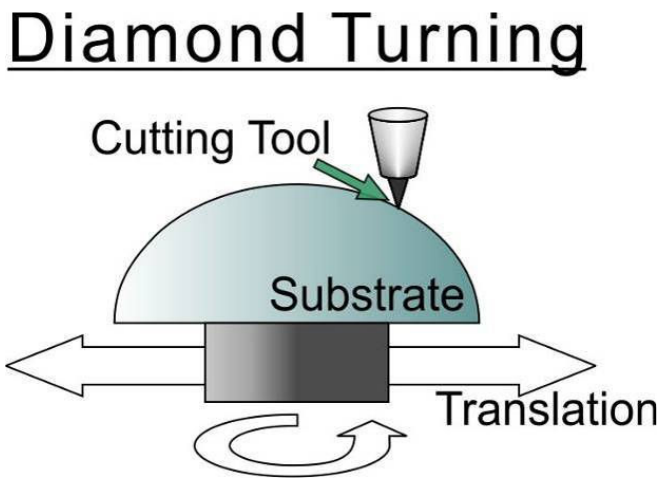

Fig. 1.9. Single point diamond turning arrangement is shown as an example of direct material removal. Substrate is rotated, while the tool is rotationally fixed but translated with slow or fast tool servo processes to generate desired surface figure. Milling processes incorporate tool rotation.

Direct material removal methods circumvent the resist coating uniformity issue. However, in diamond machining processes, when generating the macro-scale portions of hierarchical components, larger sized tools are used to efficiently remove material. These same tools are too large for generation of micro-scale portions of the device. Tool changes can be performed to scale down the size of realizable features, but obtaining accurate information regarding placement of the “new” swapped tool in relation to the machined surface remains a challenge [50]. In addition, the sizes of the smallest tools available are typically too large for subwavelength applications in the visible. Ion beam

milling can generate subwavelength structures, but suffers from slow removal rates for macro-scale components [49]. An issue common to single point diamond machining and focused ion beam milling is that, much like e-beam lithography, the initial cost of equipment is substantial, and the fact that they both remain relatively slow serial processes.

1.5.3 Self-assembly

Self-assembly techniques use the interactions between components to spontaneously generate ordered structures [51]. This process is likely the least conventional of the micro-optical fabrication methods described here. Self-assembly occurs over a number of sizes and scales. However, in this discussion we concern ourselves with micro/nano scale parts that form structures such as colloidal crystals. The interactions between components that generate these structures include Van der Waals forces, capillary action, and hydrogen bonding [52]. Colloidal crystals have desirable properties for optical applications as many exhibit a photonic band gap and are reported to have inherently hydrophobic surfaces [53]. Colloidal crystals consist of films of self organized micro-spheres into single or multiple layers (Fig. 1.10). These crystals are formed using several different self assembly approaches, including cell confinement [54], sedimentation, and vertical deposition [51]. These methods place the substrate into a suspension solution typically consisting of water or ethanol and the particle of choice. The particles are mobile within the solvent allowing them to deposit themselves in an orderly fashion on the substrate as it is removed from the solvent or the solvent is removed from the solution. The advantage to these processes is the limited amount of equipment needed to generate highly ordered structures.

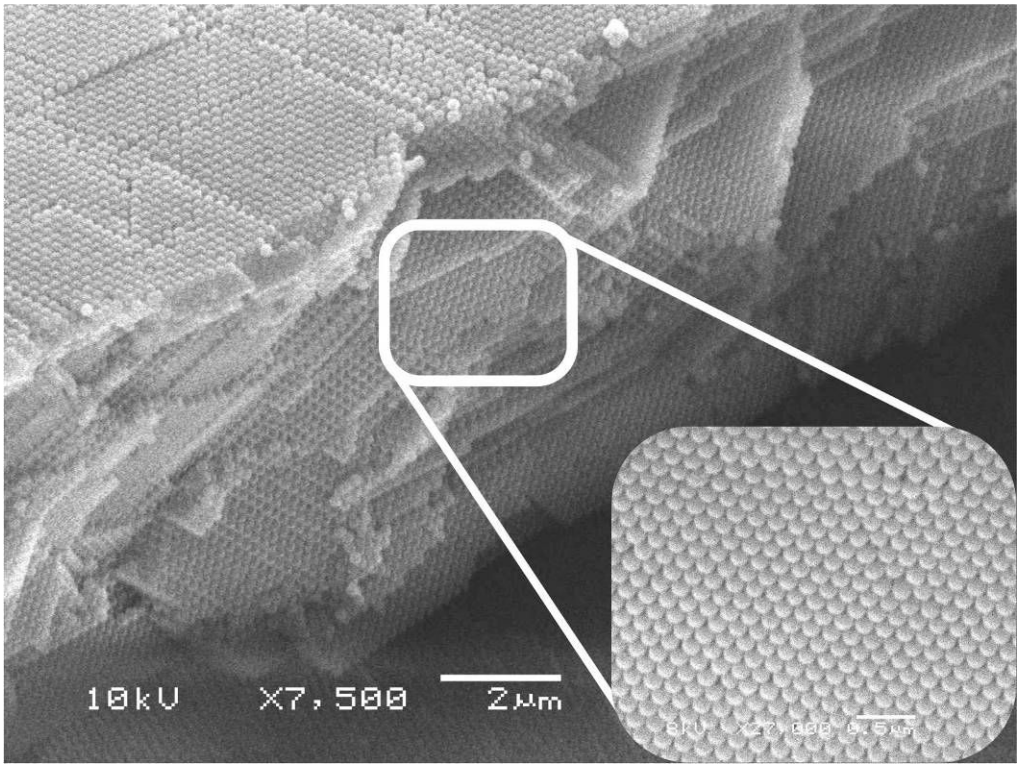

Fig. 1.10. SEM of colloidal crystal formed by the vertical deposition method, showing a large number of highly ordered layers. Close up (inset) of polystyrene sphere organization (sphere diameter = 200 nm)

Self-assembly techniques may prove useful for hierarchical optics as many of the coating processes used to create structures such as colloidal crystals should theoretically be transferable to contoured surfaces [55]. The simplest of these processes requiring the least equipment while generating uniform coatings is the vertical deposition process (Fig. 1.11). Generally this technique submerges a substrate vertically into a solution of microspheres, and allows the solvent to evaporate. A self-assembled layer of colloidal crystals form at the meniscus/substrate boundary, and are deposited over the entirety of the substrate as the solution level decreases [51]. However, many process parameters play a role in the deposition of uniform structures, including ambient humidity, temperature, microsphere concentration, substrate surface energy, and presence of other polymers added to the solution [56, 57]. In addition, current literature offers many conflicting

reports on optimized parameters [56-58]. This, combined with the length of time for each process run, which may take up to several days, can make establishing a robust process a challenge. Further complicating the issue, the substrate angle also plays a role in the rate and uniformity of deposition, adding to the challenges for spherically curved substrates [59]. Lastly, self-assembled elements are also primarily limited to periodic structures, reducing their flexibility for generating optical designs.

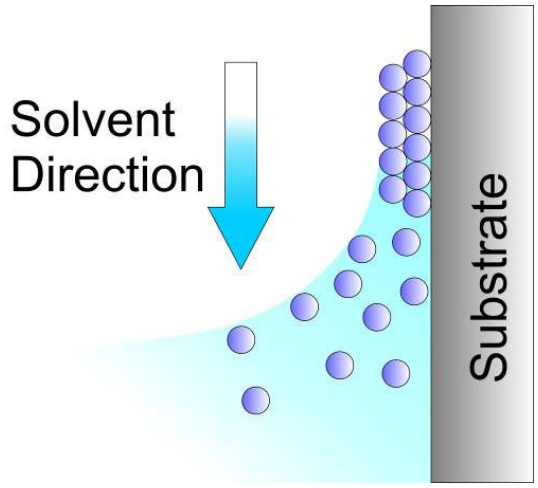

Fig. 1.11. Vertical deposition self assembly process is commonly used to generate colloidal crystals. A substrate is placed vertically in a suspension of micro-spheres, and either the solvent is evaporated or the substrate is slowly removed from the solution. The micro-spheres congregate on the surface of the substrate and deposit themselves in a highly ordered fashion, generating a crystalline structure.

1.5.4 Replication

Replication processes simply copy a structure fabricated by some other means (Fig. 1.12). This can be accomplished by a variety of techniques, including nano-imprint lithography, injection molding, micro-transfer molding, micro-molding in capillaries (MIMIC), solvent assisted molding, micro-contact printing, and hot-embossing [5, 7, 60]. Typically replication processes result in a polymer copy of the master structures. The motivation to use most replication processes is the throughput they provide. One master pattern can be quickly copied many times offsetting the cost of the slow serial process

used to generate a high quality master structure. Feature sizes attainable with these processes can be very small, with some reported to have replicated features down to the molecular level [61]. Replication can be segregated into categories based on the types of mold templates used. The first uses mold templates made of rigid materials such as metal or glass. These rigid mold templates have excellent replica feature fidelity due to low elastic deformation and low coefficient of thermal expansion (in the case of thermally dynamic processes) [62]. The second category is *soft lithographic* processes that use flexible/deformable mold templates most commonly made of elastomeric polymers. When molding on flat substrates, these mold templates can be used to improve mold template/substrate contact when sources such as particle contamination and substrate flatness may otherwise prevent uniform contact. Taking further advantage of their conformal nature, these flexible mold templates can be used to replicate features copied from a flat substrate over contoured surfaces.

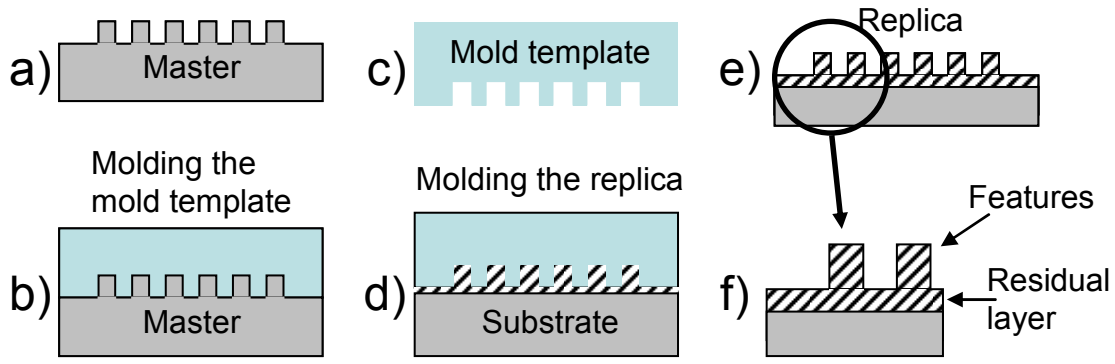

Fig. 1.12. Process flow for generalized molding process: (a) A master pattern is acquired (b) the mold template is then molded off master features, and (c) separated (d) the mold template replicates the features into another material (typically polymer) (e) and finally mold template and replica are separated. (f) A small residual layer of the molded material is typical for replication processes.

The strengths of replication processes make them attractive for generating hierarchical structures, however they still have challenges and limitations. Conventional replication circumvents many of the issues for other microfabrication methods by only

"replicating" i.e. copying other structures already formed. However these processes are typically limited to polymer replicas, which often lack the material properties desired for a "finished" micro-optic. In the case of transferring replicated features into the underlying substrate via etching, molding processes leave a "residual layer" of molded polymer requiring a descum process prior to transfer etching. The descum process requires anisotropic dry etching to properly remove the residual layer, which is intended and needed for flat substrates [63]. However, for hierarchical structures with moderate amounts of substrate curvature this may introduce poor uniformity in subsequently etched features. Another issue for hierarchical processes using soft lithography involves the elastomeric nature of the mold template. Although the inherent flexibility is a prerequisite for the process to work, it can also introduce feature distortion as the mold conforms to the curves of the substrate [64]. Yet another challenge lies in the application of the polymer to the curved substrate. Micro-transfer molding processes often used for this purpose typically require the moldable material be applied to the mold template and then transferred to the substrate [5]. However, many elastomeric polymers used in soft lithography have an inherent 'non-stick' quality. This is needed to facilitate separation of the mold template and polymer. Nevertheless, this trait puts these materials at odds with typical uniform coating methods such as spin-coating, introducing a need for additional processing steps. We chose to implement several replication processes, and as such they will be discussed in much greater detail throughout this dissertation.

1.6 Optical testing and challenges for hierarchical optics

After a device is designed and fabricated, we need a way to verify it will function as intended. A wide range of testing apparatuses exist, but the test applied is typically

dependent on what the device is intended to do. After fabrication, traditional metrology typically concentrates on the surface figure (large spatial frequency error) and finish (micro-roughness) of the optic, due to their having the largest impact on performance (material properties of transmissive components are typically tested/known prior to fabrication) [38]. Most often, measurement techniques use interference to compare a reference surface to the surface under test [65]. Because most traditional optics are spheres and flats, a small number of reference surfaces combined with an adjustable measurement apparatus can test a large number of optical components. This technique capitalizes on the symmetrical nature of these components, simplifying the testing process, increasing throughput and decreasing cost. Much like the need for alternative fabrication methods, alternative metrology methods are needed for micro-optics [66]. Because surface figure and finish are no longer the primary factors for determining optical performance, many of the methods used in traditional optics are less useful. For refractive and other micro-optical designs where surface profile remains critical, interferometric methods such as scanning white light interferometry (SWLI), confocal laser scanning microscopy (CLSM) and micro-interferometry are often used [66]. Other techniques to measure surface profile include atomic force microscopy (AFM), scanning electron microscopy (SEM), and contact profilometry. These techniques give us useful information regarding surface topography, but for many of the advanced functions common in micro-optics they give insufficient data to confirm our device will function as intended. Therefore, to further quantify device performance, measurements of transmission, reflection, polarization and beam profile as a function of the device under test are commonly used.

Hierarchical devices pose additional challenges for measurement and characterization. As discussed above, many measurement techniques are intended for use with the macro-scale elements of traditional optics or micro-optics, but not both simultaneously [67]. Because hierarchical optics consist of a combination of optical structures at different size scales, surface measurement techniques for each respective scale can provide useful information. However, getting a combined measurement of all the aspects can be quite challenging. Characterizing optical performance also becomes more challenging, as it is difficult to isolate the testing of specific optical functions without building a specialized testing apparatus. Specific approaches used for both metrology and optical performance measurements are discussed in more detail throughout this dissertation.

1.7 Dissertation outline

Chapter 1 introduces micro-optics, and discusses motivation inspired by biological systems to generate hierarchical designs. An overview of techniques used for design, fabrication and testing of conventional micro-optics is given and challenges for applying these techniques to hierarchical optics are discussed. In Chapter 2, we elaborate on techniques used in this dissertation to address the challenges associated with fabricating hierarchical optical designs. We discuss several optical designs that can be integrated to form hierarchical structures and associated advantages. Next, in Chapter 3 we demonstrate spectral guided mode resonance (GMR) filters on conformal surfaces using flexible molds as replication templates in a micro-transfer molding process. GMR filters at near-IR wavelengths fabricated on concave lens surfaces are discussed, and experimental results are presented. In Chapter 4 we demonstrate a free space compound

fly eye structure fabricated using techniques introduced in Chapter 3. In Chapter 5 we investigate a spray coating technique for deposition of resist over curved surfaces. We incorporate this technique with the large depth of field inherent in interference lithography to generate structures such as polarizers on convex lenses. Lastly, Chapter 6 summarizes the work presented in this dissertation and discusses key developments, conclusions, and directions for future work.

CHAPTER 2: REALIZING HIERARCHICAL OPTICS

2.1 Overview

Despite the discussed challenges associated with hierarchical designs, there has been a great deal of research interest in making and testing these devices. So far, there does not appear to be one technology or approach that addresses all or even most of the concerns mentioned in the previous chapter. However, by understanding the compromises involved in various techniques, and what approximations and modifications are possible, it may be feasible to satisfy specific device requirements. A large hurdle for these devices is simply that they are un-conventional. Conventional micro-optics have capitalized on a large amount of infrastructure built for the semiconductor industry. For wafer-based micro-optics, much of this infrastructure is directly applicable. For many hierarchical designs however, that infrastructure does not exist. As a result, relatively few hierarchical optical devices have been fabricated, and even fewer have been characterized. By fabricating and testing functional devices, the advantages of hierarchical designs can be demonstrated. If these advantages are significant, a greater level of infrastructure will likely follow. In this chapter, we delve deeper into the paths we have selected to fabricate hierarchical optical devices: conformal soft lithography which leverages the flexible nature of elastomeric mold templates, and interference lithography which leverages a large depth of field with spray coated rather than spun photoresist. We also introduce background on the

individual types of micro/nano-optical components that will be used in later chapters to mimic the biological optical functions previously discussed.

2.2 Fabrication approaches

2.2.1 Conformal soft lithography

Conformal soft lithography is one of the simplest, fastest and cheapest methods to fabricate features on a contoured surface. This technique has been demonstrated for transfer of patterns such as micro-lenses, gratings and many arbitrary patterns [68] into polymers such as polystyrene [45], polymethylmethacrylate (PMMA) [69] and SU-8 [70] and can be applied to virtually any substrate. Polydimethylsiloxane (PDMS) and perfluoropolyether (PFPE) are commonly used polymers for conformal mold templates [71]. Despite significant research completed on the techniques and polymers involved in conformal soft lithography, most of the literature on this topic demonstrates only the ability to transfer features onto contoured surfaces, and does little to turn these features into functional devices [45, 68, 72].

As discussed in Chapter 1, the dominant conventional resist lithography methods generally involve the formation of patterns in resist, which may be damaged relatively easily and can have poor optical qualities. In many cases, formed patterns need to be transferred into the desired optical substrate by a suitable etching process. There are several limitations to etching of non-standard substrates, and the ability to achieve the required etch selectivity and optical smoothness can be extremely challenging [7]. In applications where the optical material contains the unique functionalities, transfer etching is not an option [73]. With this in mind, molding of micro-optics offers

advantages. Various materials can be molded, and in cases where the molded material remains part of the final device, potentially complicated etching can be avoided.

To this end, SU-8, a common epoxy based negative acting photoresist, is a promising polymer for micro-optical replication for multiple reasons. It can remain part of a functional device as an integrated unit [74]. It is mechanically robust, enabling high aspect ratio structures and MEMS applications. The high chemical resistance to most solvents makes it widely used in microfluidics. SU-8 has relatively high refractive index after curing, making it a promising candidate for plastic/polymer optics [14]. SU-8's thermal resistance, with operating temperatures above 200°C, and high transmittance allow it to be implemented in applications with higher optical power densities than typical optical polymers used for replication [75, 76], and it can be applied to a wide variety of substrates. SU-8 is useful over a broad range of wavelengths with high transmittance ranging from visible to near-infrared [14].

Work done previously in the molding of SU-8 demonstrates its applicability for micro-optics. Several examples of molding of diffractive structures in SU-8 exist in the literature [74, 77, 78]. An example of a molded microlens array in SU-8 has also been demonstrated, but requires a UV exposure prior to separation [14]. A compound microlens array in SU-8 mimicking the ommatidia arrangement of a fly eye is one of the few hierarchical designs fabricated and tested [79]. Despite fabrication limitations requiring precise dispensing and size restrictions, this device also has the inherent limitations of a real fly eye. Work has also been performed combining molded diffractive structures in SU-8 and photolithographic processes to generate 2D and 3D periodic structures [77].

In this dissertation we use two SU-8 molding processes. The first of these is intended to photolithographically incorporate 2D and 3D structures onto and into molded wafer scale refractive micro-optical designs, and serves as a baseline SU-8 molding process for comparison with less conventional methods. This method combines a rigid mold template and polymer under vacuum at room temperature, and then applies low pressure and heat. Molding occurs after the glass transition temperature of SU-8 is reached. The mold templates are separated from the resist after cooling and prior to UV exposure. The second method is intended to replicate features from patterned flat substrates onto macro-scale contoured surfaces. This technique applies SU-8 to PDMS mold templates which are then micro-transfer molded to contoured surfaces at an elevated temperature, and then cooled prior to separation. Utilizing the low temperature (below 120°C) molding processes discussed in this dissertation, micro-optics in SU-8 can be molded directly onto wafer based semiconductor elements such as laser diodes or LEDs. In addition, these processes leave SU-8 photosensitive after molding, giving us the option to perform additional structuring of molded features through photolithography. This can be used to create additional hybrid structures (discussed in Appendix A) that may be difficult or impossible to make using other fabrication methods.

2.2.2 Baseline SU-8 molding process

While photolithographic patterning of SU-8 is relatively common, molding of SU-8 requires different processing parameters due to challenges with solvent removal and cross linking. Our SU-8 molding methods leverage conventional SU-8 processing techniques to address these challenges, as shown in Fig. 2.1 and discussed in detail below.

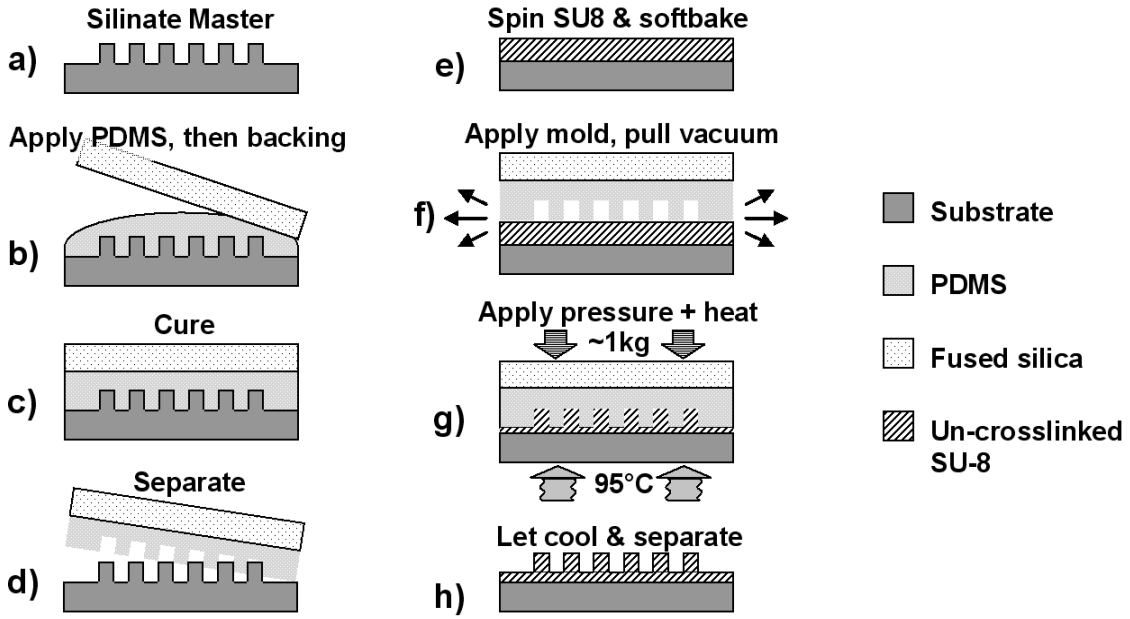

Fig. 2.1. Process chart for hard-backed mold generation and vacuum molding process. (a) Silination of master wafer prepares surface for separation from PDMS. (b) PDMS is applied to master and rigid backing is added. (c) PDMS is thermally cured and (d) separated from master. (e) SU-8 is spun and softbaked conventionally. (f) PDMS mold template and SU-8 wafer are brought into contact and vacuum is applied. (g) Heat and pressure transfer the pattern into SU-8. (h) Wafers are cooled and separated.

Solvent content and distribution provide significant challenges in molding and lithographic processes for SU-8. Work involving photolithography on thick layers of SU-8 serves as an example to show the difficulty with controlling SU-8 solvent content when standard resist processing (spin and soft-bake) is not used. These techniques require a variety of solvent removal techniques, such as multiple casting and dry chip casting, to create a uniform solvent distribution throughout the resist layer [80]. With some of these processes requiring more than 30 hours, and issues related to repeatable layer thickness, similar approaches are poor candidates for molding. It has been shown that surface layers tend to lose solvent at a much higher rate, resulting in “crust” formation and internal solvent trapping [80]. Some molding techniques can create a similar issue, as non-porous molds placed over fluid SU-8 (solvent rich) will prevent adequate means of dissipation.

The remaining solvent can lead to bubble formation as heated solvent evaporates but remains trapped. Standard processing for spinning and soft-baking single coated SU-8, similar to that used in our processes, attains proper solvent reduction and distribution prior to contact with the mold. However, following the soft-bake, when solvent is removed, SU-8 solidifies at ambient temperatures. The molding techniques at temperatures above the glass transition temperature (T_g) of 50 °C [81] used in our processes helps to prevent voids formed from air trapping and solvent evaporation.

Due to SU-8's high level of adhesion to a variety of substrates, an intermediary mold was needed to enable mold release and preserve master feature integrity. The silicone elastomer PDMS was chosen because of its highly conformal properties, relatively low shrinkage [82] and easy separation (due to low intrinsic surface energy) from SU-8. There are several formulations of PDMS, but for characterization described here, we use conventional Sylgard 184 PDMS. For simplicity, this standard 184-PDMS will simply be referred to as PDMS. The general properties and techniques of soft lithography [5] were leveraged heavily for these processes. Master wafers were prepared for separation from PDMS by silination in a vacuum oven for 1 hour at 100 °C with Aquaphobe (Gelest Inc. Morrisville, PA). For masters in resist, temperatures were reduced to 80 °C to prevent reflow or excessive solvent loss. PDMS was prepared by mixing 10:1 pre-polymer to curing agent in accordance to standard processes.

To prevent void formation, we used a vacuum process developed with hard-backed molds for thermally and pressure assisted molding [70] (Fig. 2.1). Uncured PDMS was applied to master wafers, then a 100 mm diameter fused silica wafer was applied to serve as the rigid backing. PDMS wicked to the edges of the wafers via capillary forces. The

mold was cured on a level surface in an oven at 60 °C for 4 hrs, allowed to cool, and then separated. The rigid backing provides additional thermal and structural stability to the PDMS mold [83]. Various formulations of SU-8, typically Series 2002, 2007, and 2025, were spun onto substrates at 2500 RPM for 60 sec following conventional processes. Spin speed and resist formulation were adjusted to allow for features of different heights and surface area fill factors. For 30 μm thick SU-8, a 6 min soft-bake at 95 °C was done on a hot plate; these parameters can be adjusted if different thicknesses or substrates are used. Following the soft-bake, the wafer was allowed to cool. Special care must be taken to avoid void formation when the mold template and coated wafer are brought together. When combined, a thin layer of air will prevent contact between the two surfaces. However, once any part of the PDMS mold template does make contact with the substrate, surface adhesion forces will drive out the remaining air. Independent of the ambient pressure, the wafers will typically appear free of voids. However, if wafers are combined at atmospheric pressure, small pockets of trapped air will exist. Once heated, these voids will expand and disrupt full wafer fidelity (Fig. 2.2 (a)). To prevent this issue, the mold template and substrate were combined in a vacuum chamber, and the chamber was evacuated prior to contact between the surfaces. Once vacuum is established, the film of air is removed and the parts come into contact free of voids (Fig. 2.2 (b)). The combined parts can then be removed from the chamber without loss of the "seal" between the surfaces. This effect is dependent on feature geometry, as large tall structures may prevent voids from forming without the need for these additional steps. The mold and resist were then placed in contact in a vacuum oven at 95 °C. A small weight, (~1 kg), was placed onto the combined wafers, and the chamber was then evacuated. The wafers

remained in contact for approximately 45 min. The wafers were removed from the oven, allowed to cool, and then separated, leaving molded patterns on the coated wafer. This process reduced void formation with consistent full wafer fidelity (Fig. 2.3). Residual layer thickness was comparable to the molded feature sizes with layers as low as 75 nm for 330 nm deep features (Fig. 2.4).

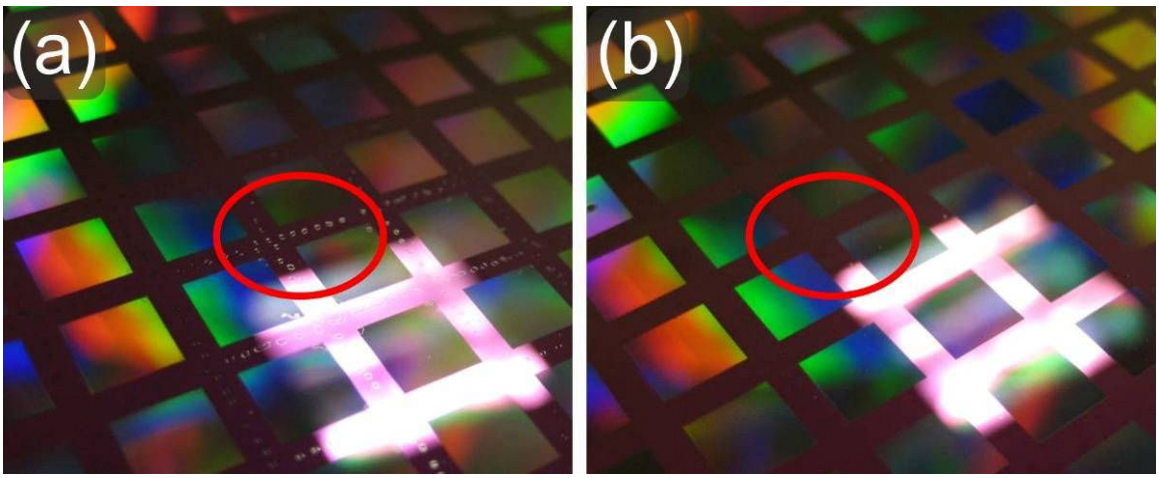

Fig. 2.2. Replicated SU-8 wafer combined with mold template at (a) atmospheric pressure showing voids present after molding, and (b) under high vacuum with voids eliminated

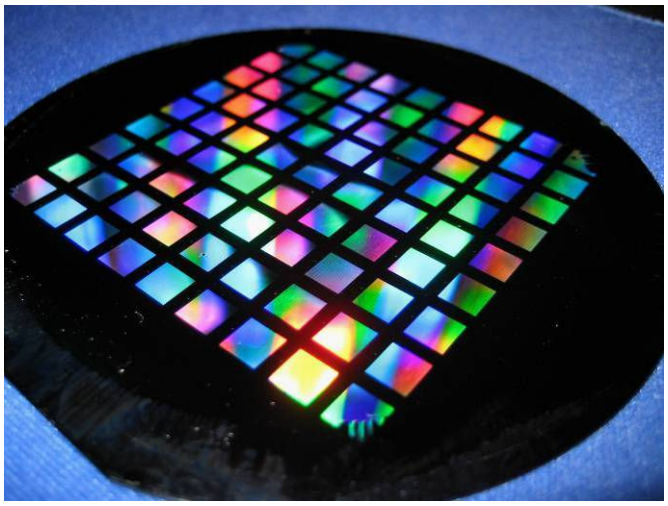

Fig. 2.3. Molded SU-8 patterns on 100 mm silicon wafer show wafer level capability

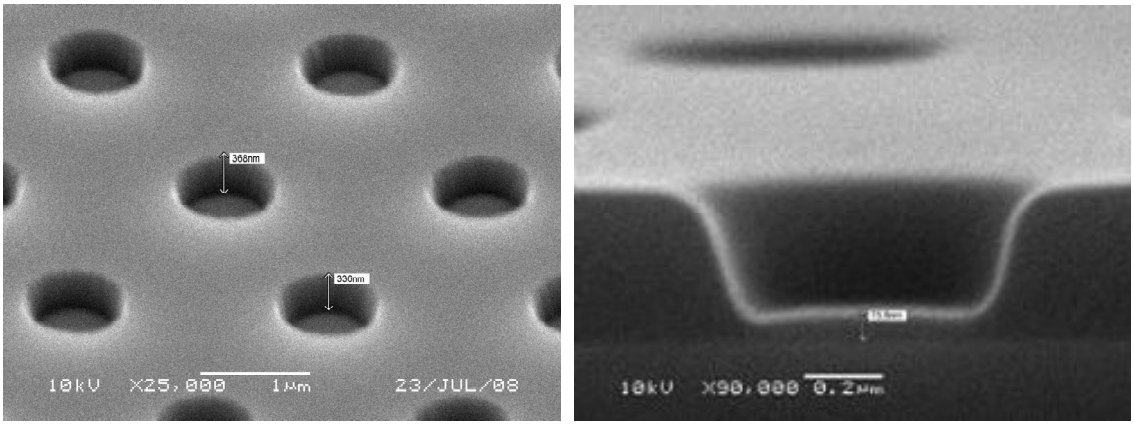

Fig. 2.4. SEM images of molded SU-8 2D gratings with 330 nm deep features and 75 nm residual layer.

In general, PDMS is an excellent intermediary, however care must be taken to ensure the mold template can be used for multiple molding cycles. A cleaning process removed any SU-8 that had adhered to the PDMS template during the molding process. The template was submersed in SU-8's developer propylene glycol monomethyl ether acetate (PGMEA) for 2 minutes, submersed in isopropanol alcohol (IPA) for 2 minutes, rinsed with IPA, and then blown dry with nitrogen. To remove any solvent absorbed by the PDMS following the cleaning process, the template was baked for 5 min at 95 °C, and then allowed to cool.

Our hard backed replication process enables wafer scale replication with low void and bubble formation, thin and uniform residual layers, and low feature distortion, enabling it for generating baseline structures discussed in Chapter 3. Additional investigation into the use of SU-8 as a molded photoresist, process parameters, applications, and limitations are presented in Appendix A.

2.2.3 Interference lithography

A lithographic approach that utilizes the resulting intensity distribution generated by interfering coherent beams to expose resist is called holographic or interference

lithography (Fig. 2.5 (a)). This process produces periodic structures over large areas with large depth of field, making it a candidate for exposing resist on or containing topography while using little sophisticated equipment (Fig. 2.5 (b)) [46].

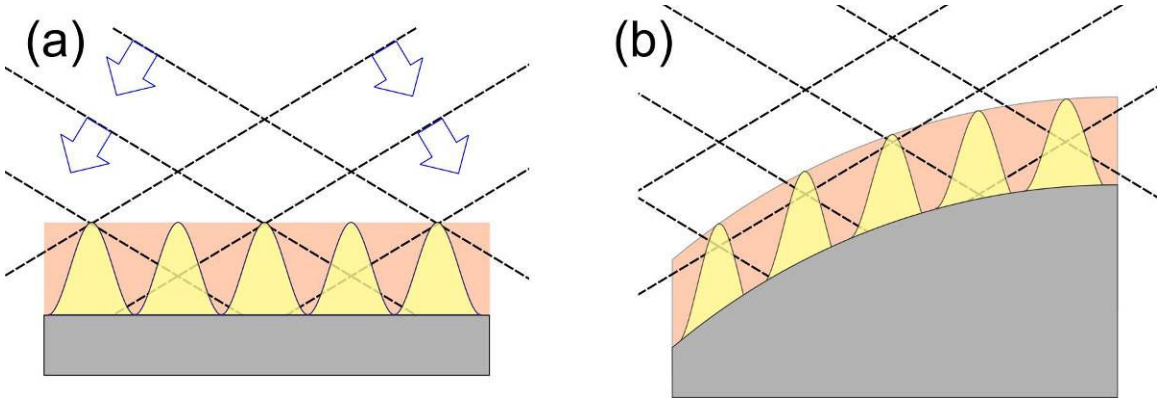

Fig. 2.5. Interference lithography works by interfering beams of coherent light. (a) Two interfering beams create a modulated irradiance distribution in photoresist. The method has an inherently large depth of field, (b) enabling lithography on curved surfaces.

The period (Λ) is dependent on the wavelength (λ) of light interfered and angle of incidence (θ) as given by the following equation:

$$\Lambda = \frac{\lambda}{2sin\theta} \qquad \text{Eq. (2.1)}$$

The resulting irradiance distribution (I) for two interfering plane waves is given by the equation below, where I_0 is the irradiance of each beam [84].

$$I = 2I_0\left(1 + \cos\left(\frac{2\pi x}{\Lambda}\right)\right) \qquad \text{Eq. (2.2)}$$

With an appropriate setup, pitch can be modified to be either smaller or larger than the interfering wavelength, as shown in Fig. 2.6. Typical photoresists have a small range of exposure wavelengths however, placing limitations on the periods readily possible with interferometric exposure.

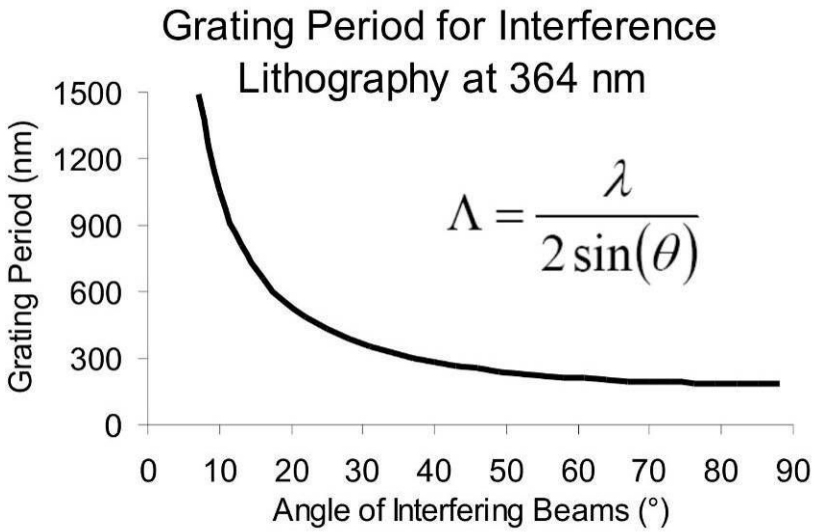

Fig. 2.6. Range of available grating periods for 364 nm interferometric lithography

Interference lithography has been demonstrated using various setups by many groups, with holographic exposures dating back to the late 1940s [7]. The setup we use is a Lloyd's mirror configuration, as shown in Fig. 2.7 with laser and mirror hardware shown in Fig. 2.8 [85]. This setup passes light from a Coherent Innova FReD 300 Argon Ion laser operating at 363.8 nm through a spatial filter, and then the beam is allowed to expand until the waves are approximately planar. A resist coated substrate and planar mirror are positioned at a 90° angle to each other and placed in the beam's path. A portion of the expanded beam reflects off the mirror onto the substrate while the other portion strikes the substrate directly. The two beams then interfere, patterning the photoresist. Fringe periodicity can easily be modified by rotating the mirror/substrate setup. This setup reduces complexity and the number of components when compared to setups used by Agayan et al, which pass through a beam splitter, spatially filter each leg, and then propagate to the substrate [86]. A fringe locking system is typically required for

these systems. In addition, changing the grating period requires the realignment of two spatial filters.

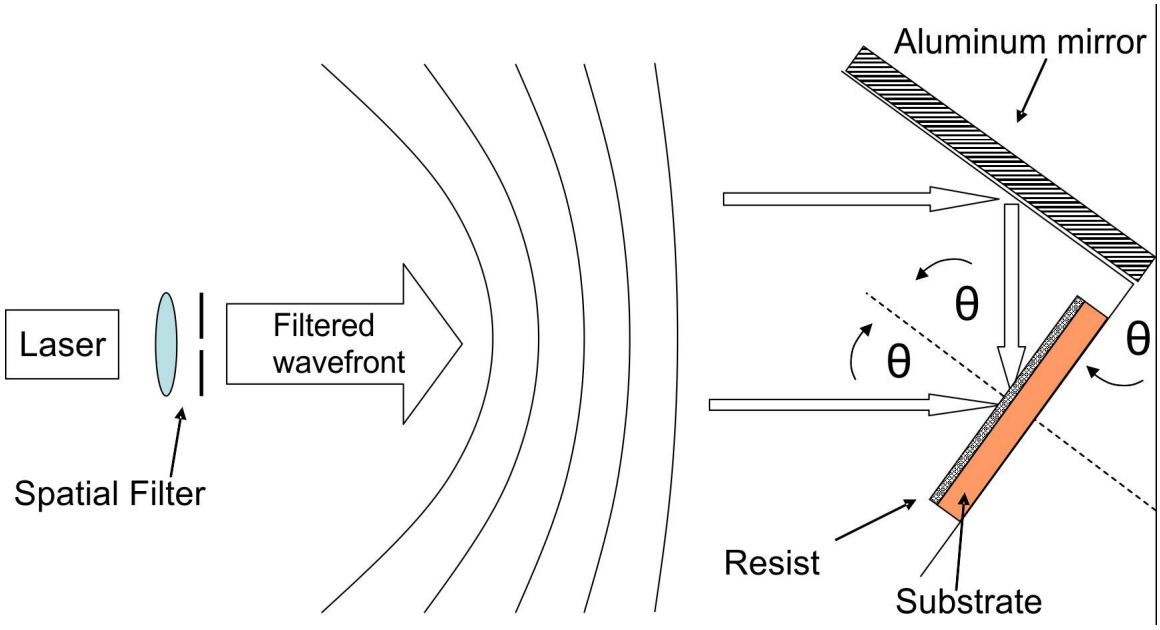

Fig. 2.7. Lloyd's mirror configuration for interference lithography. Coherent light is spatially filtered, and expanded. The approximately planar waves are incident on both the substrate and a mirror positioned at a 90° angle to each other. The beams then come together and interfere in the photoresist, with a period determined by the angle θ.

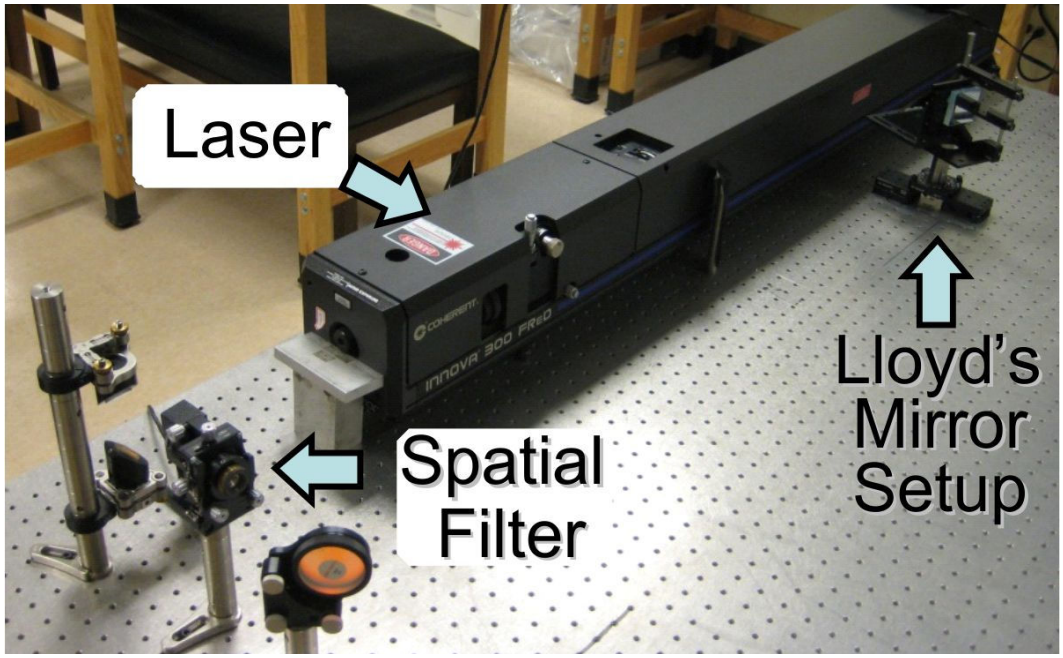

Fig. 2.8. Hardware setup for interference lithography using a Lloyd's mirror configuration.

2.3 Approaches for biomimetically inspired optical functions

2.3.1 Spectral filters through guided mode resonance

As discussed previously, one feature of the mantis shrimp eye is an integrated spectral filtering capability. With this inspiration in mind, we investigated man-made spectral filters as candidates for integration onto curved surfaces. Of particular interest was the guided mode resonance (GMR) phenomena, studied and exploited for applications in sensors, polarizers, dichroic laser mirrors, and more. GMR filters are relevant due to their ability to perform high contrast, narrowband spectral filtering with a relatively simple design, consisting of only a few patterned dielectric layers [87]. A typical GMR design consists of a diffraction grating and a waveguide [88]. Fig. 2.9(a) shows a simple form of GMR, where a periodically modulated index layer serves as both diffraction grating and waveguide.

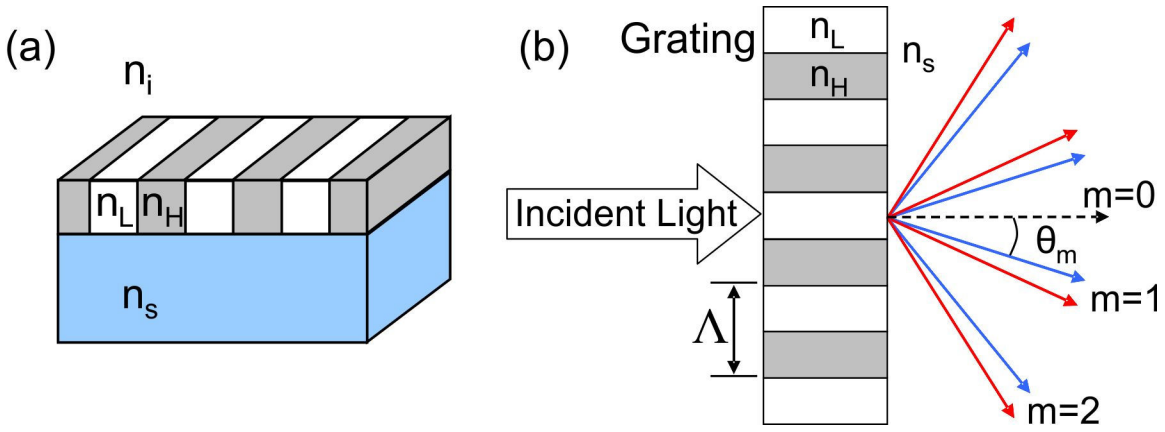

Fig. 2.9. (a) GMR structure where the grating layer serves as both the diffracting and waveguiding layer. (b) Grating structures diffract light into m orders at specific angles, dependent on wavelength, angle of incidence, and grating period.

As shown, n_H is a region of high index, n_L is low index, n_i is the superstrate index and n_s is the index of the substrate. Light diffracted by the grating will be separated into diffraction orders at angles as shown in Fig. 2.9(b) determined by the grating equation:

$$n_i \sin\theta_i + n_s \sin\theta_m = \frac{m\lambda}{\Lambda} \qquad \text{Eq. (2.3)}$$

where θ_i is the angle of incidence, θ_m is the angle of the m^{th} diffracted order, m is an integer value for the m^{th} order, λ is the wavelength, and Λ is the grating period.

For propagating modes to exist within the waveguide, it must have an effective index n_g, larger than surrounding substrate and superstrate [33] approximated by the following equation:

$$n_g \cong \sqrt{\frac{n_H^2 + n_L^2}{2}} \qquad \text{Eq. (2.4)}$$

When the angle of a diffracted order coincides with a possible propagating mode, energy will be coupled from diffracted light incident on the grating into a leaky mode in the waveguiding layer. Light propagating in the waveguide interacts with the grating, coupling light out of the mode. The light coupled out of this leaky mode destructively interferes with transmitted light, and constructively interferes with light in the direction of specular reflection [89]. The resulting reflection for a narrow band of wavelengths occurs over a small range of angles to form a high contrast spectral filter. Because grating and waveguide parameters can be adjusted, GMR devices can easily be tuned over a broad range of wavelengths. These characteristics have enabled these devices as wavelength division multiplexors [87], humidity sensors [90], and rapid medical testing components [8] to name a few examples.

GMR devices are sensitive to changes in feature parameters and materials, and thus benefit from well controlled and characterized fabrication processes [34], such as semiconductor fabrication techniques, which are designed and optimized for flat

substrates. Techniques such as interference lithography [90], projection lithography [91], contact lithography [92], e-beam [93], and replication [94] have all been used to demonstrate successful devices. GMR filters have been fabricated in a wide range of dielectric materials, typically with a combination of high and low refractive index materials. Choosing appropriate materials ensures that the waveguiding layer has a sufficient refractive index contrast between it and surrounding materials to enable a propagating mode. High index materials, including hafnium oxide, tantalum oxide, and silicon nitride, are commonly coupled with low index materials such as silicon dioxide [88, 90, 95]. Two fabrication approaches are commonly used to generate GMR devices (Fig. 2.10). One method deposits layers of dielectric material on an un-patterned substrate, and then coats those layers with photoresist. The photoresist is then exposed and the pattern transfer etched into the underlying dielectric layers [90]. This technique allows for control over feature duty cycle and sidewall profile. Another common approach uses deposition of dielectric layers over features already patterned on the substrate. This technique facilitates simple fabrication of devices from molded features, as no etching is required [34]. Despite the wide range of methods and materials used to construct GMRs, to date these devices have been fabricated exclusively on flat surfaces.

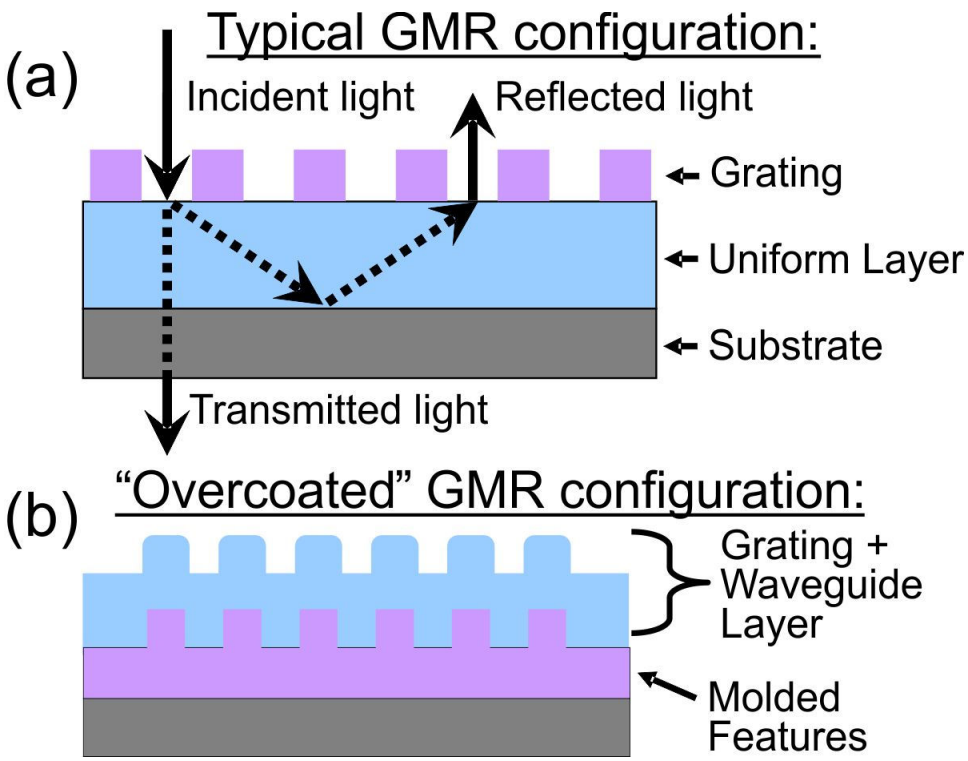

Fig. 2.10. Two common GMR configurations. (a) Dielectric layers are deposited and then patterned. (b) Features are patterned (in this case molded) followed by deposition of dielectric layers.

Due to the characteristics described above, flat GMR filters have a wide variety of uses. However, integrating these structures onto curved surfaces can enable new functions and applications. The specific application we have targeted is for use as a fiber laser cavity mirror in a retro-reflection configuration. A fiber laser in its simplest form consists of a section of doped fiber serving as the active gain medium which is optically pumped, and some form of reflector at both ends of the fiber [96]. Recent advances [97] have had a positive impact on the number and variety of applications these lasers are being used for, ranging from cutting, welding and drilling in manufacturing to laser surgical knives and optical coherence tomography (OCT) of biological tissues in medicine [98, 99]. Fiber lasers often use a spectrally selective reflective element as one of the cavity mirrors to help stabilize and spectrally narrow the output [100]. GMR filters

have been used as external optical elements to serve as reflective elements in fiber lasers, but require optics for beam expansion and collimation at the fiber terminus [100] (Fig. 2.11(a)). By using a curved GMR, the additional optics become unnecessary as the concave surface can be positioned to match the diverging beam exiting the fiber, refocusing reflected light back into the fiber as shown in Fig. 2.11(b). This reduction in optics enables a smaller footprint and lighter weight configuration. We discuss the design, fabrication, and testing of a curved GMR in this configuration in detail in Chapter 3.

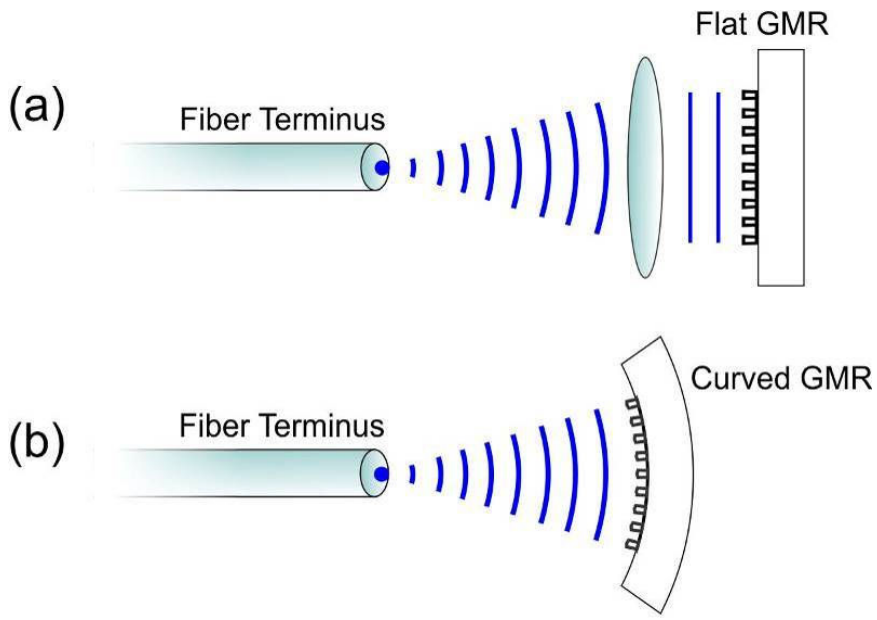

Fig. 2.11. Fiber laser with external GMR used to promote stability and narrowed linewidth. (a) A flat GMR requires optics to expand and collimate the beam. (b) A concave GMR placed to match the curvature of the wavefront can eliminate the need for additional collimation/focusing optics.

2.3.2 Enhancing FOV through compound lenses

A recurring theme of optical systems found in small animals is the compound eye. A simple device conceptually, consisting of an arrangement of small lenses over a larger lens, but capable of providing wide FOV with a relatively small optic (Fig. 2.12). For

traditional lenses, field of view can be estimated geometrically using the following equation:

$$FOV = 2\tan^{-1}\left(\frac{d}{2f}\right) \qquad \text{Eq. (2.5)}$$

where d is the diameter of the sensor, and f is the focal length of the lens.

To give some perspective regarding the FOV improvement for compound lenses, the following arbitrarily chosen compound eye specifications were compared with similar traditional lenses. For a compound arrangement with 25 lenslets (focal length = 7.8 mm) spread over a 15.9 mm ROC hemispherical window imaging on 25 individual 1 mm wide sensors placed in the imaging plane of each lenslet (for simplicity in the example, the lenses are spread in a line similar to those shown in Fig. 2.12) a 180° FOV can be achieved. Replacing this configuration with a 15.9 mm ROC traditional lens focusing on a combined sensor width of 25 mm provides a 44° FOV. By decreasing the focal length of the macro-scale lens to match the lenslets a 117° FOV can be achieved. Although this example is overly simplified, and does not account for whether practical implementation of these arrangements would function well, or image quality and aberrations of each configuration, it does provide some insight into the FOV advantages possible with compound lenses.

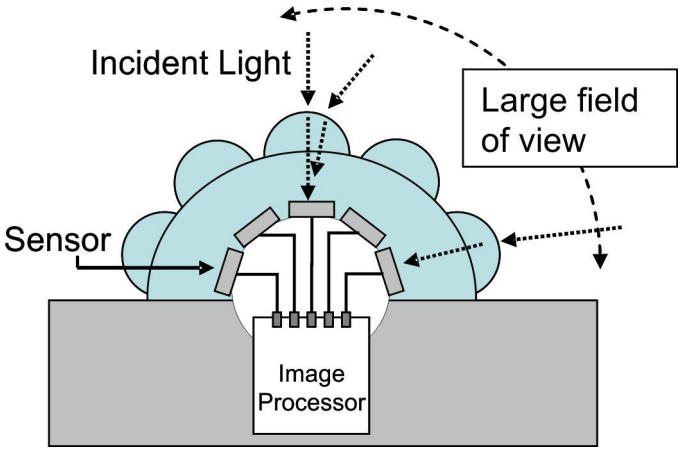

Fig. 2.12. Compound lens concept configuration. Lenslets placed over macro-scale lens increase FOV without significantly increasing the size of the optical device.

The lens is one of the oldest and simplest optical elements used by man, but in man-made systems, compound imaging systems similar to those in nature are not commonly found. This is mostly due to the lack of good fabrication processes to generate them. Despite being similar in concept to conventional lenses, traditional grinding and polishing cannot be used, calling for alternative approaches. The few devices found in the literature have primarily been fabricated using diamond machining, as this can excel at making larger scale freeform surfaces [48, 101]. However, diamond machining is a serial process that is slow and expensive. Thus, lithographic or replication processes that enable parallel fabrication of lenses are highly desirable. Because they form the basis of so many biomimetic systems, overcoming the associated fabrication limitations would give us the ability to incorporate micro and nano-optic structures to form more complex and functional optical devices. We discuss the design, fabrication, and characterization of a compound lens system in more detail in Chapter 4.

2.3.3 Polarization selectivity through wire grid polarizers

In addition to the mantis shrimp's ability to perform spectral filtering, the mantis shrimp eye also has the ability to detect the polarization of light. Man-made devices that select a particular polarization state are abundant in literature, however successfully incorporating these designs onto contoured surfaces remains a challenge.

The simplest man-made polarizing elements convert randomly polarized or "un-polarized" light to light of a specific linear polarization. Polarizers are one of the most commonly used optical elements, with many applications including use in free space optical switching, fiber optics, magneto-optic data storage, polarization based imaging systems, metrology tools, spectrometry, and more [102, 103]. A polarizer generally consists of an element with asymmetric physical properties that contribute to passing of one polarization and selectively absorbing, reflecting, or scattering another [32]. One of the simpler of these devices is the wire grid polarizer. This device is comprised of parallel conducting "wires" that lie in a plane normal to that of the propagating wavefront as shown in Fig. 2.13. For the device to perform well, the wires must be subwavelength relative to the incident light. When TE polarized light (light whose electric field oscillates in the direction of the elongated wire grid) is incident on the polarizer, the electric field will cause the electrons in the conducting wires to oscillate along the wire's length, generating a current. As a result, some of the energy from the wavefront will be reflected and some will be absorbed as it is converted to joule heat as the electrons collide with lattice atoms. For the TM polarization, the electrons are bound by the finite width of the conducting wires, preventing them from freely oscillating in the direction of the electric field. Therefore, the TM polarization passes through unimpeded. In reality no polarizer

completely absorbs or transmits either wavefront, but extinction ratios, the ratio of the passed wavefront to the absorbed, can range into the tens of thousands.

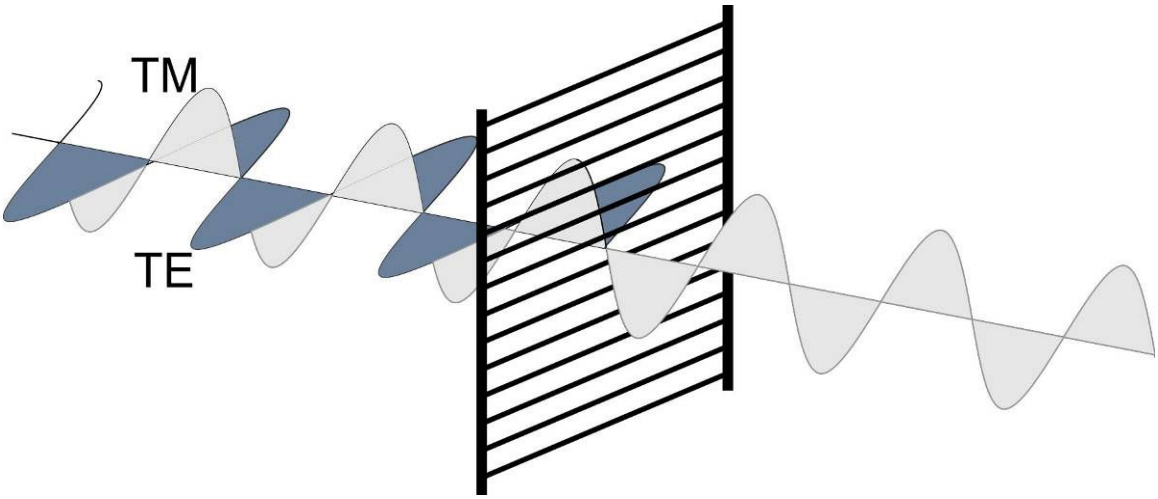

Fig. 2.13. Wire grid polarizer consisting of parallel conducting wires. Light whose electric field runs parallel to the conducting wires (TE) incident on the polarizer will be blocked. Light whose electric field runs perpendicular to the wires (TM) will pass through. The ratio of the amount passed to the amount blocked is known as the extinction ratio.

There are many ways to fabricate wire grid polarizers, most of which involve creating subwavelength metal gratings. The most common techniques can be separated into two categories: those that pattern a substrate or underlying layer first and then deposit metal, and those that deposit uniform metal that is then patterned after. The first technique has the advantage that patterns can be formed using traditional techniques without having to account for changes in lithographic patterning due to the highly reflective nature of metals, and etching of the metal can potentially be avoided. For example, etched or photoresist grating structures can be coated with a layer of metal as shown in Fig. 2.14. Depending on the sidewall profile, a break in the coated metal layer can exist. For etched gratings, the break is sufficient to allow the polarizer to transmit or block the respective polarizations with no further processing. For structures in photoresists that are not suitable for finished devices (common positive novolac based

resists for example), the breaks allow for easy dissolution of the top layer with a proper solvent, leaving only the bottom metal gratings. The second technique involves patterning grating structures on top of a uniform metal layer and then etching the patterns via wet or dry etching into the underlying substrate. This technique is attractive for its compatibility with processes that produce features with slightly positive sidewalls or for thicker metal layers [102]. By incorporating a back anti-reflective coating layer prior to photoresist application, the reflective nature of the metal can be significantly reduced.

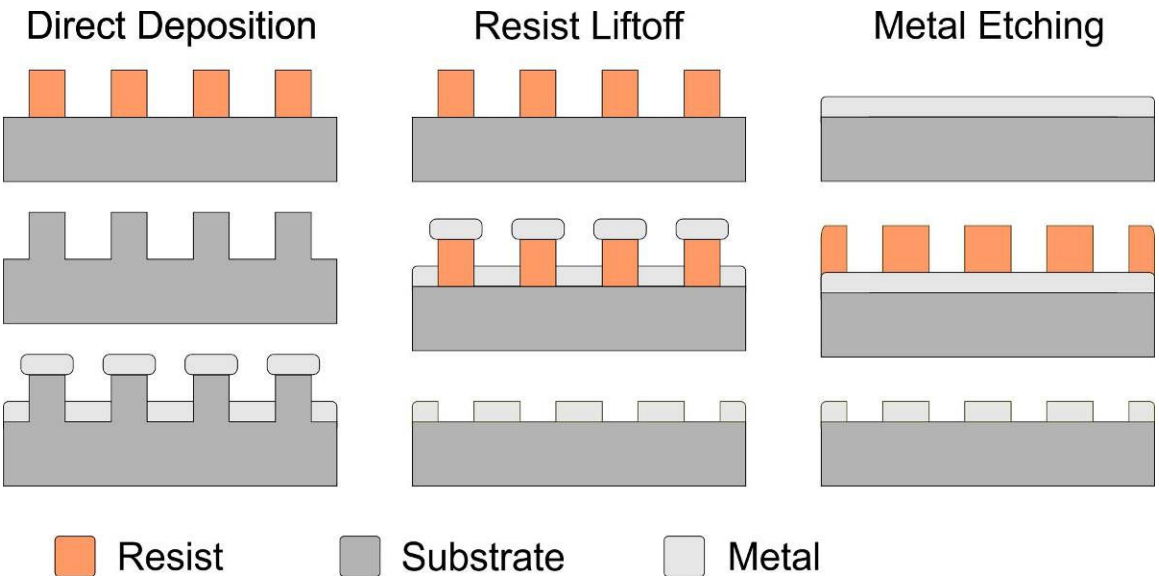

Fig. 2.14. Fabrication processes used to make wire grid polarizers. For direct deposition, patterns in photoresist are etched into an underlying substrate, and then coated with metal. For resist liftoff, photoresist patterns are coated with metal and then an appropriate solvent is used to dissolve the photoresist, leaving metal gratings. For metal etching, a metal layer is deposited first, and then patterned photoresist is used to transfer features into the underlying metal layer.

Because polarizers are such common and essential components to so many optical systems, and because they are typically a standalone component, incorporating the devices onto surfaces already in many of these systems can not only improve efficiency but also reduce the footprint of the optical system. Incorporating polarizers onto the curved surfaces of the encapsulation of light emitting diodes (LED) is one such example.

LEDs inherently produce unpolarized light, but if their output is polarized they can have additional applications in high-contrast imaging, optical communications and LCD backlighting [104]. To convert the LED output to polarized light, several techniques can be employed, such as an external polarizer, a polarizer directly on the LED die, and one built onto the lens shaped encapsulation layer. Sepsi et al shows that by incorporating the polarizer onto the encapsulation layer a significant improvement in extraction efficiency is observed compared with the external polarizer or polarizer on the die [104]. They do however acknowledge the associated fabrication challenges. To our knowledge, the only polarizers currently demonstrated on curved surfaces have had measured extinction ratios below one, far below a "functional" level [105]. We discuss the design, fabrication, and characterization of a wire grid polarizer on a convex lens surface in more detail in Chapter 5.

CHAPTER 3: CONFORMAL GUIDED MODE RESONANCE FILTERS

3.1 Overview

The theoretical advantages for biologically inspired hierarchical elements have motivated researchers to pursue techniques to design, fabricate, and test these complicated structures. Combining spectral filters with contoured surfaces provides specific advantages, mimicking the spectral filtering capability integrated into a mantis shrimp's vision system. Guided mode resonance filters were selected to be part of our hierarchical element, as they are highly functional micro-optics capable of narrowband spectral filtering. They receive a great deal of interest due to their simple design and high performance in sensing, polarization sensitive filtering, laser cavity mirror applications, and more [87, 94]. Their simple design is of particular interest, as it offers a possibility for fabrication onto contoured surfaces. GMR devices have previously been demonstrated on flat substrates using a wide range of materials and configurations. In this chapter, we apply the soft lithographic technique introduced in Chapter 2 followed by deposition of dielectric layers to generate GMR filters on a concave lens surface. The GMR is designed as a retroreflecting spectral mirror for integration into a fiber laser cavity with a target reflected wavelength at 1550 nm. A testing apparatus is built and characterized to measure the reflectance from flat and curved surfaces. Resonances of the resulting conformal GMR filters are then experimentally measured and characterized, and the

results are compared to the performance of similar GMR filters fabricated on flat surfaces.

3.2 Design

A critical aspect of the GMR design is the fabrication process used to fabricate the device. To generate GMR filters using conformal molding techniques, grating patterns are first replicated onto a substrate and then coated with dielectric layers (Fig. 3.1). The grating parameters of the master structure are fixed, however the thicknesses of the molded residual layer, and deposited dielectric layers can be adjusted to select desired resonance properties. The master 4 inch wafer contains an array of 5 mm square die patterned by g-line stepper lithography and etched into fused silica. The grating is a polarization insensitive hexagonal lattice [34] with lattice constant *a* of 1150 nm, 43% duty cycle, and 90 nm depth. BK7 glass is selected for use as our substrate material (n = 1.5075). Our molded polymer is SU-8 negative photoresist. Crosslinked SU-8 (n = 1.5669) can withstand temperatures of 300 °C, making it compatible with plasma enhanced chemical vapor deposition processes (PECVD) used for these devices. A deposited high index silicon nitride (SiN, n = 1.9240) layer serves as both the diffractive and waveguiding layer. Deposited silicon dioxide (SiO_2, n = 1.4440) serves as a buffer layer to isolate the grating and waveguiding layer from the higher index SU-8.

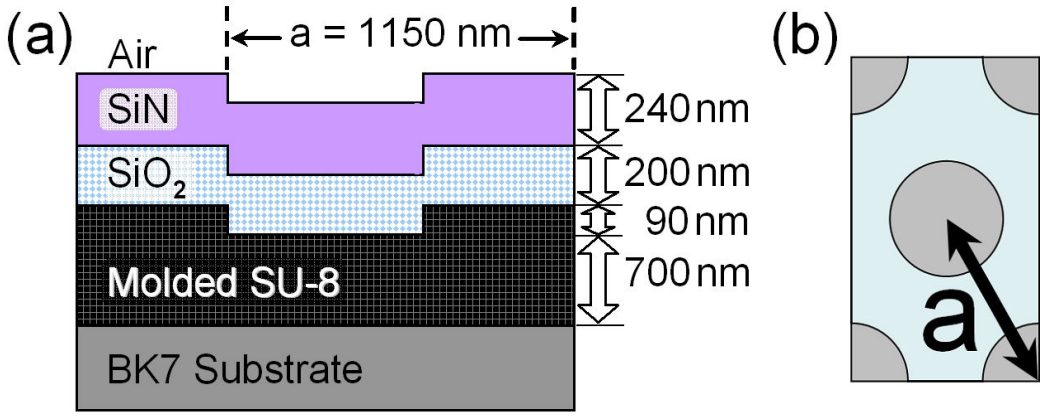

Fig. 3.1. (a) Cross section of GMR structure design with layer parameters. (b) Top view of hexagonal grating design.

A MATLAB based implementation of RCWA was used for simulation to select appropriate design parameters [34, 35]. Parameters such as dielectric layer thickness and grating dimensions typically serve as adjustable parameters that help the designer select for a particular resonance wavelength. However, due the nontraditional approaches used to generate these structures, fabrication related variation of these and other parameters must also be addressed.

For this design, fabrication imperfections that most significantly affect the resonance behavior are changes in thickness of the replicated SU-8 residual layer, deposited dielectric layers, and distortion of feature dimensions. Variation of these parameters must be understood to address sources of possible deviation in measured performance of GMR structures from designed structures. Of these parameters, the residual layer is the most likely to experience arbitrary variation during processing, due to the nature of the conformal processes used. Fig. 3.2 demonstrates the effect of residual layer variation on the resonance properties of the GMR. As the residual layer is increased, the resonant wavelength likewise increases, coupled with a slight narrowing of the resonant linewidth. Also, as residual layer becomes thicker, variation of this parameter has a lesser impact on

resonant properties. Another notable change is the introduction of a smaller secondary resonance. The secondary resonance follows the general behavior of the primary, but as residual layer increases, the separation between primary and secondary resonances decreases. Despite being a likely source of fabrication error, over the range of residual layer variation possible this parameter has a relatively moderate impact on the resonance properties of the GMR. With these factors in mind, a 700 nm residual layer was chosen for its compatibility with our molding process, strong resonance at 1550 nm, reduced sensitivity to fabrication errors and reasonable separation from the secondary resonance.

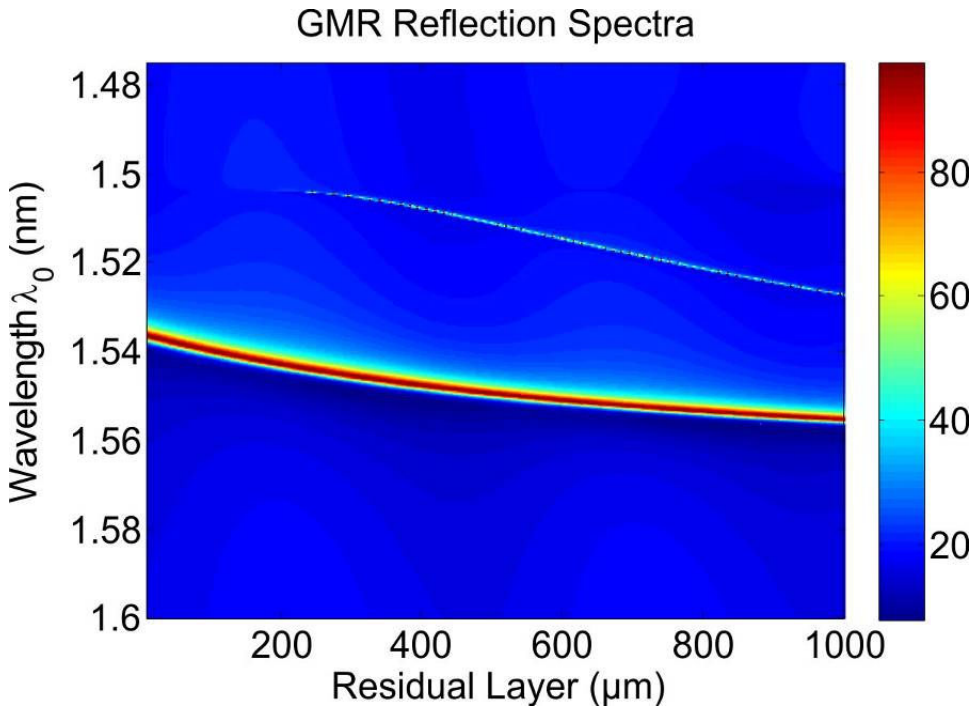

Fig. 3.2. Matlab simulation of GMR filter resonance behavior as a function of residual layer thickness, with other layer parameters specified in Fig. 3.1. Increasing the residual layer shifts the resonance wavelength toward the IR, though less so as the thickness is increased further.

The deposited dielectric layers have a significant effect on the GMR, however, they most likely will contain the least fabrication error due to the high quality deposition of the PECVD process. In Fig. 3.3 we can see that increasing thickness of SiN and SiO_2

layers have different results. An increase in SiN thickness strongly shifts the resonance toward the IR, while an increase of the SiO_2 layer moderately shifts the resonance toward the UV. Increasing the SiN layer drives the secondary resonance to further depart from the primary. However, the secondary resonance is observed to slightly approach the primary when increasing the SiO_2 layer. The SiN layer has a significant increase in linewidth until around the 240 nm mark where the rate of change is diminished. Changes in linewidth exist for the SiO_2 layer, but are relatively small over the range of variation possible in the deposition process. Because these parameters are the least likely to experience fabrication error, adjustment of these thicknesses can be leveraged to correct for resonance shifts caused by other sources of error.

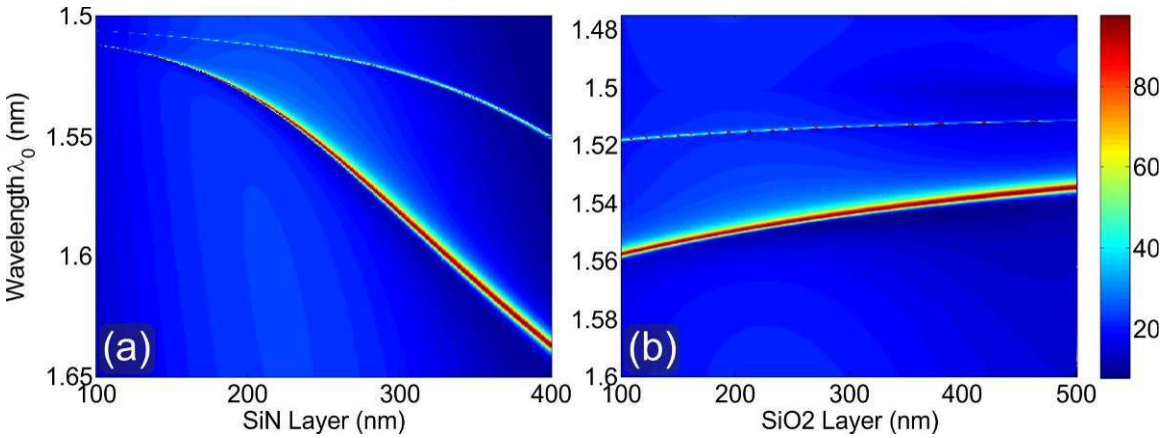

Fig. 3.3. Matlab simulations of GMR resonance behavior as a function of dielectric layer thickness, with other layer parameters specified in Fig. 3.1. (a) Increase in SiN shifts resonance to IR. (b) Increase in SiO2 shifts resonance to UV.

Another source for altering resonance behavior is variation in replicated feature dimensions. Due to the nature of the conformal process, this variation is likely, however more predictable than residual layer variation. We examine the trends of grating lattice constant variation here, with possible causes discussed in later sections. As can be seen in Fig. 3.4, increasing the lattice constant has a nearly linear increase in resonant

wavelength for our structures, with little change in linewidth or separation from the secondary resonance. Out of the parameters considered here, variation in lattice constant is observed to have the largest impact on resonance relative to the percent change in dimension of the respective parameters modeled.

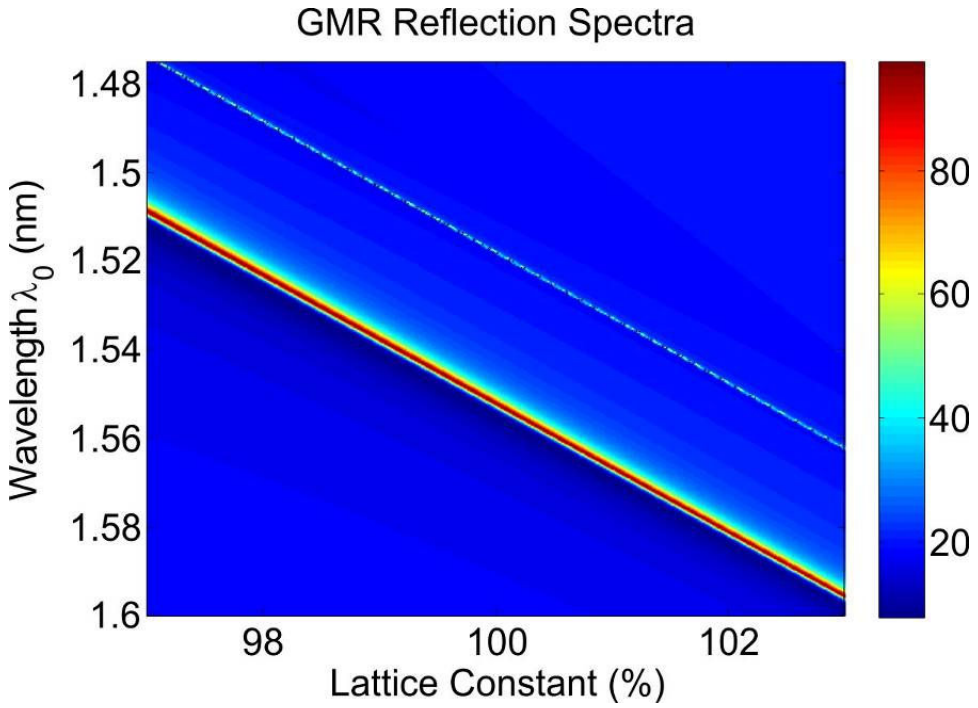

Fig. 3.4. Matlab simulation of GMR resonance behavior as a function of grating lattice constant, with other layer parameters specified in Fig. 3.1. Increase in lattice spacing provides a near linear increase in resonance wavelength.

With the various factors discussed above taken into consideration, a GMR design with a 700 nm SU-8 residual layer, an SiO2 thickness of 200 nm and a SiN thickness of 240 nm was selected. Using the MATLAB based RWCA code, resonances for normally incident TE and TM polarization are predicted at 1550 nm [34, 35]. A graph of predicted resonance peaks for a GMR with these design parameters is shown in Fig. 3.5.

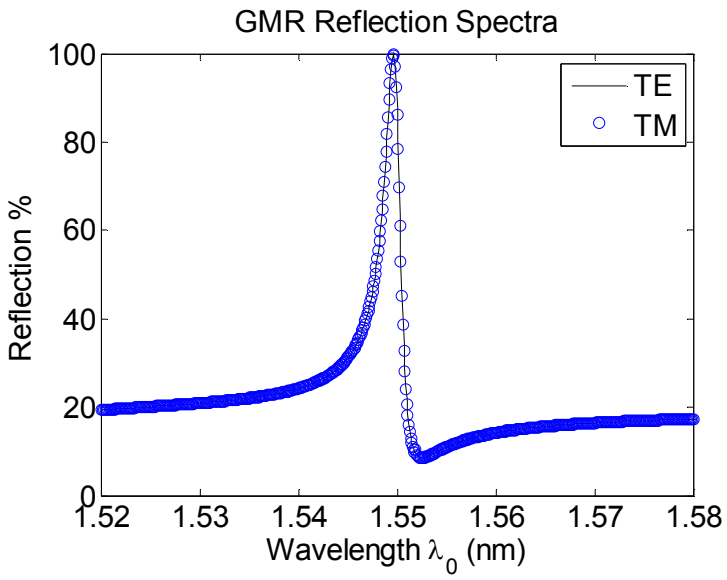

Fig. 3.5.Matlab simulation of reflection spectra for TE and TM polarizations incident on polarization insensitive GMR filter configuration with parameters as shown in Fig. 3.1.

3.3 Fabrication methodology

The high degree of flexibility of "conventional" polydimethylsiloxane, or Sylgard 184 PDMS makes it commonly used for conformal mold templates. However, this flexibility can lead to feature deformation, especially for small structures. To address this issue, composite PDMS and high compression modulus or "hard" PDMS (h-PDMS) mold templates were developed by Odom *et al* and were shown to improve pattern transfer fidelity while retaining the conformal properties of PDMS [106]. In the following processes we replicate GMR patterns from fused silica masters using PDMS/h-PDMS composite molds with hard backing (HB) using an embossing process, and free standing flexible composite molds (Flex) using a micro-transfer molding process. The embossing process enables controlled and consistent residual layers and the rigid backing reduces mold distortion during replication. We use the HB process to generate high fidelity replicas on flat substrates to serve as a baseline for comparison. The second method

employs the composite molds but does not use a rigid backing, leaving the molds flexible for conformal processing.

Composite mold fabrication begins with preparation of h-PDMS. A solution of 3.4 g of trimethylsilyl terminated (7-8% vinylmethylsiloxane) (dimethylsiloxane) copolymer (VDT-731, Gelest), 18 μL of platinum catalyst (platinum divinyltetramethyldisiloxane complex in xylene, SIP 6831.2LC, Gelest), and 36 μL of 2,4,6,8-tetramethyl-2,4,6,8-tetravinylcyclotetrasiloxane (396281, Sigma Aldrich) were mixed and degassed. After degassing, 1g of methylhydrosiloxane dimethylsiloxane copolymer (HMS-301, Gelest) was gently stirred into the mixture and degassed again. The mixture was then poured onto the master substrate, and spun for 40 seconds at 1000 RPM to generate an h-PDMS thickness of approximately 40 μm. The wafer was then placed in an oven for 30 minutes at 60° C. During this time PDMS (Ellsworth Adhesives) is mixed with a 10:1 elastomer base-to-curing agent ratio, in accordance with conventional process, and then degassed. After the h-PDMS has baked for 30 minutes, the PDMS is poured over the still tacky h-PDMS. For a composite HB mold, a fused silica backing wafer is added at this point. The setup is then placed in an oven and baked for at least 4 hours at 60° C. After full crosslinking of the composite PDMS mold, the setup is pulled from the oven and the mold is separated from master features.

The general process flow for the embossing technique used by the HB molding process is discussed in detail in Chapter 2 and shown in Fig. 2.1. For the GMR replication process described here, first a layer of SU-8 2000.5 is spun onto a 50 mm by 75 mm rectangular BK7 glass substrate for 50 seconds at 1000 RPM. The wafer is then soft baked for 1 min 30 seconds at 95° C. After soft baking the wafer is cooled, and the

mold template is brought into contact with the SU-8. The wafers are placed in a vacuum chamber and the chamber is evacuated. The wafers are then removed from the vacuum chamber and placed in an oven for 45 min at 110 °C with a small weight (~1kg) placed on top. As the SU-8 temperature rises past its glass transition temperature (T_g = 50° C), the SU-8 becomes viscous and the features are embossed into the resist. The wafers are then removed from the oven, allowed to cool, and separated.

The Flex replication process (Fig. 3.6), uses a micro-transfer molding process leveraging the flexibility of the composite PDMS molds. This process is used to generate GMR devices on both flat and curved substrates, allowing us to examine any changes in GMR performance introduced by contoured surfaces.

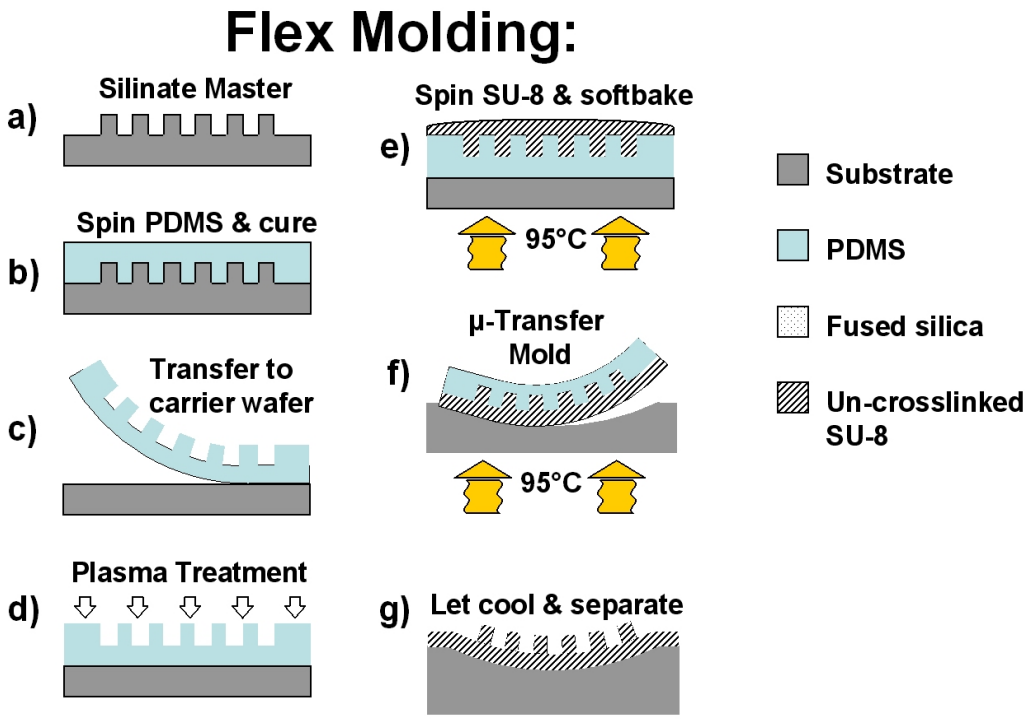

Fig. 3.6. Flex process for molding SU-8 resist on flat and contoured surfaces. (a) Master features are cleaned (b) Mold template of composite PDMS is spun and cured (c) Mold template is transferred feature side up to carrier wafer (d) PDMS composite mold template is exposed to oxygen plasma (e) SU-8 is applied, and soft-baked to remove excess solvent (f) SU-8 is micro-transfer molded at an elevated temperature onto substrate (g) Part is cooled and separated.

First, the 4 inch composite PDMS mold template is cut into 1 inch square sections. A single section is then placed feature side up in the center of a silicon carrier wafer and then treated with oxygen plasma to improve SU-8 spin uniformity. Both PDMS and h-PDMS have naturally hydrophobic surfaces, and exposure to oxygen plasma renders the surfaces hydrophilic. Process details for plasma treatment are discussed in previous work [107]. SU-8 2000.5 is then spun onto the piece for 50 seconds at 1100 RPM. After spin coating, the piece/carrier wafer and the substrate for transfer are placed on a hot plate set at 95° C. The SU-8 is soft baked for 2 minutes, then the coated piece is removed from carrier and applied SU-8 side down to the heated substrate. The SU-8 is micro-transfer molded at an elevated temperature onto the substrate, to maintain the SU-8 in a fluid state above its glass transition temperature. After application the substrate remains on the hot plate for an additional 2 minutes to anneal the SU-8 and further minimize cracks and stresses. We used diced pieces of flat BK7 glass substrate for the "Flex Flat" and a 1-inch diameter BK7 concave lens with 32.4 mm radius of curvature (ROC) for the "Flex Curve" parts. The pieces are then removed from the hotplate, allowed to cool, and the flex mold is peeled from the substrate, leaving the replicated features.

After patterns have been transferred to their respective substrates, the SU-8 must be fully crosslinked prior to the deposition process (Fig. 3.7(a)), to prevent resist reflow. An exposure of 12 seconds at 13.2 mW/cm^2 is performed on a Quintel Ultraline 4000 contact aligner. The pieces are then post exposure baked (PEB) for 2 min at 95° C on a hot plate. After PEB, the pieces are then hard baked for 10 minutes at 300° C on a hot plate. Following crosslinking and hard baking of SU-8 patterns, the pieces were coated with 200 nm of SiO_2 and 240 nm of SiN using PECVD. The platen temperature for both

depositions is set to 300° C. Images of the resulting devices are shown in Fig. 3.7(b), Fig. 3.8 and in Fig. 3.9.

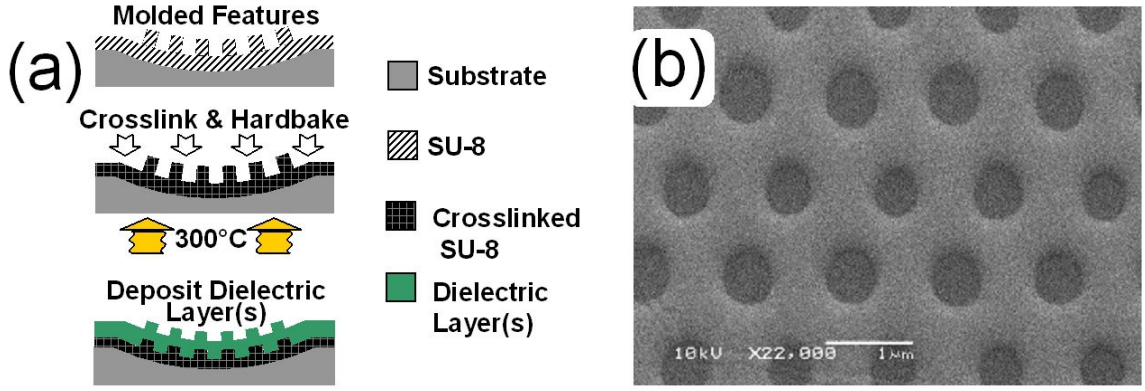

Fig. 3.7. (a) Preparation of molded SU-8 features for deposition by UV exposure, PEB, and 300° C hard bake followed by PECVD to generate dielectric layer coatings. (b) SEM image of hexagonal grating pattern after coating by PECVD to form a GMR device.

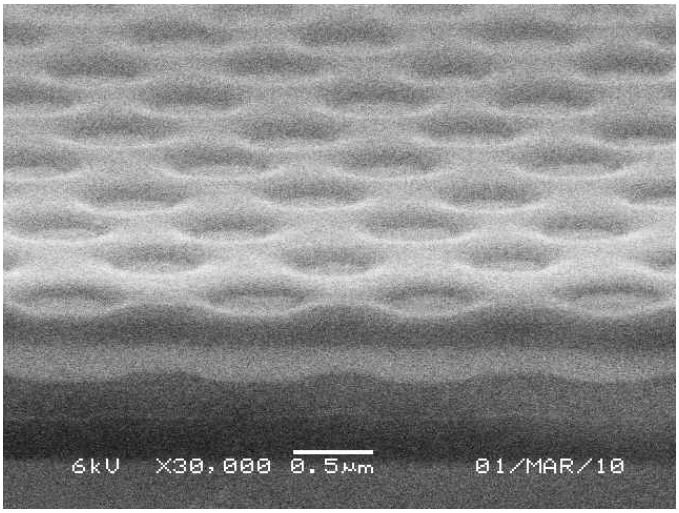

Fig. 3.8. SEM image of representative GMR structure fabricated on silicon wafer for cleaving and cross sectional view of deposited layers.

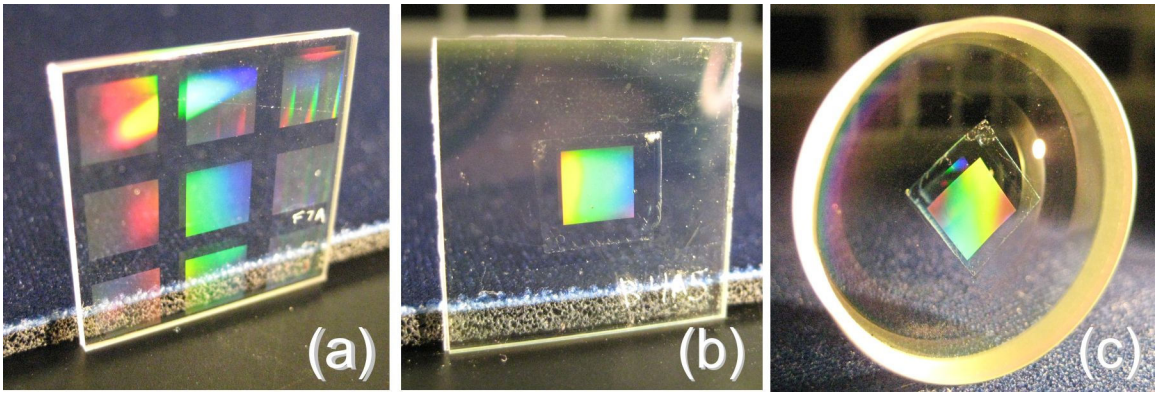

Fig. 3.9. Camera images of GMR devices fabricated on (a) flat using Hard Backed embossing process; on (b) flat and (c) concave lens (ROC = 32.4 mm) using Flex micro-transfer process.

3.4 Test setup

Due to the unconventional nature of the curved GMR parts, a custom testing apparatus was required to quantify device performance. The setup needed the ability to measure flat and curved parts to facilitate meaningful comparisons of the devices. To simplify the testing assembly and to mimic the application for which the devices are intended, we chose to measure the reflectivity of the GMR structures. A simplified diagram of the test setup is shown in Fig. 3.10 with pictures of the alignment setup shown in Fig. 3.11.

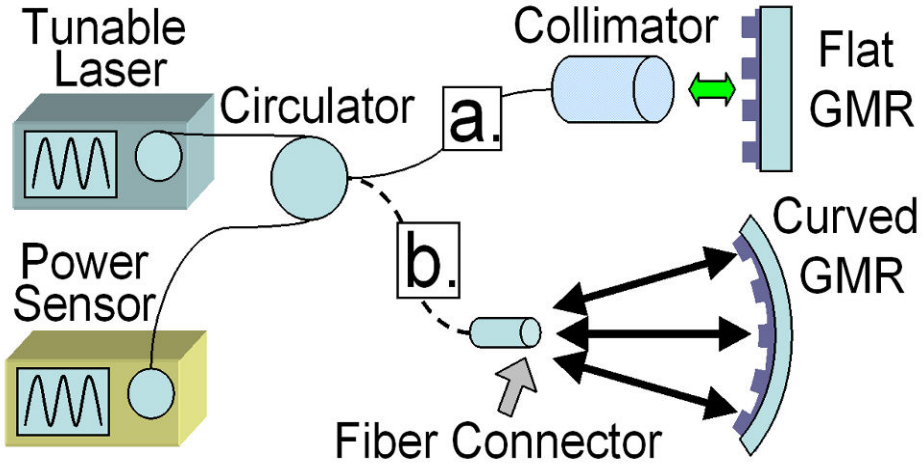

Fig. 3.10. Simplified diagram of setup used to measure reflectivity from (a) flat and (b) curved parts.

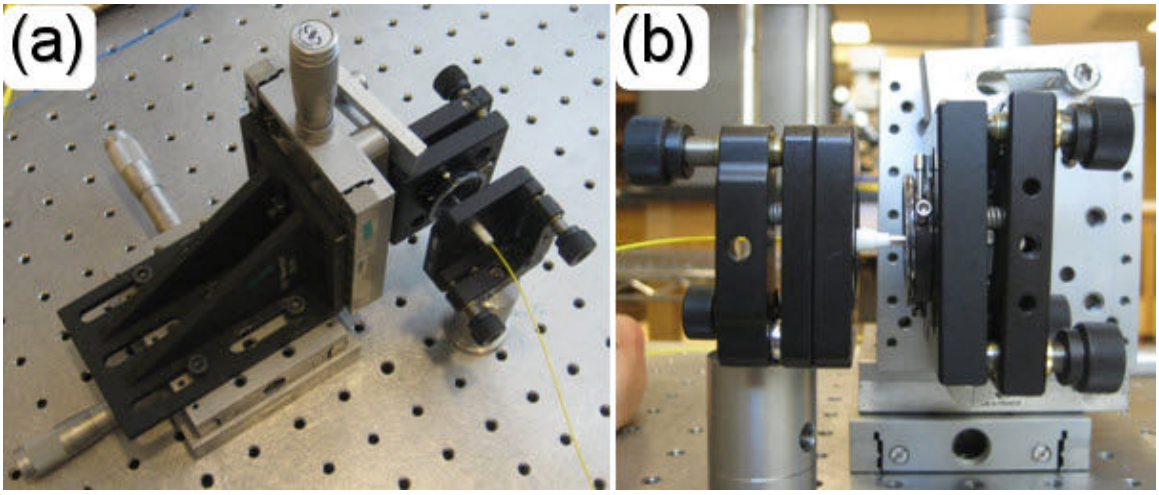

Fig. 3.11. Images of configuration used to align curved parts with (a) x, y and z and (b) tip tilt adjustment with variable aperture.

An Agilent 8164A tunable laser is used as the source, coupled with an Agilent 81636B power sensor. Light exits the tunable laser, and then passes through single mode SMF-28 fiber. An inline optical circulator is used to isolate transversely propagating modes. To measure flat structures, light exiting the fiber is collimated using a pigtail style fiber collimator (OZ Optics) with a collimated beam size of 220 um. Reflected light travels back down the fiber through the circulator to the power sensor. To test curved structures, the fiber is terminated at a fiber connector to approximate a point source generating spherical waves. The concave GMR device (ROC = 32.4 mm) is placed at a distance to match the emerging wavefront to the curvature of the device, in effect locally approximating a flat GMR over finite areas. The beam size is reduced to a diameter of 3.8 mm by an adjustable iris to eliminate illumination of unpatterned areas of the part. Experimental measurements use a combination of TE and TM polarization due to lack of polarization maintaining fiber.

Prior to GMR testing, we made measurements to quantify the system losses involved with the setup and verify proper function. When configuring the test setup the primary

source for uncertainty between measurements was from connecting and disconnecting the fiber optic connectors to switch between flat and curved testing configurations. An in-depth analysis of system losses and the fiber connector-related uncertainty is discussed in Appendix B.

To remove the uncertainty discussed in Appendix B when connecting/disconnecting fiber connectors, we chose to avoid this possibility and take data off a reference surface after each device measurement. To maintain consistency and to provide a meaningful comparison for the different configurations, measurements were referenced to a gold mirror on the same surface type for each case. For the flat GMR parts, this was straightforward, due to the robust nature of the alignment involved. The flat measurement setup has two factors that benefit it in this respect. First, the width of the collimated beam emitted from the flat measurement setup remains relatively constant over the range of possible z values, as shown in Fig. 3.12(a). Second, the width of both the beam and the collimator aperture is reasonably large. This ensured rough alignment of the part provided enough measured power to register on the Agilent 81636B power sensor. As a result, parts could be interchanged in the setup, and the peak could be re-located using the Agilent tunable laser and power sensor alone. However, for the curved GMR parts, the beam varies in width as a function of z, focusing down to a very small spot at the location of peak reflected power (Fig. 3.12(b)). Therefore, when the GMR part is changed out for the gold mirror, the slightest misalignment will render the power too low to register on the Agilent power sensor, and will make location of the reflected beam excessively challenging. To locate the beam, a higher power broadband source (AFC Technologies BBS 15/16D -TS Ultra broad high power fiber source) was coupled with a more sensitive

optical spectrum analyzer (Agilent 86142b). These tools were restricted to only locating the beam due to an insufficient spectral range needed to make the measurements for device characterization. To avoid connector uncertainty when changing the power and measurement devices, we used a set of optical splitters, shown in Fig. 3.13. The splitters were arranged to allow use of either test arrangement without making or breaking any connections to ensure direct comparison of each measurement to gold surfaces. Measurement results presented herein show values with system losses removed, therefore focusing only on the performance of the GMR filters themselves

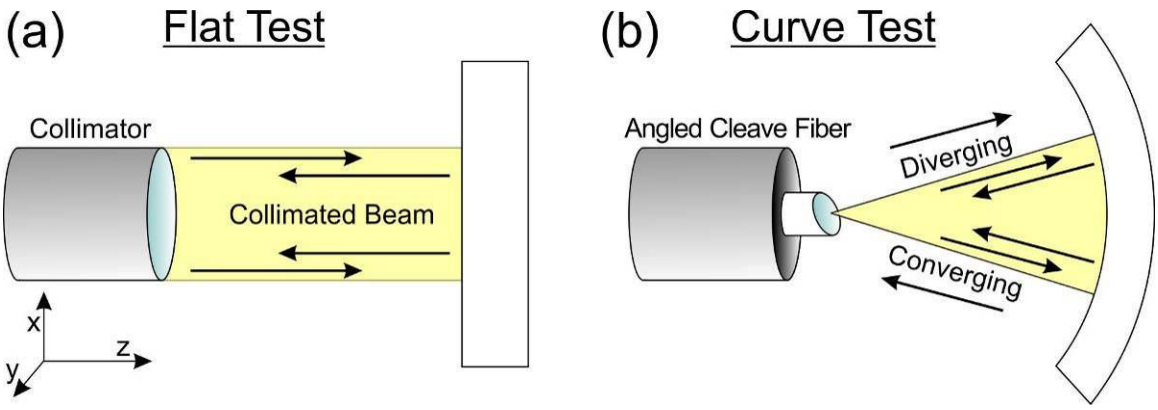

Fig. 3.12. (a) Diagram of collimator used in flat test arrangement. A wide, consistent beam ensures robust alignment. (b) Curve test arrangement with angled cleaved fiber used to approximate a point source. Slight misalignment in any dimension will cause significant disruption of measured signal.

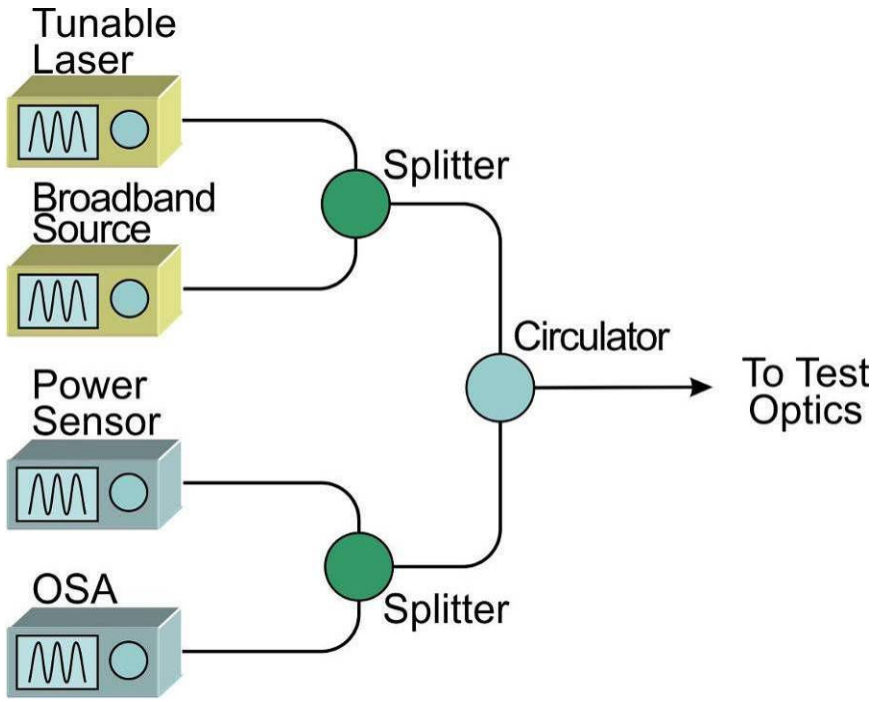

Fig. 3.13. Diagram of splitter arrangement used to ensure successful alignment without breaking any connections. Only a single source/sensor pair is used concurrently.

3.5 Measurement and characterization

With the characterization of the experimental system complete, we performed measurements of the three different samples; the flat hard-backed GMR as a baseline reference, the flat GMR from a flexible mold, and the curved GMR from the flexible mold. Experimental data shown in Fig. 3.14 are averages of three measurements for each structure, with an associated standard deviation below 1% for peak reflectivity. The possible causes of observed changes in resonant behavior from modeled values are discussed below. We consider effects such as master structure imperfections, thermal and mechanical deformation of the mold, and mode profile in curved waveguides.

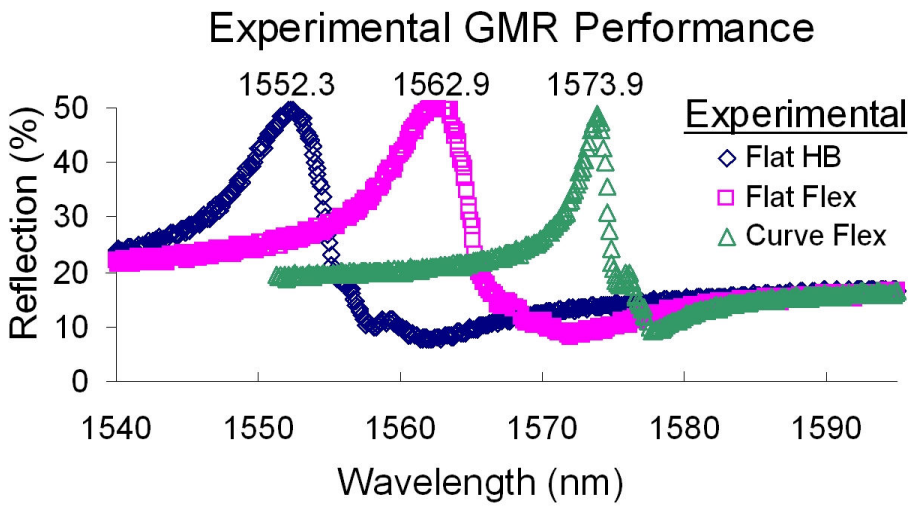

Fig. 3.14. Average measured GMR performance for different fabrication processes. Resonance peaks are labeled in nanometers.

Theoretical models assume perfect structures; however SEM and AFM measurements show some variation in the master pattern lattice constant and hole diameters, resulting in broadened linewidth and reduced peak reflectivity. The simulated HB data uses an adjusted grating period of 1152.1 nm to match the experimentally determined peak at 1552.3 nm and to provide a relative baseline for comparison of the Flex molded parts. A shift in measured resonance wavelength is apparent for the Flex process on both the flat and curved surfaces. The lack of rigid backing helps to explain the shift in resonance for the Flex process on a flat surface. Without a rigid backing the mold will expand freely with differences in temperature. The coefficient of thermal expansion (CTE) of PDMS suggests the mold will expand by ~1.08% when subjected to the temperature swings of the Flex molding process. In the case of the HB mold, some expansion may still occur, but it will be reduced laterally by the rigid glass backing. Characterization of rigid backed molds combined with calculated CTE values suggest the HB GMR period will expand by ~0.27% during molding. The disparity in expansion

values leads to an increased Flex GMR period relative to the HB; if we increase the period of the structure used to model the HB generated replica by 0.81% to 1161.4 nm, the wavelength of the modeled peak resonance shifts to 1563.9 nm, within 1 nm of the experimental resonance at 1562.9 nm.

The curved GMR displays a further shift in resonance beyond that introduced by the Flex molding process on a flat, as well as narrowed linewidth in comparison to the other measured structures. To account for these differences we consider the two most influential factors, distortion of the structure due to mechanical deformation, and the mode profile generated by a curved waveguide. Change in feature dimensions due to deformation of the mold template is approximated with geometric calculations for changes in arc length associated with material bending. When a beam of material is bent, the interior side of the beam compresses, the peripheral side experiences tension and the neutral axis experiences neither [108], as seen in Fig. 3.15. The resulting feature distortion caused by Flex molding on concave surfaces can be quantified with the equation below, where l(n) is the length of the neutral axis (length of the part in its uncompressed state), r(o) is the radius of the part the mold template is being conformed to, d is the thickness of the mold, and l(o) is the resulting length of the stretched side with features.

$$l(o) = r(o)\left(\frac{l(n)}{r(o) - d/2}\right) \qquad \text{Eq. (3.1)}$$

Fig. 3.16 shows the effect this can have on feature dimensions over a range of part curvatures and mold template thicknesses. For our part, this effect increases lateral feature geometry of the GMR by an additional ~1.46%, and when combined with the

increase in period described above for the Flex mold process increases the modeled resonance to 1585.3 nm.

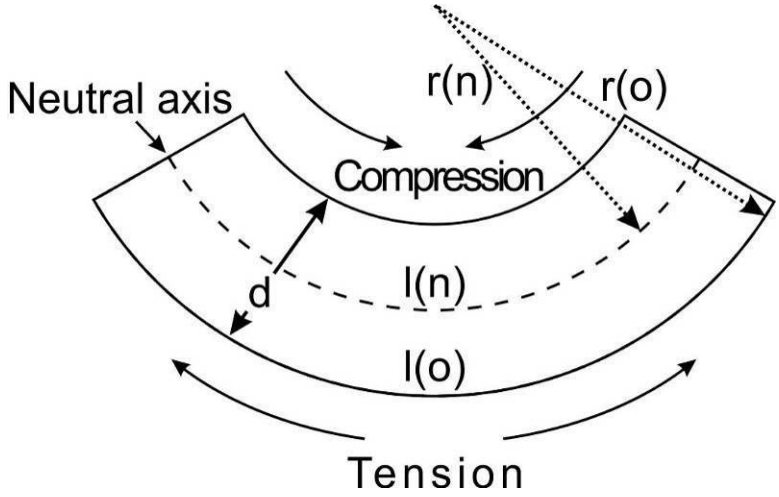

Fig. 3.15. (a) Diagram of beam undergoing bending. Features on the peripheral side of the bend experiencing tension lengthen, while features on the interior side shorten.

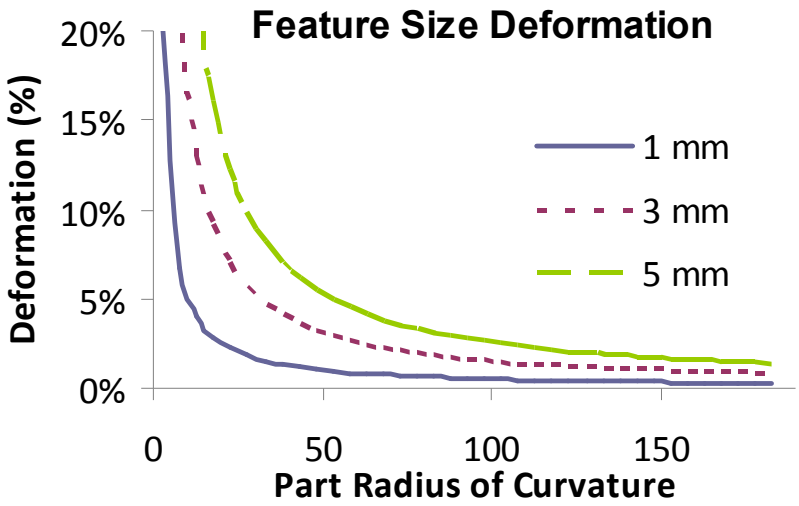

Fig. 3.16. Calculated percent of feature deformation as a function of concave substrate's radius of curvature and mold template thickness.

In addition to this effect however, a curved waveguide has a distorted mode profile, with the eigenmode field distribution being shifted toward the outer edge [109]. For a GMR, this outward shift reduces the grating interaction, thereby decreasing the rate at which light is coupled out of the propagating mode. This increases the distance the mode

will travel inside the waveguide, resulting in an increased grating interaction length, and decreased linewidth [110]. In order to qualitatively evaluate the effect of the distorted mode profile on GMR performance, we change the waveguide parameters in our simulation to shift the mode profile toward the "outer edge" of the waveguide thereby increasing the grating interaction length in a similar manner. This is approximated in the RCWA code by decreasing the SiN (core) refractive index [111]. A decrease of 2.34% (change from n = 1.9240 to 1.8790) results in a decrease in modeled resonance wavelength (to 1573.9 nm) and narrowed linewidth, closely matching the measured value (Fig. 3.17). This effect should be consistent for both polarizations due to the symmetry of the part.

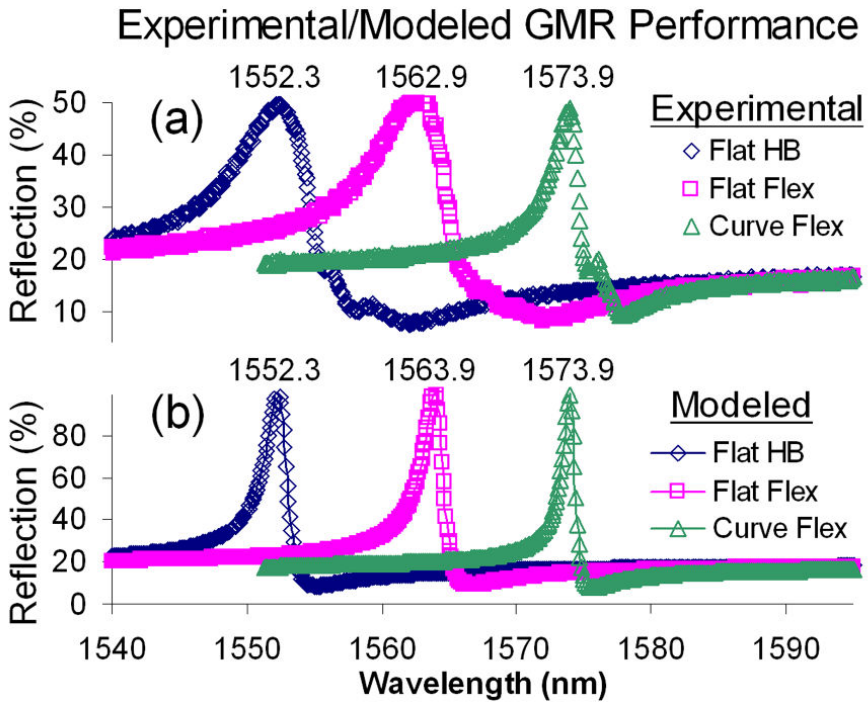

Fig. 3.17. (a) Average GMR performance for different fabrication processes. (b) Modeling results with assumptions described in text. Only TE polarization is shown for brevity since design is polarization insensitive. Resonance peaks are labeled in nanometers.

The modeled refractive index value was determined empirically, and thus only qualitatively supports a physical explanation for the change in GMR performance.

Dimensional changes due to mechanical deformation clearly have the largest impact on resonance wavelength. The mode profile distortion has the largest impact on linewidth, while also playing a lesser but significant role in reducing the resonant wavelength. Under these assumptions, increased curvature of the device should increase the resonant wavelength and decrease the linewidth further.

In summary, we have fabricated and characterized GMR filters on curved surfaces. Experimental measurements were compared with results from the same nominal GMR filters fabricated on flat substrates to gain understanding of effects on performance due to the curved surface and processing approach. The ability to generate sophisticated micro-optical devices on curved surfaces is a significant step towards new types of functional integration not achievable with conventional methods.

CHAPTER 4: LENS STRUCTURING FOR COMPOUND LENSES

4.1 Overview

In the pursuit to generate biomimetic optics, the challenges associated with generating micro and nano-optics on a surface with any amount of curvature can be quite formidable. However, to fabricate designs that approach the actual construction of biological designs such as the moth or shrimp eye where structural integration is paramount, curved parts must be replaced by parts with compound curvature. With this in mind, the process to inexpensively fabricate a compound lens was investigated. Having this ability gives us the potential to integrate more complex functions onto individual lenslets as fabrication processes evolve. In this chapter we discuss combination of conventional convex lens elements with lenslet arrays to form compound lenses inspired by "fly eye" structures found in nature. To fabricate the compound lens, flexible SU-8 molding techniques discussed in Chapter 3 are used to transfer replicas of a commercially available lenslet array onto macro-scale lenses. A free space scale part was chosen to enable characterization of imaging quality using conventional imaging equipment. Our design goal was to generate a compound lens capable of focusing multiple images onto a visible wavelength CCD detector simultaneously. We discuss structure design, fabrication techniques and challenges, and imaging performance of the resulting devices.

4.2 Compound lens design

To create a functioning and testable free space compound lens, aspects of fabrication and measurement such as lens specifications, CCD placement and size, and changes in feature dimensions due to the molding process were critical in generating an appropriate design. For selecting the appropriate lens/lenslet specifications, we took into account that a small lenslet with moderate sag will inherently have a short focal length. This can create a significant challenge if the lenslet is positioned on a macro-scale lens, as the imaging plane of the lenslet may form within the macro-lens itself. To avoid this issue, the lenslet ROC can be decreased, increasing the focal length. However, this can dramatically increase the f-number *N* of the lens. The f-number is a ratio of the focal length *f* to the diameter *D* of the lens, as given by the formula below [32].

$$N = \frac{f}{D} \qquad \text{Eq. (4.1)}$$

Increasing the f-number can significantly increase the diameter of the diffraction limited spot size (*d*), as shown in the formula below [32].

$$d \approx 2.44 \frac{f\lambda}{D} \qquad \text{Eq. (4.2)}$$

To compromise and generate lenslets with an appropriate f-number for a fixed focal length, the lens diameter can be increased. Selecting the lens specifications with the restrictions discussed above are also coupled with the size and placement of the camera detector. Desired parameters will focus images from multiple lenslets onto the detector simultaneously, placing requirements on lens size and focal length. The available camera for characterizing the imaging performance over the visible, a UNIQ (UP-900-12B), has

its CCD detector recessed approximately 19 mm into the detector's housing (Fig. 4.1). Assuming we need approximately 3 mm for mounting and alignment of the finished part, this means the back focal length for the compound structure must be 22 mm or greater. The detector has a functional area of 4.8 mm high by 4.9 mm across, meaning to simultaneously image four lenslets, the image size of each lenslet should be approximately one fourth of that.

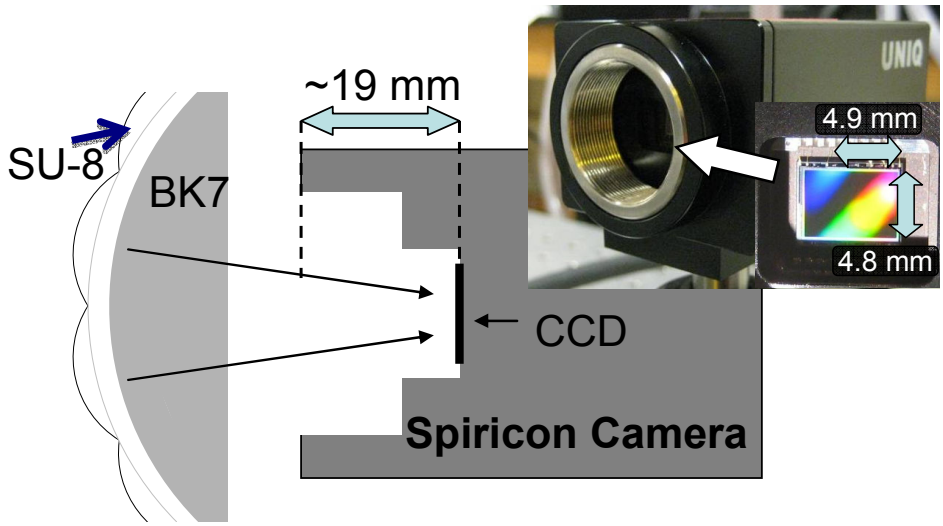

Fig. 4.1. Figure showing testing arrangement available to measure compound lens performance. Restrictions imposed by the CCD detector placement and size, had to be understood to properly image multiple lenslets simultaneously. Picture of camera used is shown inset.

Before creating our compound design, one more factor need be considered, the impact the fabrication process has on final structures. For a nano scale structure placed on a macro-scale lens, that structure will only experience a very small portion of the curvature of the curved surface it is molded onto. This allows us to locally approximate the substrate this nano-scale structure is fabricated on as planar. However, for larger structures this approximation is not necessarily valid. For these structures, the conformal nature of the micro-transfer molding process can have a significant impact on replicated

feature dimensions. For spherical lenslets being fabricated on macro-scale spherical lenses we can approximate the effect this can have by combining the sags of each lenses as shown in Fig. 4.2.

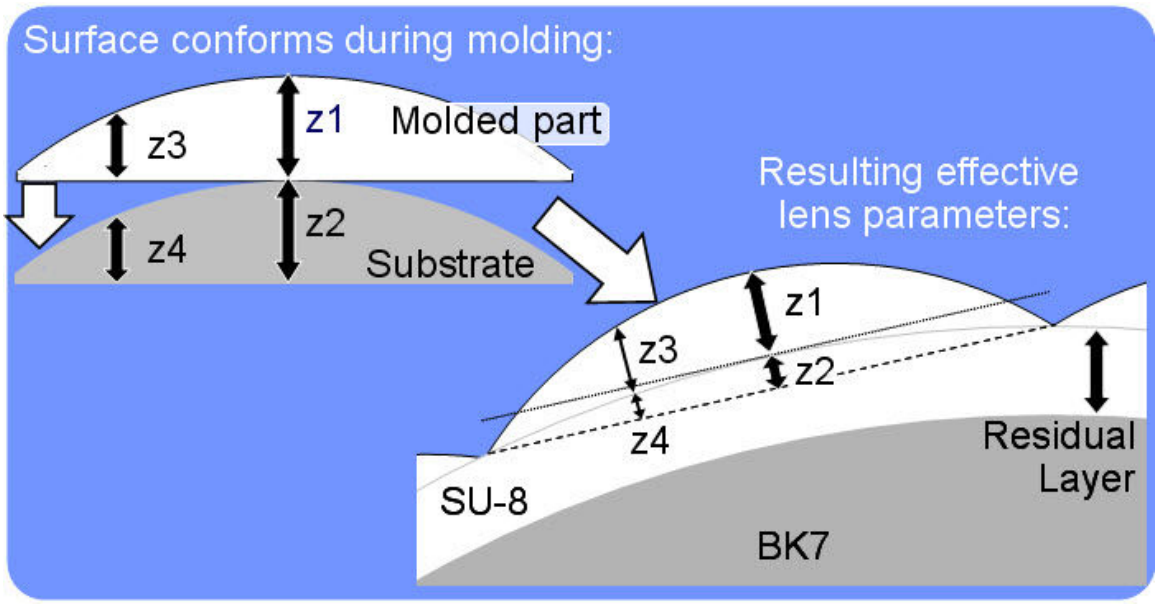

Fig. 4.2. Variation in lenslet SAG due to the conformal molding process must be accounted for to properly design the compound lens structure. As the molded lenslet conforms to the substrate curvature the resulting lenslet dimensions can be approximated by summing the SAG values of each respective lens.

With the design requirements taken into account, we then selected commercially available parts that would best accommodate desired specifications. A commercially available 46 mm by 46 mm lenslet array from Edmund Optics was chosen to serve as a master for the molded lenslet patterns. Each rectangular lenslet is 3 mm by 4 mm, has a ROC of 20 mm, diagonal SAG of 157 µm, and a focal length of 38 mm. We combined this array with a 25.4 mm diameter macro-scale lens from Thor Labs with a ROC of 51.5 mm, SAG of 1.5 mm, and focal length of 100 mm. A geometrical model to represent the finished structure (Fig. 4.3) was generated in ZEMAX using code written in MATLAB to specify spatial and angular position parameters for each lenslet. The combined ROC for each lenslet is 14.47 mm giving the structure a back focal length of 22.6 mm. Due to the

focusing effect of the macro lens, each lenslet occupies a 2.32 mm by 3.1 mm footprint on the CCD detector, approximately the size required to fit four complete images on the detector simultaneously.

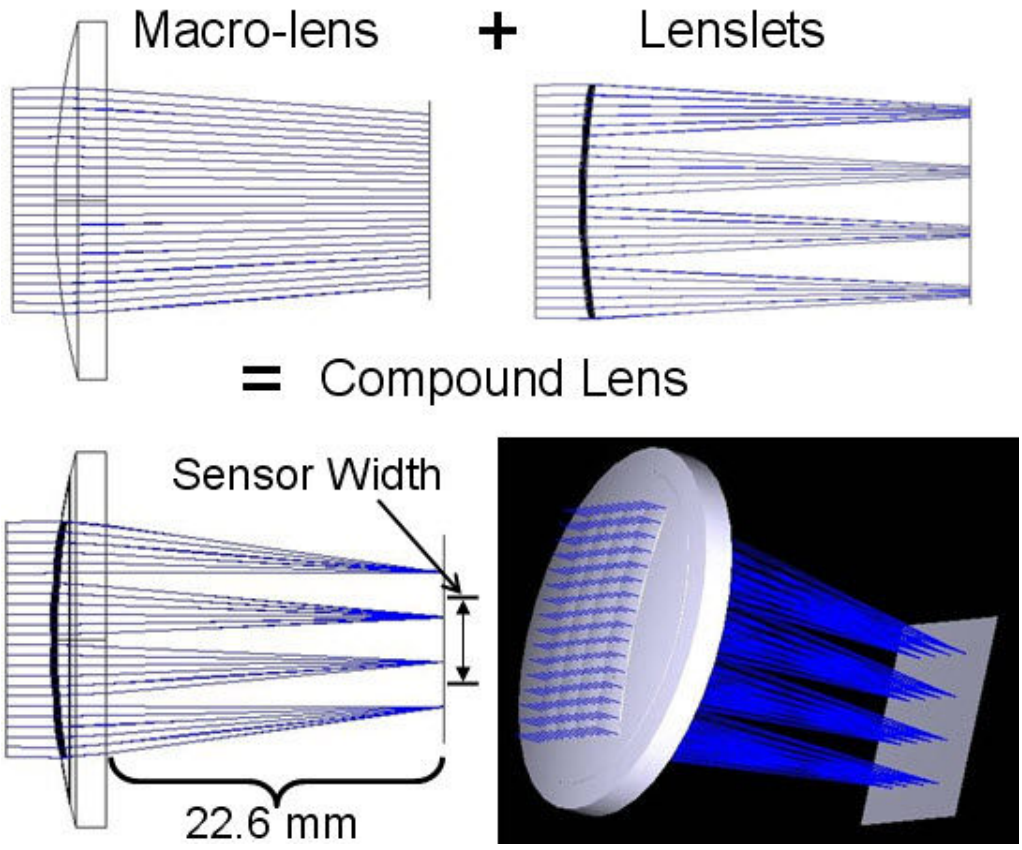

Fig. 4.3. ZEMAX models for the compound lens structure combine the macro-scale lens with lenslets. MATLAB code was written to select the spatial and angular parameters for each lenslet element. The combined structure has a back focal length of 22.6 mm, sufficient for our testing apparatus. A 3-d shaded model is shown for perspective.

4.3 Compound lens fabrication

Our fabrication process for the compound lens borrowed heavily from processes used to generate the conformal spectral filters discussed in Chapter 3. The flexible PDMS micro-transfer or FLEX process was modified as discussed below to accommodate for the increased resist thickness needed to fill the lenslet arrays. To fabricate the composite

device, first we generate a flexible replica of the lenslet array. Master lenslets are silinated in a vacuum oven for 1 h at 100 °C with Aquaphobe to facilitate separation from replica molds. Sylgard 184 PDMS is mixed with a 10:1 elastomer base-to-curing agent ratio, in accordance with conventional process, and then degassed [5]. The elastomer is then poured onto the substrate, placed in an oven at 60°C and cured for at least 4 hours. After curing, molds are peeled from master features, diced to fit a macro-lens, and then transferred to a carrier wafer. The PDMS is then treated with oxygen plasma to change the surface energy to allow for uniform wetting of SU-8 poured onto the structure. SU-8 2025 is spun at 800 RPM and then soft baked at 65° C for 5 min, followed by a 95°C soft bake for 30 min. The macro-lens is pre-heated to 95°C, as well as a lens with concave dimensions complimentary to the ROC of the plano-convex substrate. The SU-8 coated mold is then transferred to the substrate, and the complimentary lens is then placed on top of the flexible mold to facilitate conformal contact. The SU-8 is maintained at an elevated temperature above its glass transition temperature to ensure the polymer remains in a fluid state during the transfer process. The parts are left in place on the hot plate for a short time (~2 min) to anneal the SU-8 and further minimize cracks and stresses. The assembly is then removed from the hot plate, allowed to cool, and the components separated, leaving the molded features on the substrate. A camera image of the resulting structure is shown in Fig. 4.4.

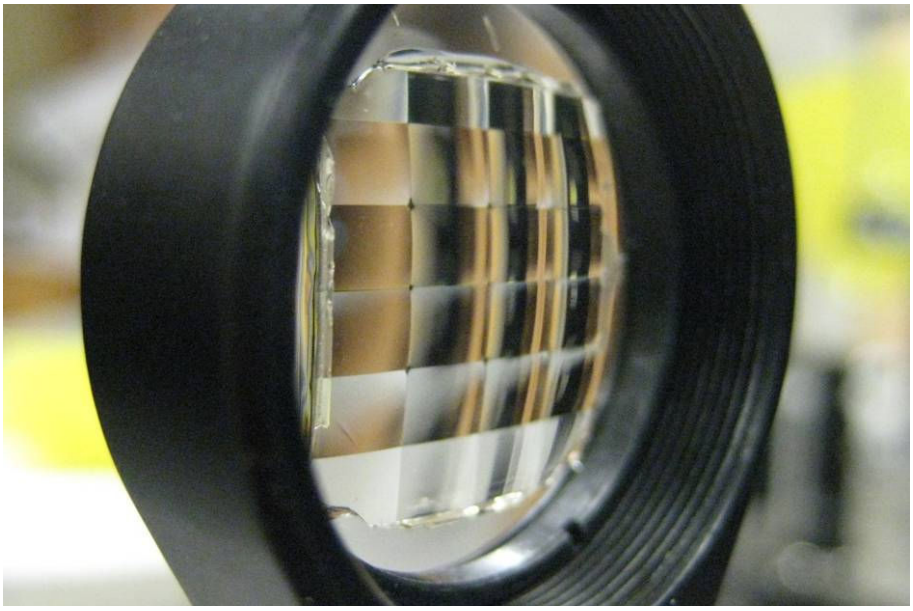

Fig. 4.4. Camera Image of molded compound lens structure shows successful lenslet replication over macro-scale lens (ROC = 51.5 mm).

4.4 Compound lens performance

Once fabricated, a commercial SLR camera was used to take images of a single penny through the compound lens to verify the optic was functioning roughly as intended, as shown in Fig. 4.5.

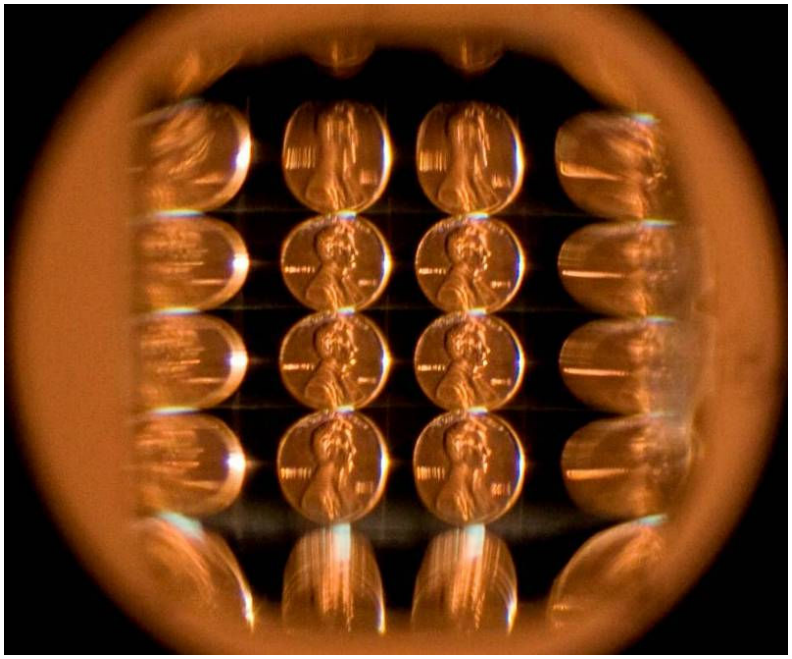

Fig. 4.5. Image of single penny through compound lens using a commercial SLR camera.

To more fully characterize the device, it was placed in front of our UNIQ CCD camera, and aligned to focus the center four lenslets onto the detector simultaneously. Our object was placed 65 mm in front of the array, and the resulting image is shown in Fig. 4.6.

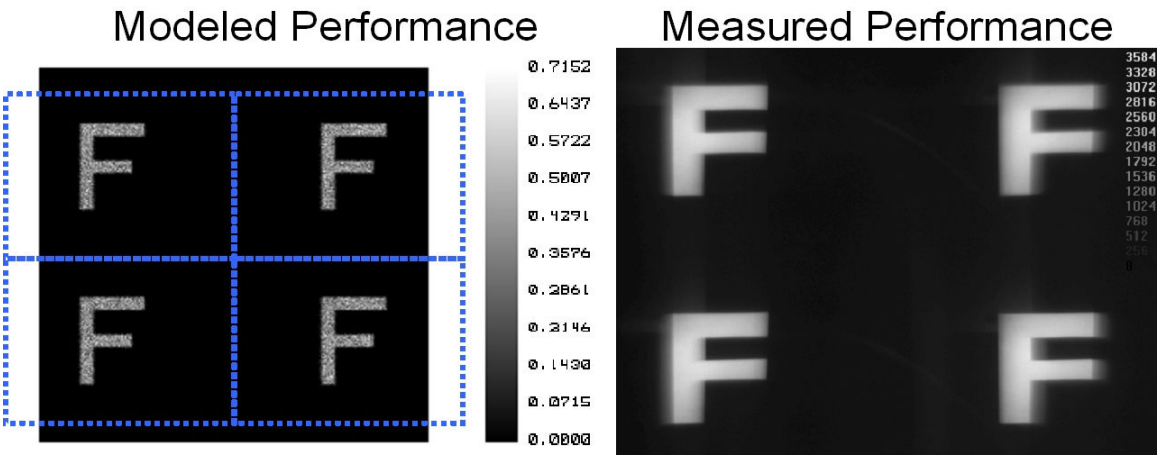

Fig. 4.6. Modeled performance for center four lenslets of compound lens compared with measured performance.

Image quality appears to suffer primarily from astigmatism, likely a result of the fabrication process. This belief was supported by lack of similar distortion in modeled performance or in measured images of master structures. To explain this, we examine the asymmetry of each lenslet. The SAG for each lenslet varies depending on the lens dimension over which the SAG is measured. Specifically, the SAG over the 3 mm dimension will be 56 µm, the 4 mm dimension will be 100 µm, and over the diagonal dimension will be the full 157 µm. The spun SU-8 thickness for our process should be around 100 µm, leading to a disparity for the "deepest" parts of the lenslets. During the spin coating process, this asymmetric disparity may lead to resist coating asymmetry over the lenslets. Thicker formulations of SU-8 are available and could quite possibly address issues related to resist thickness. However, SU-8 2025 was the thickest we had available.

Despite this limitation, the conformal nature of the process suggested reasonable fidelity may still be achieved. To quantitatively evaluate the molding fidelity we measured the ROC of lenslets along their short and long axes. To do this, images of the compound lens surface were taken with confocal scanning laser microscopy (CLSM) performed by an Olympus LEXT OLS4000 microscope (Fig. 4.7). Measurements were taken fitting the lenslet structures to spherical curvature, using the center and outer edges as three points to evaluate ROC. Using this technique we observed ROC variation dependent on lenslet axes. The average measured ROC for the center four lenslets along their short axis was 14.6 mm, and along their long axis was 15.3 mm. The variation of 0.7 mm is large enough to impact imaging quality as shown in Fig. 4.8, where a simulated image for an anamorphic lenslet is observed to more closely match measured images from Fig. 4.6. For reference, the measured flat master ROC for both axes was 20.4 mm. The predicted ROC for molded structures was 14.47 mm, suggesting reasonable fidelity over features with sufficient resist thickness.

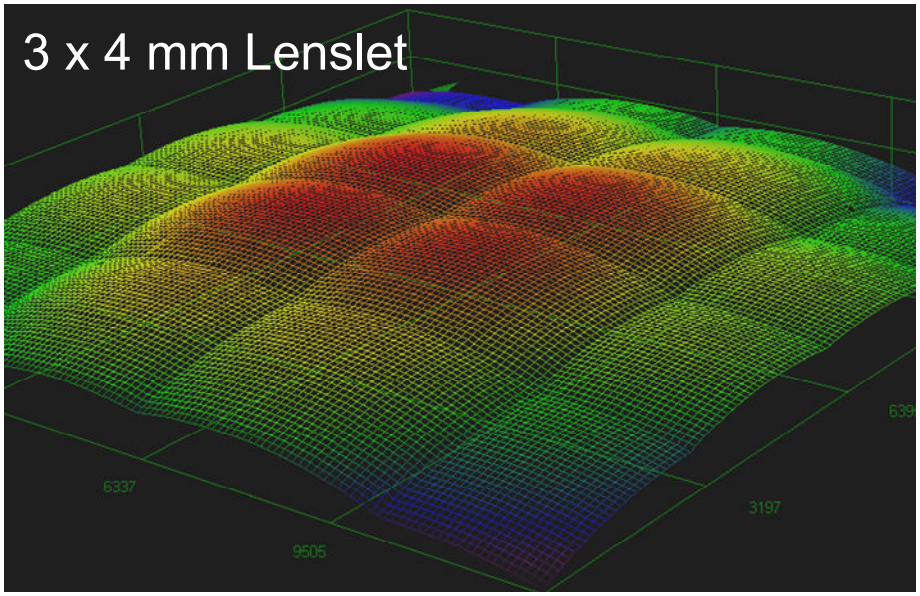

Fig. 4.7. CLSM measurement of molded compound lens structure used to evaluate lenslet replication fidelity over macro-scale lens.

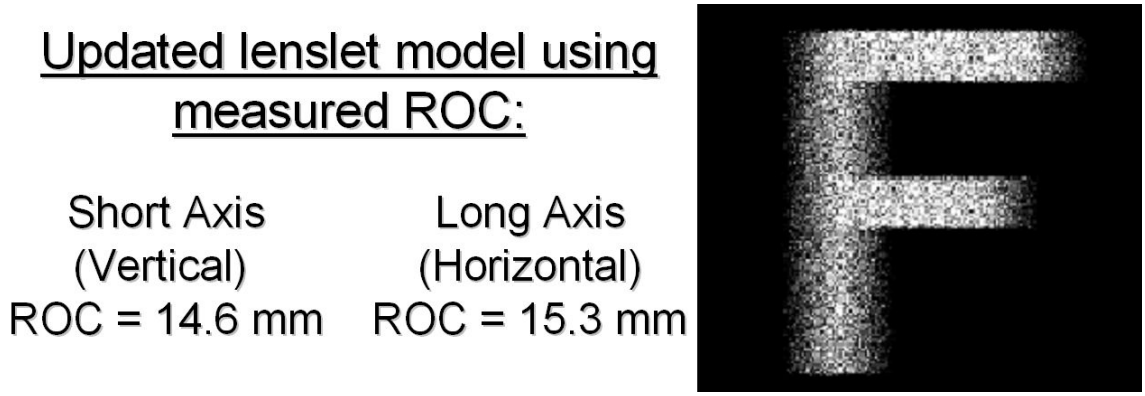

Fig. 4.8. Simulated image for anamorphic lenslet with ROC of 14.6 mm for short (vertically) oriented axis and 15.3 mm for long (horizontally) oriented axis at imaging plane for 14.6 mm ROC.

To examine whether astigmatism at the outer portions of each lenslet was the primary contributing factor to the image aberrations, we placed an adjustable iris in front of individual lenslets and reduced the aperture to a 3 mm diameter circle. This restricted imaging to the center of the lens where the master part is symmetric. The images generated by the full lenslet and reduced aperture lenslet are shown in Fig. 4.9, revealing improved image quality for the reduced aperture lenslet. In theory reducing the aperture for a spherical optic should improve image quality due to reduced spherical aberrations as well, however the modeled structures did not predict the observed level of aberration.

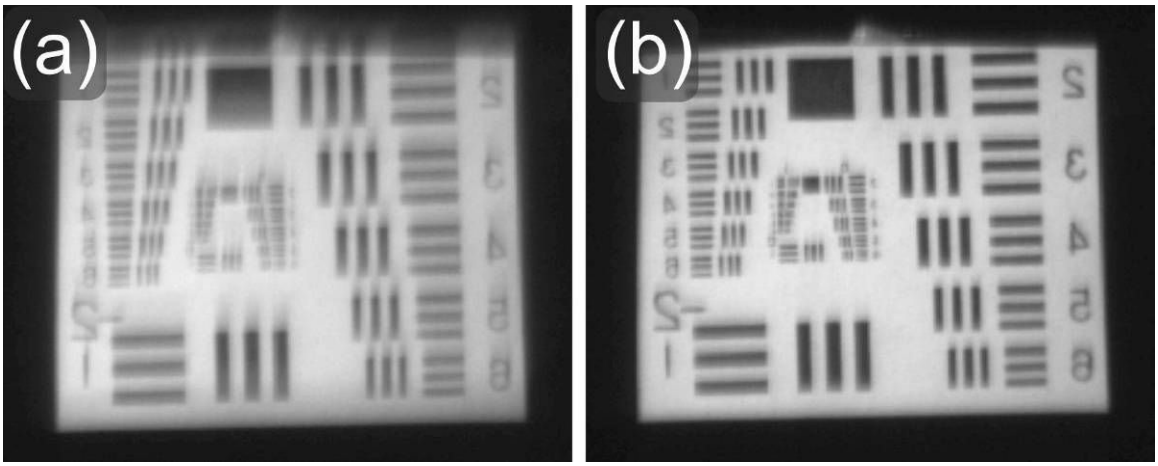

Fig. 4.9. (a) Image formed by single lenslet of air force target. Lenslet is positioned with long (4 mm) dimension vertically oriented. (b) Same image after aperture is reduced by an adjustable circular iris in front of lenslet array to 3 mm diameter.

While these tests were not exhaustive, we have shown that our micro-transfer molding process can be applied to generate compound lens structures. This structure was fabricated to demonstrate the ability to generate compound lenses with our micro-transfer molding process, and be testable using our optical setup. With these design restrictions, our device was not optimized for increased FOV. However, the success of our process suggests molding on more highly curved substrates to enable greater FOV is possible. Additionally, because these devices can be fabricated quickly and cheaply, they can serve as an excellent substrate for developing additional biomimetically inspired fabrication processes on complicated surface topography, where multiple iterations may be necessary. Imaging aberrations measured could likely be corrected by using thicker formulations of SU-8.

CHAPTER 5: LENS STRUCTURING FOR POLARIZATION SELECTIVITY

5.1 Overview

In our quest to fabricate optical functions present in biological systems, we have demonstrated curved spectral filtering elements and compound lenses. Another function present in biological systems commonly used in man made devices is polarization selectivity. In man made systems, polarization is often controlled with wire grid polarizers[102]. These devices have a straightforward design, typically consisting of subwavelength metal gratings, and are simple to implement on flat surfaces. Once again inspired by the mantis shrimp, we seek to generate polarization selective structures on a curved surface. In this chapter, we combine a wire grid polarizer with a commercially available convex lens to focus and linearly polarize near-IR light using a single hybrid element. The device is fabricated with a technique developed using interference lithography coupled with spray coated photoresist. We discuss polarizer design, fabrication techniques and challenges, and evaluate the extinction ratio for the resulting device.

5.2 Design of a Polarization selective lens

The intended function for our polarization selective lens was to focus incident light onto a CCD detector while linearly polarizing transmitted near-IR wavelengths, centered around 1550 nm. Our polarization selective lens has two functional components that combine to provide the functionality for the hybrid structure. The first is the lens itself

which must transmit in the near-IR, have sufficient focal length to focus the incident beam onto our detector, be sufficiently curved to demonstrate the process capability and have a SAG that is small enough to fit into our ICP etching chamber. The second component of our hybrid structure is a wire grid polarizer, introduced in Chapter 2. The polarizer must be subwavelength for 1550 nm, have sufficient extinction ratio to properly polarize transmitted light, have sufficient transmission of the TM polarization and must be compatible with our fabrication processes. To achieve these goals, CCD detector placement, lens material and ROC were taken into account for the lens, while metal type, thickness, grating period, and duty cycle were taken into account for the polarizer. First, a lens to serve as the substrate was chosen. The lens requirements were reasonably flexible, with several off the shelf parts available that would suit our purposes. The near-IR camera used, a Spiricon SP-1550M, has its detector recessed approximately 10 mm into it's housing. Assuming a few millimeters for positioning and alignment, the focal length of the lens should be 13 mm or more. We selected a 12.7 mm diameter BK7 glass lens with ROC of 7.7 mm, a focal length of 15 mm, and a SAG of 3.3 mm (Fig. 5.1). BK7 glass is a common lens material that has good transmission into the near-IR [112]. Next, aluminum was chosen as our metal for the polarizer, as it is known to work well as a wire grid polarizer [112], and is compatible with our deposition and etching equipment.

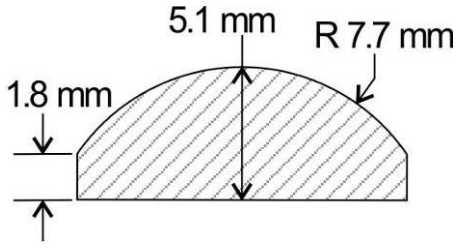

Fig. 5.1. Diagram of lens parameters for part patterned with aluminum gratings.

After establishing the material parameters of our polarizer, RCWA modeling using G-Solver was implemented to select dimensional parameters. Although polarizers modeled in G-Solver are limited to flat structures we did not have reason to expect significantly different behavior. Our device configuration with a planar incident wavefront would effectively result in varying angles of incidence on our polarizer. Unlike GMR filters, wire grid polarizers have a relatively robust response over a range of incident angles. To confirm this, the extinction ratio was modeled over a range of incidence angles (0-40°), and observed to have a relatively modest increase, as shown with parameters for modeled polarizer in Fig. 5.2. Thus, we could move forward with design parameters that play a greater role in device performance.

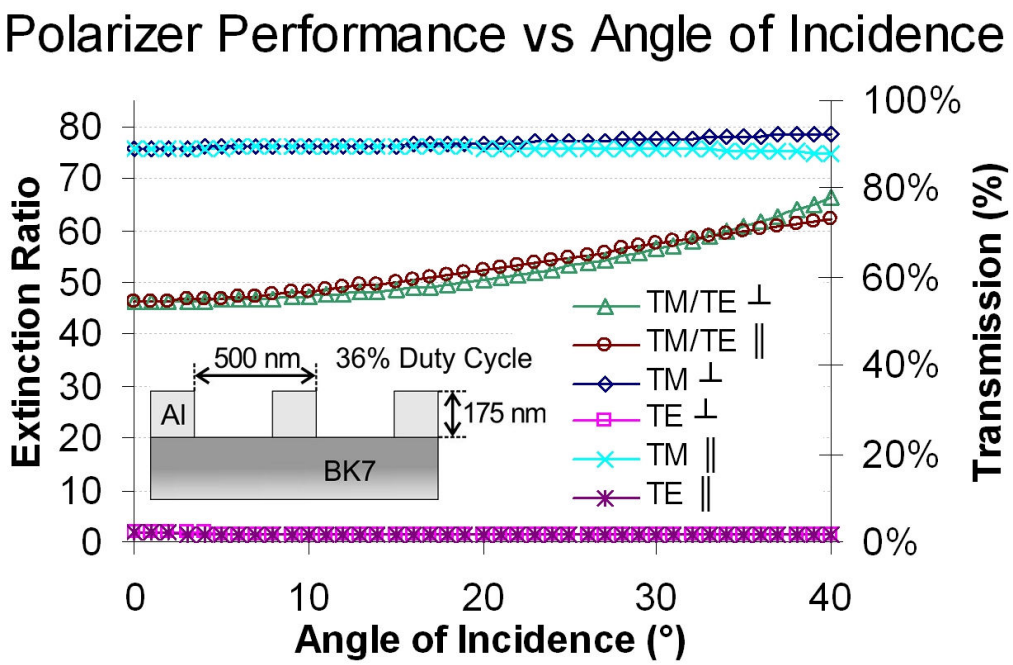

Fig. 5.2. Plot of polarizer TM and TE polarization transmission and the ratio of these values (extinction ratio) vs. the angle of incidence rotated perpendicular and parallel to the gratings with polarizer design shown inset. Increasing the angle of incidence modestly increases the extinction ratio.

As shown in Fig. 5.3 increasing the aluminum thickness has a significant impact on the extinction ratio of the polarizer. Over the parameter range we modeled, as the

thickness is increased, the extinction ratio becomes larger while having little impact on the transmission of the TM polarization. Using this model, an aluminum thickness of 175 nm was chosen in order to be thick enough to provide a functional extinction ratio, while being thin enough to ensure good etch uniformity using only exposed resist as our etch mask. If a higher aspect ratio polarizer is needed, incorporation of a hard mask for etching is often used [103].

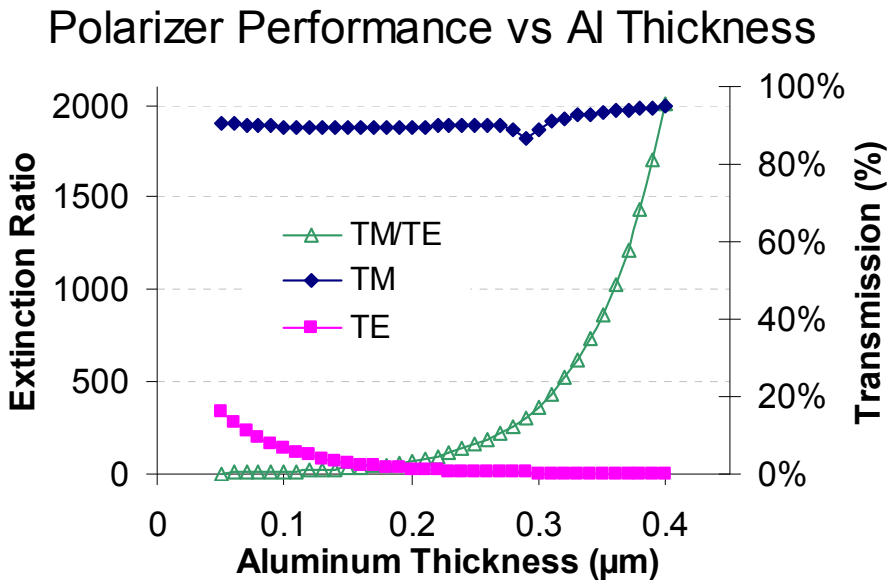

Fig. 5.3. Plot of polarizer TM and TE polarization transmission and the ratio of these values (extinction ratio) vs. the aluminum grating thickness (other grating parameters shown in Fig. 5.2). Increasing the aluminum thickness dramatically increases the extinction ratio by reducing the TE polarization transmission.

Although the period of a functional polarizer must be subwavelength to avoid diffraction of transmitted light, changes in period within the subwavelength regime do in fact alter the overall performance of the device. A range of periods possible with our interference lithography setup were modeled, showing an increase in extinction ratio for smaller period structures (Fig. 5.4).

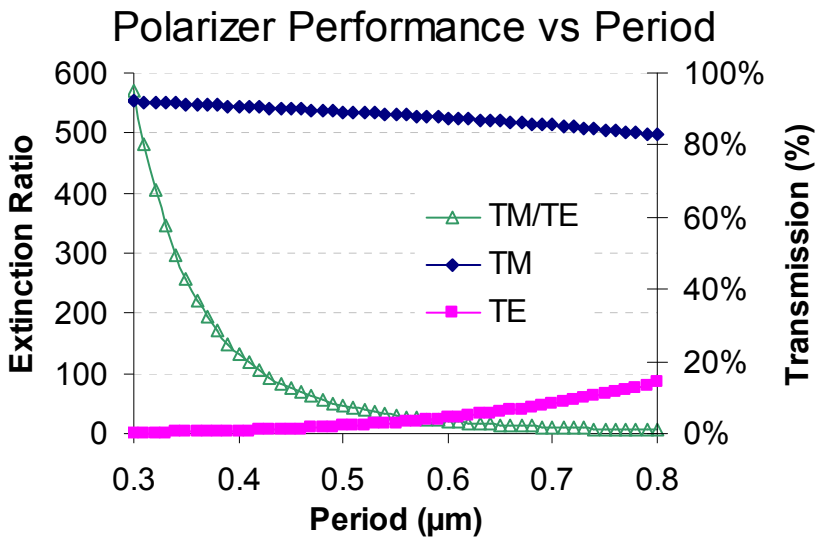

Fig. 5.4. Plot of polarizer TM and TE polarization transmission and the ratio of these values (extinction ratio) vs. the period of the aluminum grating (other grating parameters shown in Fig. 5.2). Reduced period increases the extinction ratio by increasing TM polarization and reducing TE polarization transmission.

With this in mind, a period of 500 nm was selected as it is the smallest period that can be measured on the CLSM and conventional light microscopes we have available to facilitate faster process development. Finally, the effects of duty cycle of the polarizer were modeled (Fig. 5.5).

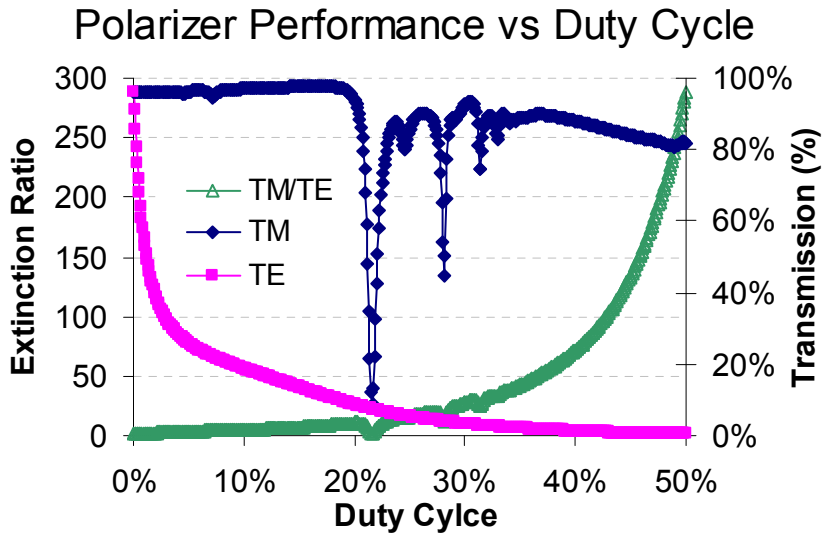

Fig. 5.5. Plot of polarizer TM and TE polarization transmission and the ratio of these values (extinction ratio) vs. the aluminum grating duty cycle (other grating parameters shown in Fig. 5.2). Although increasing the duty cycle generally increases the extinction ratio, after around 35% it does this at the cost of TM polarization transmission.

Duty cycle plays an important role in determining polarizer performance, but is the most challenging to adjust due to the nature of the interferometric exposure used to generate the gratings. To ensure good grating uniformity during exposure and development, specific exposure dose parameters were used. This resulted in limited duty cycle flexibility. Characterization of the interferometric exposure dose that provided uniform gratings over large areas suggested we should expect a duty cycle of around 36%. For the parameters chosen above, (175 nm thick aluminum, 500 nm period, 36% duty cycle, on a BK7 substrate) the modeled polarizer has an extinction ratio of 46 at 1550 nm, with similar performance over the C band (1530 nm to 1565 nm) as shown in Fig. 5.6.

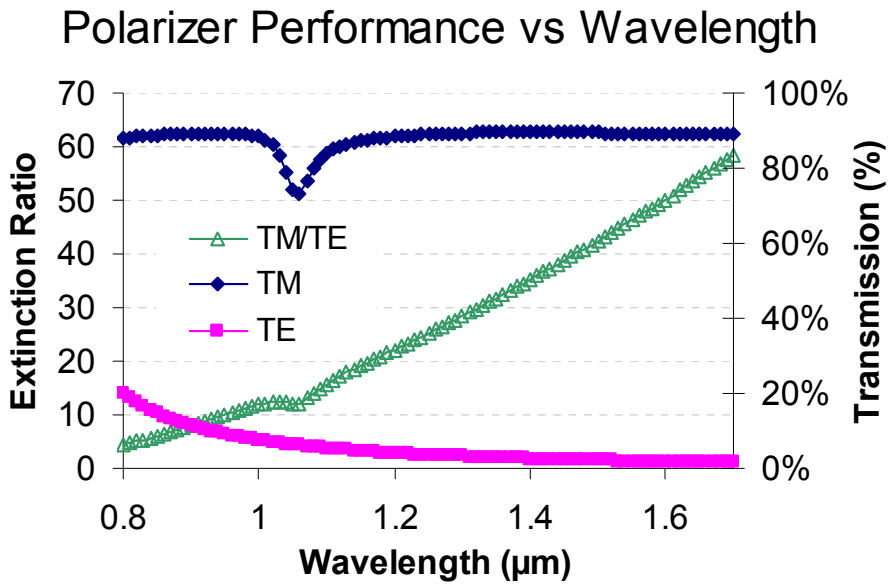

Fig. 5.6. Plot of polarizer TM and TE polarization transmission and the ratio of these values (extinction ratio) for the fabrication parameters chosen vs. wavelength (other grating parameters shown in Fig. 5.2). The extinction ratio at 1550 nm is 46.

5.3 Polarization selective lens fabrication

The two largest challenges for photolithographically patterning curved surfaces are exposure depth of field and resist coating uniformity. As discussed in Chapter 2,

interference lithography can address challenges related to exposure uniformity on curved surfaces due to its inherently large depth of field [46]. This is a significant advantage for this process, but without a uniform resist coating the ability to generate functional devices remains limited. To address the resist uniformity issues and fabricate a polarizer over a lens surface, we developed a process combining interference lithography with spray coated positive photoresist. Spray coated resist has the advantage that it can be applied to highly curved substrates in a uniform manner [113]. This technique has been used for thick resist layers [114] but to our knowledge has not been used to generate micro or nano-scale features.

For our process, we chose to generate the polarizer by ICP dry etching metal using photolithographically defined resist patterns as our etch mask. This involves first depositing metal layers over lens surfaces, then applying resist, exposing, developing and finally etching. For this process as described above, another issue becomes evident. For lithographic patterning on metal surfaces, the highly reflective properties of the substrate often reduce the quality of exposed structures. On a curved surface, this effect will be exacerbated by the locally variant surface profile. To address this issue on flat surfaces, an anti-reflection layer between the metal and resist layer is often required, typically called a back antireflection layer (BARC) [115]. Therefore, for our process, not only did we need to develop the capability to uniformly coat photoresist, but also the BARC layer.

To implement our process, an airbrush (Harbor Freight Tools) was connected to an in house pressurized nitrogen supply (Fig. 5.7) to ensure clean and consistent pressure during coating. The fluid cup was then filled with a solvent diluted material (photoresist or BARC) for coating and applied to the substrate. To facilitate uniform spray deposition,

the substrate was slowly spun (~200 RPM) on a spin coater. Several parameters have a significant impact on the uniformity and thickness of the resulting spray coating, including fluid viscosity, substrate distance, spray angle, duration, and nitrogen pressure. These were optimized through trial and error to achieve high quality spray coated films.

Fig. 5.7. Image of airbrush setup used to generate spray coatings.

The first parameter investigated was fluid viscosity. To generate thin spray coatings, we found that the fluid viscosity must be relatively low. Also, we found that sprayed resist thicknesses generally tended to be thicker than spun resist of the same viscosity. Depending on the coated material, different solvents can be used to reduce the viscosity of conventional photoresists and anti-reflection coatings to attain desired thickness. The photoresist used, Shipley 1813 (S1813) is a novolac based positive resist diluted with propylene glycol monomethyl ether acetate (PGMEA), intended for spin coating with a nominal thickness of 1.3 μm for a 4000 RPM spin. To reduce the spun or sprayed thickness, additional PGMEA can be added to dilute the resist. We found that spray coated S1813 formed reasonably uniform coatings over a range of dilutions (for coatings

in the hundreds of nanometers range). This was much unlike the coatings formed by spray coated SU-8, despite various dilutions with its solvent cyclopentanone. This appeared to be the result of differing evaporation rates for the two solvents. PGMEA is known to have a slower evaporation rate, facilitating coalescence of individual droplets as they accumulate on the substrate [113]. The anti-reflection coating used was Brewer Science XHRiC-16, with a nominal spin thickness of 150 nm at 4000 RPM. The solvent in XHRiC-16 is Propylene glycol monomethyl ether (PGME). PGME has a higher evaporation rate than PGMEA, and not surprisingly undiluted XHRiC-16 spray coatings suffered from poor uniformity. To address this issue, PGMEA was added to the XHRiC-16. Although not it's native solvent, the PGMEA was able to improve coating uniformity without any degradation to the anti-reflection properties of the BARC.

To characterize the spray coated thickness of various dilutions repeatable spray parameters were first chosen. We positioned the substrate approximately 3 inches from the airbrush nozzle, with the spray angle at approximately 35°. The spray duration was chosen to be approximately 1 second, with a spray pressure of 25 psi. These parameters were adjusted as needed to account for different substrate and coating criteria. With a nominal spray process in place, various coating dilutions were then characterized by measurement with a Tencor Alpha Step 200 profilometer. A resist thickness of 160 nm was chosen to provide enough resist material to endure the duration of the aluminum etching, while being thin enough to achieve good quality patterning of the photoresist with our interferometric exposure and subsequent development. To achieve the desired resist thickness of 160 nm, 1 part S1813 was diluted with 7.5 parts PGMEA. A BARC thickness of 60 nm was chosen to provide sufficient anti-reflection properties while being

thin enough to limit the duration of a descum step. To achieve the desired BARC thickness of 60 nm, 1 part XHRiC-16 was diluted with 4 parts PGMEA.

Following spray coating characterization and selection of resist and BARC parameters, we needed to verify the anti-reflective properties of the BARC would still function on our curved substrate. Anti-reflection coatings used in lithography operate primarily through absorption of the exposure wavelength [116]. A curved substrate will effectively have varying angles of incidence for a planar exposure wavefront (Fig. 5.8), impacting Fresnel reflections off the coating, as well as the optical path length through the absorbing BARC. To test whether this could have a significant impact on fabrication, the BARC alone, and the BARC and resist coating were spray coated onto flat aluminum coated BK7 glass microscope slides. To simulate the various angles of incidence caused by the lens surface, the reflection of TM and TE polarization was measured with a JA Woolem VASE ellipsometer as the parts were rotated over a range of incident angles. For both the BARC alone and the BARC and resist, changes in reflectivity are relatively gradual. Because the reflected wavefront intensity is relatively small compared with the un-attenuated incident wavefront, the amount of change observed suggested the impact on the overall exposure uniformity was relatively minor.

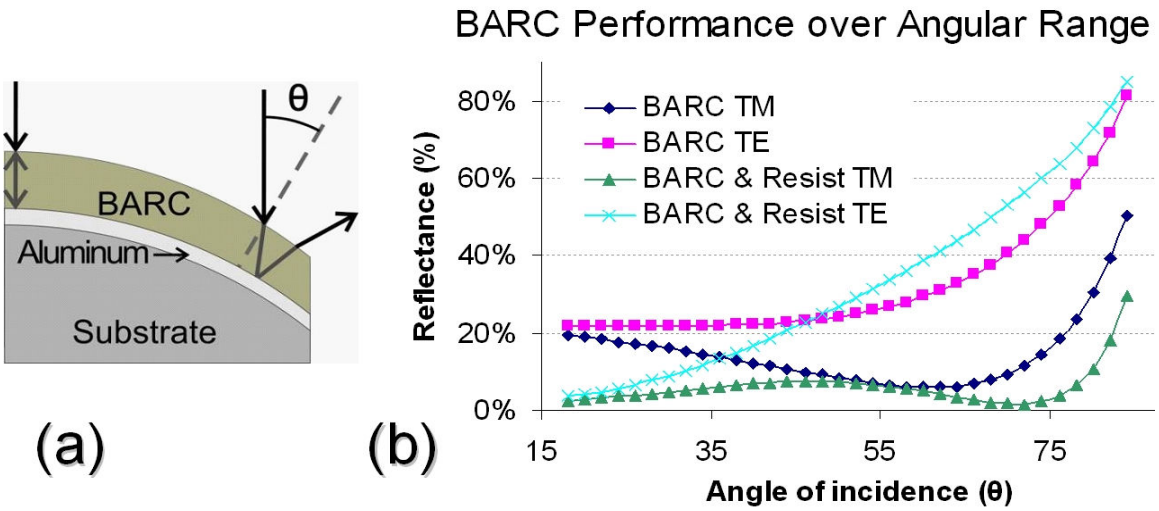

Fig. 5.8. (a) Curved substrates effectively have spatially dependent angles of incidence for a planar exposure wavefront. This impacts Fresnel reflections and optical path length through the absorbing BARC layer. (b) Reflection from an aluminum coated glass slide spray coated with a BARC alone, and with a BARC and resist coating was measured over a range of angles for TE and TM polarization. For reference, uncoated aluminum slides have a reflection of around 92% for TM and 96% for TE at a 20° angle of incidence.

After demonstrating that resist and BARC layers had the potential to work on curved surfaces, we configured specifics of the fabrication process (Fig. 5.9).

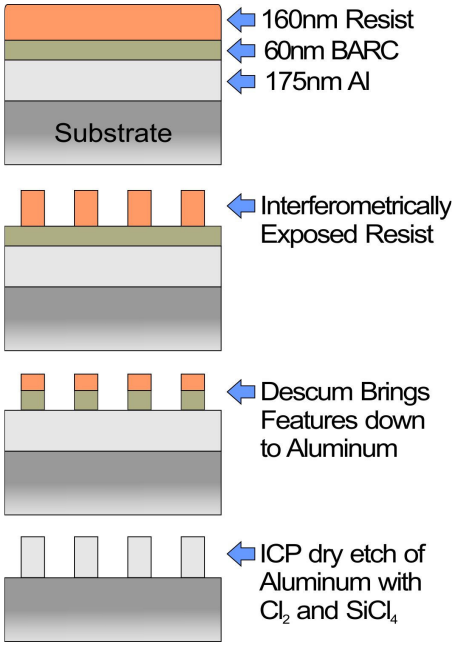

Fig. 5.9. Process diagram for patterning aluminum gratings. Aluminum is evaporated onto substrate, followed by spray coating of BARC and photoresist. The resist is exposed interferometrically, and chemically developed. A descum process etches the BARC layer and photoresist layer, bringing features down to the substrate. An ICP Cl_2 and $SiCl_4$ etch process etches the aluminum.

BK7 microscope slides and lenses were prepared for deposition of aluminum coatings by cleaning in 3 parts sulfuric acid to 2 parts hydrogen peroxide (piranha etch) for half an hour, followed by rinsing in DI water. Substrates were then placed into a Lesker PVD-75 e-beam evaporation system and pumped down to 9 x 10^{-7} Torr. Aluminum was then evaporated at a rate of 20 A/s until the desired thickness of 175 nm was reached. The aluminum coated substrates were removed from the chamber and spray coated with XHRiC-16. A soft bake was then performed on a hot plate at 185° C for 1 minute. The substrate was spray coated with S1813 and soft baked on a hot plate at 115° C for 1 minute. Next, using a Lloyd's mirror configuration introduced in Chapter 2, resist patterns were exposed into the photoresist using a Coherent Innova 300 FRED Ion Argon laser set for near I-line exposure at 363.8 nm. The mirror setup (Fig. 5.10) consists of a 2 inch square aluminum mirror placed approximately 1 meter from a spatial filter. An optimized dose of 15.5 mJ was used to expose the resist, followed by a PEB of 1 min at 115° C on a hot plate.

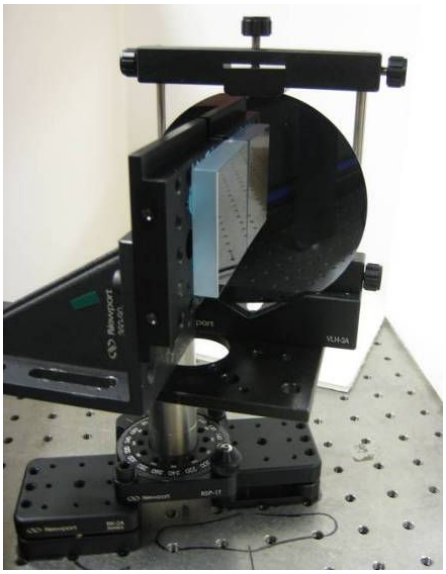

Fig. 5.10. Picture of interference lithography exposure setup. Mirror and substrate (in this case a silicon wafer) are placed at a 90° angle to one another and placed on a rotating stage to allow simple adjustment of grating period.

After PEB, the resist was submerged in Shipley MF-319 developer for approximately 20 seconds. The substrates with patterned photoresist were placed in a STS III-V ICP etch system for aluminum etching. To remove the BARC layer and expose the underlying aluminum for etching, a descum process is used first. The descum process consisted of an 8 second oxygen and helium plasma etch at 10 mTorr main pressure, 45 sccm O_2, 50 sccm He, coil (ICP) power of 500 W, and platen power of 50 W. After the descum, a 15 second aluminum etch at 10 mTorr main pressure, 15 sccm Cl_2, 23 sccm $SiCl_4$, coil power of 1000 W, and a platen power of 75 W was used. After etching the aluminum, the descum process was run again for 2 minutes to remove any remaining photoresist or BARC. This process was run on silicon wafers as well for cleaving and cross sectional inspection. SEM images of cleaved gratings in Fig. 5.11 show good uniformity and successful etching of the aluminum.

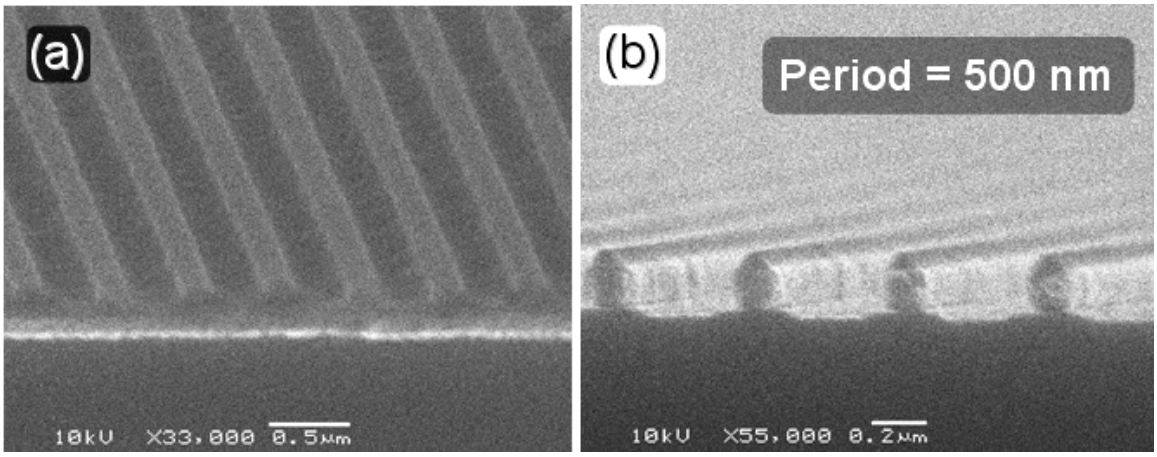

Fig. 5.11. Cross section of structures on Si substrate patterned using interference lithography. (a) SEM image of photoresist patterns over BARC and aluminum layers. (b) SEM image of aluminum gratings after descum and etch. Remaining photoresist can be seen at tops of structures.

After establishing our fabrication parameters generated uniform structures on flat surfaces, the process was run on the selected lens. Visual inspection of the fabricated

element shows good color uniformity and light transmission (Fig. 5.12). The center patterned area of the lens is a 6.1 mm diameter circle. The SAG over the patterned area is 630 μm, covering a 43° arc of a circle. SEM images taken at the center and edges of the structure confirm successful etching of the aluminum layer.

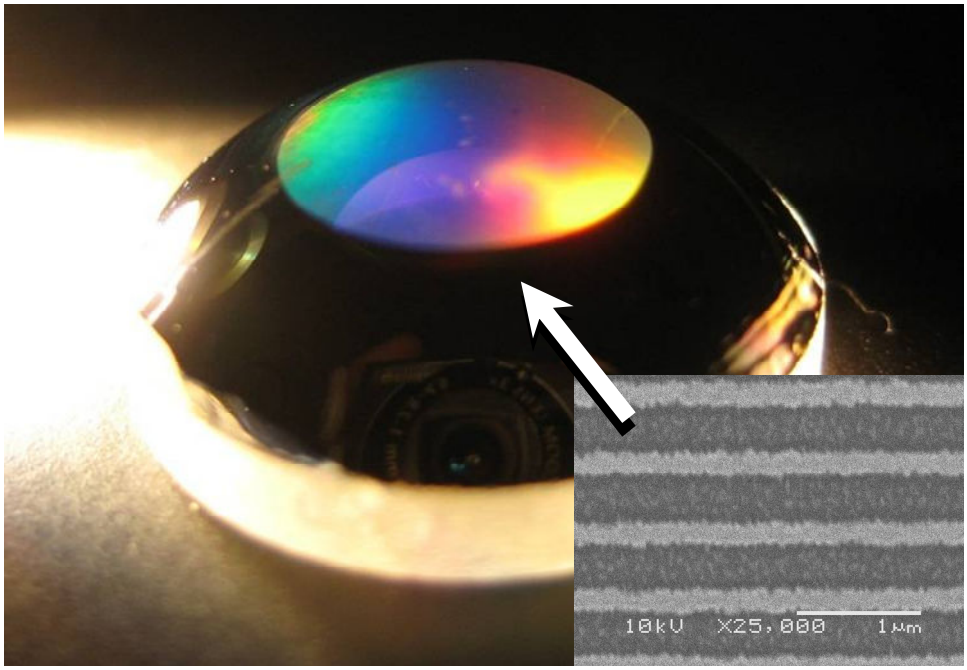

Fig. 5.12. Fabricated polarization selective lens. Color observed is from light bouncing off the table and then being transmitted through the aluminum grating structure. The patterned area is 6.1 mm in diameter with 630 μm SAG. SEM image of gratings at top of structure is shown inset, showing successful etching of aluminum gratings.

5.4 Polarization selective lens performance

To measure the performance of the polarizing lens, a test setup as shown in Fig. 5.13 and Fig. 5.14 was arranged. Unpolarized light emitted by a high power broadband source (AFC Technologies BBS 15/16D -TS Ultra broad high power fiber source) was coupled to an optical fiber, whose terminus was placed 1.75 m from our measurement setup. An Edmund Optics linear IR polarizer (EO 47327) was placed into the beam path. Following the polarizer, an adjustable iris was used to aperture the beam down to the width of the

patterned area on the part. Next our patterned lens was placed into the beam path, and positioned to focus incident light onto the SP-1550M CCD detector.

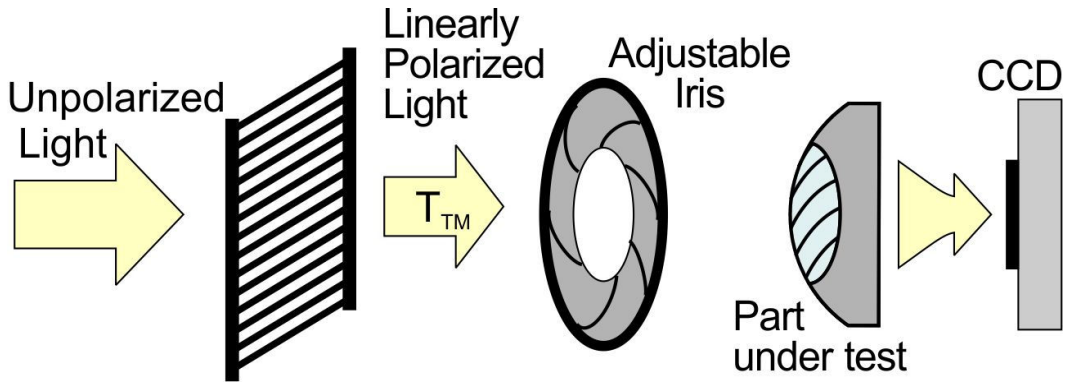

Fig. 5.13. Diagram of polarization selective lens measurement setup. Light is linearly polarized by a rotatable commercial IR polarizer, and then passes through an aperture set to match the patterned area of the part. Next, light is incident on the part with any transmitted light focused onto a near-IR CCD detector.

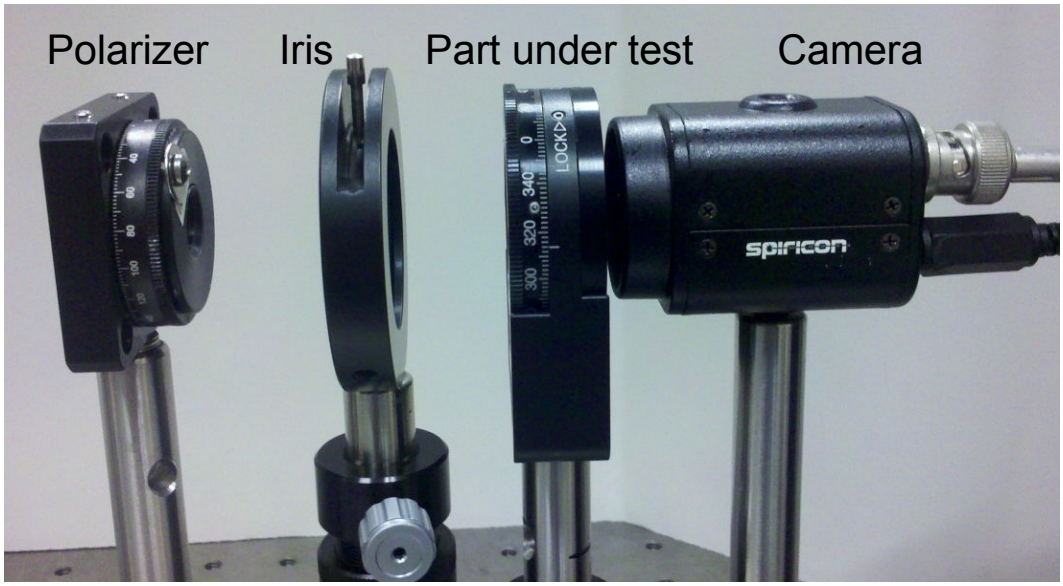

Fig. 5.14. Picture of polarization selective lens measurement setup.

The linear polarizer was then rotated with respect to the part which serves as the analyzer in this arrangement. Integrated intensity values on the CCD detector given by the LBA-PC laser beam profiling software for the SP-1550M were then recorded at each angle (Fig. 5.15). The patterned lens was then replaced by an identical but unpatterned lens and measurements were repeated. Using the intensity values for the unpatterned part

as a baseline to remove system losses, percent transmission values for the polarizing lens were calculated (Fig. 5.16).

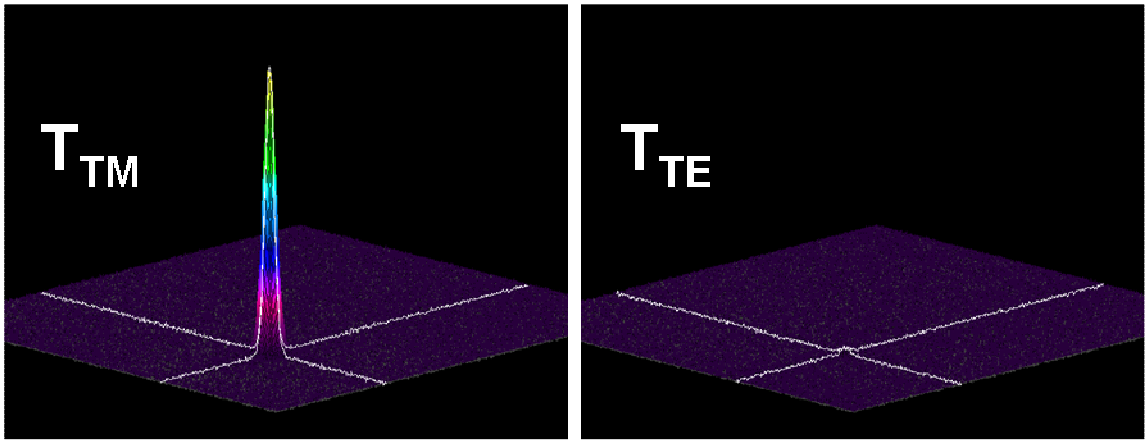

Fig. 5.15. Focused beam profile of transmitted TE and TM polarizations.

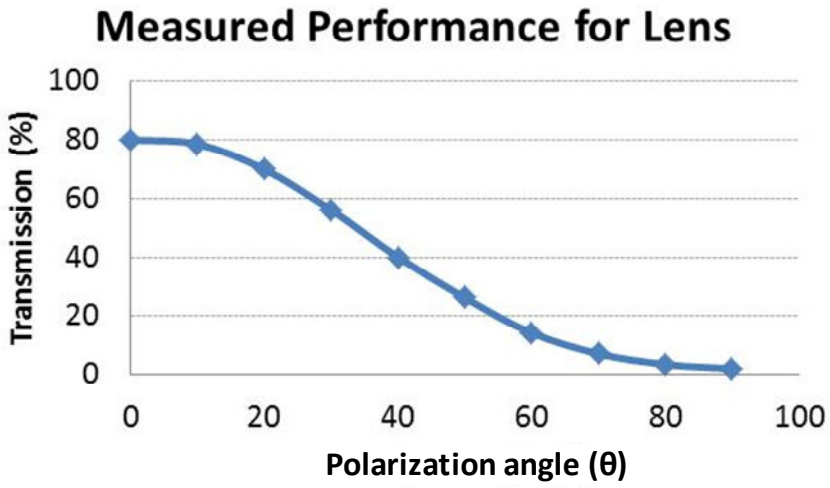

Fig. 5.16. Measurements of transmitted light through polarization selective lens over a range of polarization angles.

The resulting maximum transmission for our part was 80.3% with an extinction ratio of 40.4, showing good agreement with modeled values. Measured intensity is a summation of transmitted light from all locations on the part, including angles of incidence other than zero. Modeled values would suggest a slight increase in extinction ratio for light incident at greater angles as shown in Fig. 5.2. For our maximum angle of

incidence of 21.5°, we should observe an increase in extinction ratio to 51 for perpendicular rotation and 53 for parallel. However this effect is countered by a calculated increase in period caused by the fabrication process. The calculated period at the edge of the structure perpendicular to the grating should be 537 nm with an associated extinction ratio of 34. These two relatively modest and opposing effects did not appear to make a significant impact on the overall performance of our device.

In summary, we have demonstrated the combination of interference lithography's large depth of field with the conformal nature of spray coated photoresist can be used to generate functional polarization-selective lenses. Measured values matched well with modeled values, suggesting the surface curvature has limited effect on the performance of the polarizer itself. In addition, this suggests alternative designs with increased extinction ratio could be fabricated using similar techniques.

CHAPTER 6: CONCLUSIONS

6.1 Summary and implications

Technological trends to provide more powerful devices in smaller spaces have driven and continue to drive a large portion of work done by the research community. Optical components are becoming more relevant in many devices, as the functions they can perform continue to expand. This is in part due to micro and nano-scale optics. These structures have been demonstrated as critical elements in a wide variety of applications for consumer, medical, industrial, commercial and military purposes. As fabrication capabilities to produce structures on the scale of the wavelength of light have improved, the novel designs and functions related to these structures have only increased. However many obstacles still exist to consolidate the numerous optical functions desired into small and lightweight packages. Vision systems found in small animals present us with an excellent source of inspiration to realize the next generation of optical components, with a common theme being a high level of functional integration.

Examples of inspirational biological designs with hierarchical themes include a fly's eye, moth's eye and mantis shrimp's eye. The fly eye, consisting of a simple compound lens, enables a wide field of view in a compact and lightweight package. Another biological example is a moth's eye, consisting of a compound lens with nanometer scale grating features called nipple arrays covering each lenslet. The moth's compound lens functions similar to the fly's eye, but what is more noteworthy is the anti-reflective

properties of the nanostructures. Perhaps the best example is the mantis shrimp eye, one of the most sophisticated vision systems found in nature. The mantis shrimp has a compound eye arrangement, with portions of the eye being dedicated to specific optical functions such as spectral filtering and polarization selectivity. With so many advanced systems found in nature, where evolution has repeatedly selected an optimized design, the question is then: How can we make these structures?

Despite the inspiration, creating optical structures on curved components is a significant challenge for existing modeling, fabrication and testing methods. Infrastructure from the semiconductor industry has been used to generate a great deal of micro-optic devices, but the majority of this technology and related processes is designed for generating structures on flat surfaces, requiring alternative approaches for hierarchical systems. In this dissertation, the primary focus has been on overcoming the fabrication challenges, while using conventional and improvised design and testing techniques to understand and measure the performance of fabricated devices.

A micro-transfer molding process leveraging the flexible nature of molds used in soft lithography was developed to transfer SU-8 structures onto lens surfaces to generate curved spectral filters and compound lenses. The nature of SU-8, an inherently rugged and optically transparent polymer with high thermal and chemical resistance enables molded structures to remain part of a functional device. To create spectral filters, two dimensional gratings were molded on the surface of a concave lens and then coated with dielectric layers to form a GMR. A custom measurement setup was created to measure reflection off the GMR, by placing a fiber terminus at the center of curvature of the concave lens in a retro-reflection configuration. The devices showed similar performance

to devices fabricated on flat surfaces with shifts in resonant wavelength primarily resulting from the nature of the flexible molding process.

Compound lenses were fabricated by combining an array of convex lenslets with a macro-scale convex lens using the SU-8 conformal molding techniques. Care had to be taken designing the device to ensure it could be tested over visible wavelengths with the measurement tools available. The molding process itself has a significant impact on the dimensions and optical performance of the fabricated structure due to the substrate curvature contributing to the SAG of the molded lenslet. Compound lenses thus demonstrated could serve as substrates for generating more complicated biomimetic structures in the future.

A new process was developed using the depth of field of interference lithography to expose photoresist spray coated over lens structures. This process was combined with ICP dry etching to transfer lithographically patterned structures into underlying materials to generate polarization selective lenses. Measurements of the extinction ratio of the polarization selective lens suggested the device performed similar to values predicted by modeling the structure on a flat.

The techniques and approaches presented in this dissertation demonstrate that many of the hierarchical optical structures once restricted to the natural world can in fact be realized, thus enabling more powerful, more compact, and lighter weight devices for the future. Optical technologies centered around micro and nano-optics have borrowed heavily from the wafer based infrastructure built by the semiconductor industry. However, as more complex and more functional hierarchical devices are realized, a greater level of infrastructure will likely follow.

6.2 Future work

Future research based on work in this dissertation can focus both on novel designs enabled by new fabrication processes, as well as on improving the design, fabrication and testing techniques.

Because this work makes significant progress in developing processes for generating biomimetically inspired hierarchical devices, it opens the door to creation of an array of new structures. The micro-transfer molding process could be used to transfer grating patterns onto curved surfaces that serve as phase mask elements for subsequent exposure and development. Using a material like SU-8 combined with super critical drying after development, this process could create photonic crystal structures on contoured surfaces. Flat lenslet arrays could be patterned with micro or nano-scale structures to serve as a replication master. Then, the micro-transfer molding process could generate a compound lens structure with additional features already "built in". This type of process could mold a compound lens with anti-reflective moth eye structures. The spray coated resist and interference lithography process could be altered to mask off portions of the exposure wavefront to spatially vary the orientation or period of the gratings. This process could then be used to fabricate, for example, a polarimeter or spectrally selective elements on the lenslets of a compound lens as shown in Fig. 6.1.

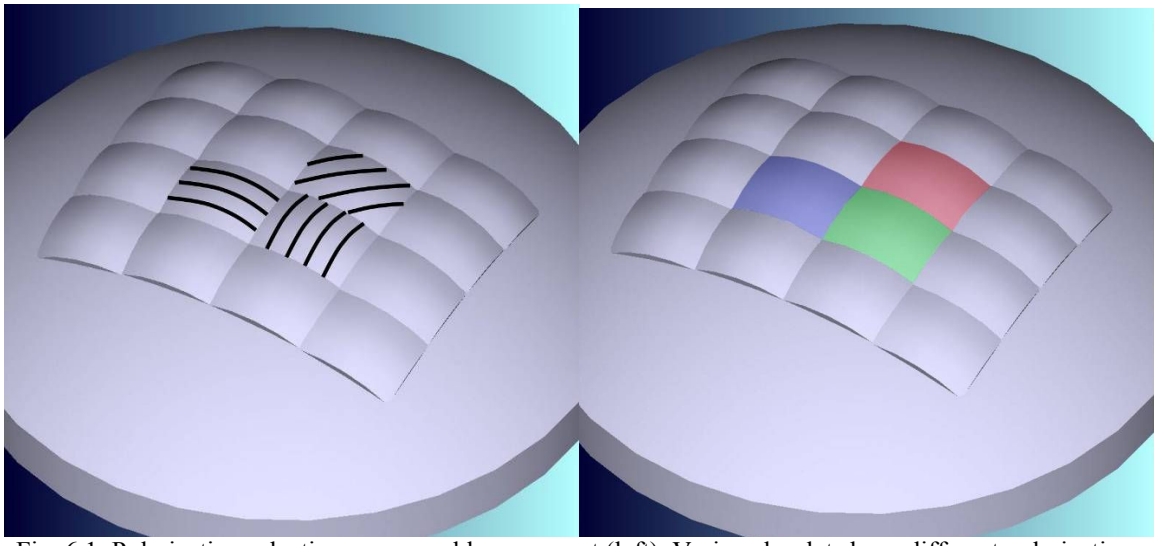

Fig. 6.1. Polarization selective compound lens concept (left). Various lenslets have different polarization-selective structures. Spectrally selective compound lens concept (right). Various lenslets have different spectral filters.

Alternatively, future work could focus on improving or modifying the fabrication processes themselves. How the micro-transfer molding process changes feature dimensions over different substrates and conditions could be studied in greater detail. This information could then be used to correct for predicted variation in replicated patterns by altering master feature dimensions. Hybrid structures consisting of gratings molded onto curved surfaces for GMR devices have been demonstrated. Taking the replication process a step further, the composite element could serve as a master for generating replicated structures. This could greatly improve throughput of the process. Additional SU-8 thicknesses could be implemented to ensure lenslet pattern fidelity is maintained. This could improve imaging quality of the compound lens arrays fabricated using this process. Further adjustments could be made to the resist spray coating technique to attain good resist uniformity over an array of different substrates. Incorporation of a hard mask into the polarizer fabrication process could enable thicker

metal layers and improve extinction ratio. Metal layers created by this process could also serve as a hard mask in etching of other substrate materials.

REFERENCES

[1] R. Völkel, M. Eisner, and K. J. Weible, "Miniaturized imaging systems," Microelectronic Engineering, 67, 461-472 (2003).

[2] L. P. Lee and R. Szema, "Inspirations from biological optics for advanced photonic systems," Science, 310(5751), 1148 (2005).

[3] J. G. Kim, N. Takama, B. J. Kim, and H. Fujita, "Optical-soft lithographic technology for patterning on curved surfaces," Journal of Micromechanics and Microengineering, 19, 055017 (2009).

[4] D. Radtke and U. D. Zeitner, "Laser-lithography on non-planar surfaces," Optics Express, 15(3), 1167-1174 (2007).

[5] Y. Xia and G. M. Whitesides, "Soft lithography," Annual review of materials science, 28(1), 153-184 (1998).

[6] L. Li and A. Y. Yi, "Microfabrication on a curved surface using 3D microlens array projection," Journal of Micromechanics and Microengineering, 19, 105010 (2009).

[7] T. J. Suleski and R. D. Te Kolste, "Fabrication Trends for Free-Space Microoptics," J. Lightwave Technol., 23(2), 633 (2005).

[8] D. Wawro, Y. Ding, S. Gimlin, S. Zimmerman, C. Kearney, K. Pawlowski, and R. Magnusson, "Guided-mode resonance sensors for rapid medical diagnostic testing applications," Proc. SPIE 7173, 717303 (2009).

[9] E. Bonetto, L. Chiaraviglio, D. Cuda, G. Castillo, and F. Neri, "Optical technologies can improve the energy efficiency of networks," Proc. IEEE, Eur. Conf. Exhib. Opt. Commun., Paper 5.5.1 (2009).

[10] V. Emiliani, D. Cojoc, E. Ferrari, V. Garbin, C. Durieux, M. Coppey-Moisan, and E. Di Fabrizio, "Wave front engineering for microscopy of living cells," Optics Express, 13(5), 1395-1405 (2005).

[11] D. R. Smith, J. B. Pendry, and M. C. K. Wiltshire, "Metamaterials and negative refractive index," Science, 305(5685), 788 (2004).

[12] E. B. Grann, M. G. Moharam, and D. A. Pommet, "Artificial uniaxial and biaxial dielectrics with use of two-dimensional subwavelength binary gratings," JOSA A, 11(10), 2695-2703 (1994).

[13] M. He, X. C. Yuan, N. Q. Ngo, J. Bu, and S. H. Tao, "Single-step fabrication of a microlens array in sol-gel material by direct laser writing and its application in optical coupling," Journal of Optics A: Pure and Applied Optics, 6(1), 94-97 (2004).

[14] J.-N. Kuo, C.-C. Hsieh, S.-Y. Yang, and G.-B. Lee, "An SU-8 microlens array fabricated by soft replica molding for cell counting applications," Journal of Micromechanics and Microengineering, 17(4), 693-699 (2007).

[15] J. Tanida, T. Kumagai, K. Yamada, S. Miyatake, K. Ishida, T. Morimoto, N. Kondou, D. Miyazaki, and Y. Ichioka, "Thin observation module by bound optics (TOMBO): concept and experimental verification," Applied Optics, 40(11), 1806-1813 (2001).

[16] M. Shankar, R. Willett, N. P. Pitsianis, R. Te Kolste, C. Chen, R. Gibbons, and D. J. Brady, "Ultra-thin multiple-channel LWIR imaging systems," Proc. Citeseer 6294, 629411 (2006).

[17] W. B. Spillman Jr, M. Mayer, J. Bennett, J. Gong, K. E. Meissner, B. Davis, R. O. Claus, A. A. Muelenaer Jr, and X. Xu, "A 'smart' bed for non-intrusive monitoring of patient physiological factors," Measurement Science and Technology, 15, 1614 (2004).

[18] J. H. Karp, E. J. Tremblay, and J. E. Ford, "Planar micro-optic solar concentrator," Opt. Express, 18(2), 1122–1133.

[19] T. Ergin, N. Stenger, P. Brenner, J. B. Pendry, and M. Wegener, "Three-dimensional invisibility cloak at optical wavelengths," Science, 328(5976), 337.

[20] X. Zhang, M. A. Young, O. Lyandres, and R. P. Van Duyne, "Rapid detection of an anthrax biomarker by surface-enhanced Raman spectroscopy," Journal of the American Chemical Society, 127(12), 4484-4489 (2005).

[21] H. Cho, P. Kapur, and K. C. Saraswat, "Power comparison between high-speed electrical and optical interconnects for interchip communication," Journal of Lightwave Technology, 22(9), 2021 (2004).

[22] N. Franceschini, J. M. Pichon, C. Blanes, and J. M. Brady, "From insect vision to robot vision," Philosophical Transactions of the Royal Society of London. Series B: Biological Sciences, 337(1281), 283 (1992).

[23] J. W. Duparré and F. C. Wippermann, "Micro-optical artificial compound eyes," Bioinspiration & biomimetics, 1, R1 (2006).

[24] D. E. Nilsson and A. Kelber, "A functional analysis of compound eye evolution," Arthropod structure & development, 36(4), 373-385 (2007).

[25] M. F. Land and R. D. Fernald, "The evolution of eyes," Annual review of neuroscience, 15(1), 1-29 (1992).

[26] S. Rossel, "Binocular spatial localization in the praying mantis," Journal of experimental biology, 120(1), 265 (1986).

[27] D. G. Stavenga, "Partial coherence and other optical delicacies of lepidopteran superposition eyes," Journal of experimental biology, 209(10), 1904 (2006).

[28] D. G. Stavenga, S. Foletti, G. Palasantzas, and K. Arikawa, "Light on the moth-eye corneal nipple array of butterflies," Proceedings of the Royal Society B: Biological Sciences, 273(1587), 661 (2006).

[29] S. Kleinlogel and A. G. White, "The Secret World of Shrimps: Polarisation Vision at Its Best," PLoS ONE, 3(5), (2008).

[30] J. Marshall and J. Oberwinkler, "Ultraviolet vision: The colourful world of the mantis shrimp," Nature, 401(6756), 873-874 (1999).

[31] J. Marshall, T. W. Cronin, and S. Kleinlogel, "Stomatopod eye structure and function: a review," Arthropod structure & development, 36(4), 420-448 (2007).

[32] E. Hecht, [Optics 4th edition], San Francisco, Addison Wesley, 2001.

[33] R. C. Rumpf, "Design and optimization of nano-optical elements by coupling fabrication to optical behavior," Ph.D. Dissertation, University of Central Florida, Orlando, (2006).

[34] R. C. Rumpf and E. G. Johnson, "Modeling fabrication to accurately place GMR resonances," Optics Express, 15(6), 3452-3464 (2007).

[35] M. G. Moharam, D. A. Pommet, E. B. Grann, and T. K. Gaylord, "Stable implementation of the rigorous coupled-wave analysis for surface-relief gratings: enhanced transmittance matrix approach," Journal of the Optical Society of America A, 12(5), 1077-1086 (1995).

[36] A. Taflove and S. C. Hagness, [Computational electrodynamics: the finite-difference time-domain method], Norwood, Artech House, 2000.

[37] R. A. Jones, "Optimization of computer controlled polishing," Applied Optics, 16(1), 218-224 (1977).

[38] D. Malacara and B. J. Thompson, [Handbook of optical engineering], CRC, 2001.

[39] R. Guo, S. Xiao, X. Zhai, J. Li, A. Xia, and W. Huang, "Micro lens fabrication by means of femtosecond two photon photopolymerization," Optics Express, 14(2), 810-816 (2006).

[40] P. Heremans, J. Genoe, M. Kuijk, R. Vounckx, and G. Borghs, "Mushroom microlenses: Optimized microlenses by reflow of multiple layers of photoresist," IEEE Photonics Technology Letters, 9(10), 1367-1369 (1997).

[41] J. Yao, Z. Cui, F. Gao, Y. Zhang, Y. Guo, C. Du, H. Zeng, and C. Qiu, "Refractive micro lens array made of dichromate gelatin with gray-tone photolithography," Microelectronic Engineering, 14, 810-816 (2001).

[42] J. Sung, H. Hockel, and E. G. Johnson, "Analog micro-optics fabrication by use of a two-dimensional binary phase-grating mask," Opt. Lett., 30(2), 150-152 (2005).

[43] W. Hong and A. Yariv, "Holographic interference lithography for integrated optics," IEEE Transactions on Electron Devices, 25(10), 1193-1200 (1978).

[44] A. L. Bogdanov, "Use of SU-8 negative photoresist for optical mask manufacturing," Proc. Society of Photo-Optical Instrumentation Engineers, Bellingham, WA, USA 3999 (II), 1215-1225 (2000).

[45] W. M. Choi and O. O. Park, "The fabrication of submicron patterns on curved substrates using a polydimethylsiloxane film mould," Nanotechnology, 15, 1767 (2004).

[46] S. Traut and H. P. Herzig, "Holographically recorded gratings on microlenses for a miniaturized spectrometer array," Optical Engineering, 39(1), 290-298 (2000).

[47] A. Disch, J. Mick, B. Blasi, and C. Muller, "Nanostructures on microstructured surfaces," Microsystem Technologies, 13(5-6), 483-486 (2007).

[48] M. A. Davies, C. J. Evans, S. R. Patterson, R. Vohra, and B. C. Bergner, "Application of precision diamond machining to the manufacture of micro-photonics components," Lithographic and Micromachining Techniques for Optical Component Fabrication II, Proc. SPIE 5183, 94-108 (2003).

[49] Y. Fu and K. A. B. Ngoi, "Focused ion beam direct fabrication of micro-optical elements: features compared with laser beam and electron beam direct writing," Innovation in Manufacturing Systems and Technology, 3904, (2004).

[50] M. A. Davies, T. J. Suleski, B. S. Dutterer, A. Georgi, J. Owen, and A. T. Cannistra, "Can Multi-Scale Optics be Fabricated by Ultraprecision Systems - Hierarchical Fabrication Across Seven Orders of Magnitude?," NSF CMMI Grantee Conference, Atlanta, Georgia, Proc. NSF, 0927621 (2011).

[51] J. F. Galisteo López, M. Ibisate, R. Sapienza, L. S. Froufe Pérez, Á. Blanco, and C. López, "Self Assembled Photonic Structures," Advanced Materials, 23(1), 30–69 (2011).

[52] G. M. Whitesides and B. Grzybowski, "Self-assembly at all scales," Science, 295(5564), 2418 (2002).

[53] H. Ge, Y. Song, L. Jiang, and D. Zhu, "One-step preparation of polystyrene colloidal crystal films with structural colors and high hydrophobicity," Thin Solid Films, 515(4), 1539-1543 (2006).

[54] E. K. Riley and C. M. Liddell, "Confinement-Controlled Self Assembly of Colloids with Simultaneous Isotropic and Anisotropic Cross-Section," Langmuir, 26(14), 11648–11656 (2010).

[55] F. Sun, W. Cai, Y. Li, L. Jia, and F. Lu, "Direct Growth of Mono and Multilayer Nanostructured Porous Films on Curved Surfaces and Their Application as Gas Sensors," Advanced Materials, 17(23), 2872-2877 (2005).

[56] Y. Liu, X. Hu, D. Zhang, B. Cheng, and Q. Meng, "Subpicosecond optical switching in polystyrene opal," Applied Physics Letters, 86, 151102 (2005).

[57] H. K. Choi, M. H. Kim, S. H. Im, and O. O. Park, "Fabrication of Ordered Nanostructured Arrays Using Poly (dimethylsiloxane) Replica Molds Based on Three Dimensional Colloidal Crystals," Advanced Functional Materials, 19(10), 1594-1600 (2009).

[58] R. G. Shimmin, A. J. DiMauro, and P. V. Braun, "Slow vertical deposition of colloidal crystals: A langmuir-blodgett process?," Langmuir, 22(15), 6507-6513 (2006).

[59] S. H. Im, M. H. Kim, and O. O. Park, "Thickness control of colloidal crystals with a substrate dipped at a tilted angle into a colloidal suspension," Chemistry of materials, 15(9), 1797-1802 (2003).

[60] H. Schift, C. David, M. Gabriel, J. Gobrecht, L. J. Heyderman, W. Kaiser, S. Koppel, and L. Scandella, "Nanoreplication in polymers using hot embossing and injection molding," Microelectronic Engineering, 53(1), 171-174 (2000).

[61] F. Hua, Y. Sun, A. Gaur, M. A. Meitl, L. Bilhaut, L. Rotkina, J. Wang, P. Geil, M. Shim, and J. A. Rogers, "Polymer imprint lithography with molecular-scale resolution," Nano letters, 4(12), 2467-2471 (2004).

[62] B. D. Gates, Q. Xu, M. Stewart, D. Ryan, C. G. Willson, and G. M. Whitesides, "New approaches to nanofabrication: molding, printing, and other techniques," Chemical reviews, 105(4), 1171-1196 (2005).

[63] H. Lee and G. Y. Jung, "Full wafer scale near zero residual nano-imprinting lithography using UV curable monomer solution," Microelectronic Engineering, 77(1), 42-47 (2005).

[64] A. T. Cannistra, M. K. Poutous, E. G. Johnson, and T. J. Suleski, "Performance of conformal guided mode resonance filters," Optics Letters, 36(7), 1155-1157 (2011).

[65] D. Malacara, [Optical shop testing], Wiley-Blackwell, 2007.

[66] A. Davies, B. Bergner, and N. Gardner, "Measurement advances for micro-refractive fabrication," Proc. SPIE 5858, 58580P (2004).

[67] S. Reichelt, A. Bieber, B. Aatz, and H. Zappe, "Micro-optics metrology using advanced interferometry," Proc. 5856, 437-446 (2005).

[68] Y. Xia, E. Kim, X. M. Zhao, J. A. Rogers, M. Prentiss, and G. M. Whitesides, "Complex optical surfaces formed by replica molding against elastomeric masters," Science, 273(5273), 347 (1996).

[69] J. H. Chang, F. S. Cheng, C. C. Chao, Y. C. Weng, S. Y. Yang, and L. A. Wang, "Direct imprinting using soft mold and gas pressure for large area and curved surfaces," Journal of Vacuum Science & Technology A: Vacuum, Surfaces, and Films, 23, 1687 (2005).

[70] A. T. Cannistra, P. Srinivasan, E. G. Johnson, and T. J. Suleski, "Microtransfer molding of SU-8 micro-optics," Proc. SPIE 6883, 68830C (2008).

[71] T. T. Truong, R. Lin, S. Jeon, H. H. Lee, J. Maria, A. Gaur, F. Hua, I. Meinel, and J. A. Rogers, "Soft lithography using acryloxy perfluoropolyether composite stamps," Langmuir, 23(5), 2898-2905 (2007).

[72] H. Sung-Hoon, H. A. N. Kang-Soo, H. Kyeong-Jae Byeon, and C. Kyung-Woo, "Fabrication of sub-100 nm sized patterns on curved acryl substrate using a flexible stamp," Japanese Journal of Applied Physics, 47(5), 3699-3701 (2008).

[73] O. M. Efimov, L. B. Glebov, and H. P. Andre, "Measurement of the induced refractive index in a photothermorefractive glass by a liquid-cell shearing interferometer," Applied Optics, 41(10), 1864-1871 (2002).

[74] M. Nordstrom, J. Hubner, and A. Boisen, "Sloped side walls in SU-8 structures with 'Step-and-Flash' processing," Microelectronic Engineering, 83(4-9 SPEC ISS), 1269-1272 (2006).

[75] Micro-chem, http://www.microchem.com/products/su_eight.htm.

[76] U. S. Precision-Lens, [The Handbook of Plastic Optics], Cincinnati, U.S. Precision Lens, Inc., 1983.

[77] S. Jeon, D. J. Shir, Y. S. Nam, R. Nidetz, M. Highland, D. G. Cahill, J. A. Rogers, M. F. Su, I. F. El-Kady, C. G. Christodoulou, and G. R. Bogart, "Molded transparent photopolymers and phase shift optics for fabricating three dimensional nanostructures," Optics Express, 15(10), 6358-6366 (2007).

[78] W. Hu, B. Yang, C. Peng, and S. W. Pang, "Three-dimensional SU-8 structures by reversal UV imprint," Journal of Vacuum Science and Technology B: Microelectronics and Nanometer Structures, 24(5), 2225-2229 (2006).

[79] K.-H. Jeong, J. Kim, and L. P. Lee, "Biologically inspired artificial compound eyes," Science, 312(5773), 557-561 (2006).

[80] C. Becnel, Y. Desta, and K. Kelly, "Ultra-deep x-ray lithography of densely packed SU-8 features: I. An SU-8 casting procedure to obtain uniform solvent content with accompanying experimental results," Journal of Micromechanics and Microengineering, 15(6), 1242-1248 (2005).

[81] R. J. Jackman, T. M. Floyd, R. Ghodssi, M. A. Schmidt, and K. F. Jensen, "Microfluidic systems with on-line UV detection fabricated in photodefinable epoxy," Journal of Micromechanics and Microengineering, 11(3), 263-269 (2001).

[82] S.-I. Chang and J.-B. Yoon, "Shape-controlled, high fill-factor microlens arrays fabricated by a 3D diffuser lithography and plastic replication method," Optics Express, 12(25), 6366-6371 (2004).

[83] M. V. Kunnavakkam, F. M. Houlihan, M. Schlax, J. A. Liddle, P. Kolodner, O. Nalamasu, and J. A. Rogers, "Low-cost, low-loss microlens array fabricated by soft-lithography replication process," Appl. Phys. Lett., 82, 1152-1154 (2003).

[84] A. Fernandez, H. T. Nguyen, J. A. Britten, R. D. Boyd, M. D. Perry, D. R. Kania, and A. M. Hawryluk, "Use of interference lithography to pattern arrays of submicron resist structures for field emission flat panel displays," Journal of Vacuum Science & Technology B: Microelectronics and Nanometer Structures, 15(3), 729-735 (1997).

[85] Q. Xie, M. H. Hong, H. L. Tan, G. X. Chen, L. P. Shi, and T. C. Chong, "Fabrication of nanostructures with laser interference lithography," Journal of Alloys and Compounds, 449(1-2), 261-264 (2008).

[86] R. R. Agayan, W. C. Banyai, and A. Fernandez, "Scaling behavior in interference lithography," Proc. The International Society for Optical Engineering 3331, 662-672 (1998).

[87] S. T. Thurman and G. M. Morris, "Controlling the spectral response in guided-mode resonance filter design," Applied Optics, 42(16), 3225-3233 (2003).

[88] C. L. Hsu, Y. C. Liu, C. M. Wang, M. L. Wu, Y. L. Tsai, Y. H. Chou, C. C. Lee, and J. Y. Chang, "Bulk-micromachined optical filter based on guided-mode resonance in silicon-nitride membrane," Journal of Lightwave Technology, 24(4), 1922 (2006).

[89] R. Magnusson, Y. Ding, K. J. Lee, D. Shin, P. S. Priambodo, P. P. Young, and T. A. Maldonado, "Photonic devices enabled by waveguide-mode resonance effects in periodically modulated films," Nano- and Micro-Optics for Information Systems, Proc. SPIE 5225, 20-34 (2003).

[90] K. J. Lee, D. Wawro, P. S. Priambodo, and R. Magnusson, "Agarose-Gel Based Guided-Mode Resonance Humidity Sensor," Sensors Journal, IEEE, 7(3), 409-414 (2007).

[91] P. Srinivasan, M. K. Poutous, Z. A. Roth, Y. O. Yilmaz, R. C. Rumpf, and E. G. Johnson, "Spatial and spectral beam shaping with space-variant guided mode resonance filters," Optics Express, 17(22), 20365-20375 (2009).

[92] A. K. Kodali, M. Schulmerich, J. Ip, G. Yen, B. T. Cunningham, and R. Bhargava, "Narrowband Midinfrared Reflectance Filters Using Guided Mode Resonance," Analytical chemistry, 82(13), 5697-5706.

[93] C. L. Hsu, M. L. Wu, Y. C. Liu, Y. C. Lee, and J. Y. Chang, "Flattened broadband notch filters using guided-mode resonance associated with asymmetric binary gratings," Photonics Technology Letters, IEEE, 18(24), 2572-2574 (2006).

[94] D. W. Dobbs, I. Gershkovich, and B. T. Cunningham, "Fabrication of a graded-wavelength guided-mode resonance filter photonic crystal," Applied Physics Letters, 89, 123113 (2006).

[95] S. H. Douglas, "Laser damage threshold measurements of microstructure-based high reflectors," Proc. SPIE 7132, 71321K (2008).

[96] J. Limpert, T. Schreiber, and A. Tünnermann, "Fiber based high power laser systems," Encyclopedia of laser physics and technology, (2010).

[97] J. Nilsson and D. N. Payne, "High-Power Fiber Lasers," Science, 332(6032), 921 (2011).

[98] T. Sumiyoshi, H. Sekita, T. Arai, S. Sato, M. Ishihara, and M. Kikuchi, "High-power continuous-wave 3-and 2- m cascade Ho3+: ZBLAN fiber laser and its medical applications," Selected Topics in Quantum Electronics, IEEE Journal of, 5(4), 936-943 (1999).

[99] K. Bizheva, B. Považay, B. Hermann, H. Sattmann, W. Drexler, M. Mei, R. Holzwarth, T. Hoelzenbein, V. Wacheck, and H. Pehamberger, "Compact, broad-bandwidth fiber laser for sub-2-μm axial resolution optical coherence tomography in the 1300-nm wavelength region," Optics Letters, 28(9), 707-709 (2003).

[100] R. A. Sims, Z. Roth, T. McComb, L. Shah, V. Sudesh, P. Menelaos, E. Johnson, and M. C. Richardson, "Guided mode resonance filters as stable line-narrowing feedback elements for Tm fiber lasers," CLEO, Proc. Optical Society of America, CThN2 (2009).

[101] D. D. Gill, W. C. Sweatt, A. A. Claudet, V. C. Hodges, M. J. Vasile, and D. P. Adams, "Design and Manufacturing of Complex Optics: The Dragonfly Eye Optic," Sandia Report: SAND2007-0127, (2007).

[102] Z. Y. Yang, M. Zhao, N. L. Dai, G. Yang, H. Long, Y. H. Li, and P. X. Lu, "Broadband Polarizers Using Dual-Layer Metallic Nanowire Grids," Photonics Technology Letters, IEEE, 20(9), 697-699 (2008).

[103] J. J. Wang, F. Walters, X. Liu, P. Sciortino, and X. Deng, "High-performance, large area, deep ultraviolet to infrared polarizers based on 40 nm line/78 nm space nanowire grids," Applied Physics Letters, 90(6), 061104 (2007).

[104] Ö. Sepsi, I. Szanda, and P. Koppa, "Investigation of polarized light emitting diodes with integrated wire grid polarizer," Optics Express, 18(14), 14547-14552.

[105] K. E. Paul, M. Prentiss, and G. M. Whitesides, "Patterning Spherical Surfaces at the Two-Hundred-Nanometer Scale Using Soft Lithography," Advanced Functional Materials, 13(4), 259-263 (2003).

[106] T. W. Odom, J. C. Love, D. B. Wolfe, K. E. Paul, and G. M. Whitesides, "Improved pattern transfer in soft lithography using composite stamps," Langmuir, 18(13), 5314-5320 (2002).

[107] A. T. Cannistra, "Characterization of hybrid molding and lithography for SU-8 micro-optical components," M.S. Thesis, Optical Science and Engineering, UNC Charlotte, Charlotte, (2008).

[108] J. M. Gere and S. P. Timoshenko, [Mechanics of materials], Pacific Grove, Brooks Cole, 2001.

[109] G. G. Denisov, S. V. Kuzikov, and M. E. Plotkin, "Study of Talbot Effects in a Bent Waveguide with Constant Curvature," Journal of Infrared, Millimeter and Terahertz Waves, 30(4), 349-356 (2009).

[110] R. R. Boye and R. K. Kostuk, "Investigation of the effect of finite grating size on the performance of guided-mode resonance filters," Applied Optics, 39(21), 3649-3653 (2000).

[111] K. R. Hiremath, "Coupled mode theory based modeling and analysis of circular optical microresonators," Ph.D. Dissertation, University of Twente, (2005).

[112] J. J. Wang, W. Zhang, X. Deng, J. Deng, F. Liu, P. Sciortino, and L. Chen, "High-performance nanowire-grid polarizers," Optics Letters, 30(2), 195-197 (2005).

[113] N. P. Pham, T. L. M. Scholtes, R. Klerks, E. Boellaard, P. M. Sarro, and J. N. Burghartz, "Direct spray coating of photoresist–a new method for patterning 3-D structures," Proc. European Conference on Solid-State Transducers, XVI 182-185 (2002).

[114] L. Yu, Y. Y. Lee, F. E. H. Tay, and C. Iliescu, "Spray coating of photoresist for 3D microstructures with different geometries," Proc. IOP Publishing 34, 937 (2006).

[115] G. P. Nordin, J. T. Meier, P. C. Deguzman, and M. W. Jones, "Micropolarizer array for infrared imaging polarimetry," JOSA A, 16(5), 1168-1174 (1999).

[116] S. S. Sethi, R. G. Distasio, D. H. Ziger, J. E. Lamb Iii, and T. D. Flaim, "Use of antireflective coatings in deep-UV lithography," Proc. SPIE 1463, 30 (1991).

[117] Kydex, http://www.kleerdex.com/briefs/124.pdf.

[118] Optical-components, http://www.optical-components.com/optical-materials.html.

[119] K. M. Choi and J. A. Rogers, "A photocurable poly(dimethylsiloxane) chemistry designed for soft lithographic molding and printing in the nanometer regime," Journal of the American Chemical Society, 125(14), 4060-4061 (2003).

[120] S. W. Lee and S. S. Lee, "Shrinkage ratio of PDMS and its alignment method for the wafer level process," Microsystem Technologies, 14(2), 205-208 (2008).

[121] M. D. Austin, H. Ge, W. Wu, M. Li, Z. Yu, D. Wasserman, S. A. Lyon, and S. Y. Chou, "Fabrication of 5 nm linewidth and 14 nm pitch features by nanoimprint lithography," Applied Physics Letters, 84, 5299 (2004).

[122] K.-d. Kim, J.-h. Jeong, Y.-s. Sim, and E.-s. Lee, "Minimization of residual layer thickness by using the optimized dispensing method in S-FILTM process," Microelectronic Engineering, 83(4-9 SPEC ISS), 847-850 (2006).

[123] C. Wohlfarth, "Refractive index of cyclopentanone," in Refractive Indices of Pure Liquids and Binary Liquid Mixtures (Supplement to III/38), 2008, pp. 243-243.

[124] C. Chung and M. Allen, "Uncrosslinked SU-8 as a sacrificial material," Journal of Micromechanics and Microengineering, 15(1), 1-5 (2005).

APPENDIX A: SU-8 MOLDING CHARACTERIZATION

A.1 Overview

Understanding the effects of the molding process on SU-8 is necessary to optimize performance of molded micro-optical components, and also to enable fabrication of more complex micro-optics through subsequent lithographic processing of molded structures. This appendix describes characterization and fabrication processes developed to create hybrid SU-8 micro-optics leveraging methods of soft lithography [5]. For the characterization in this appendix, we focus primarily on hard backed (HB) PDMS mold templates, but the results are predominantly applicable to flexible techniques as well. Polymer shrinkage, molding resolution, and changes in lithographic properties as a result of the molding process are investigated. SU-8 replicas show high fidelity, small residual layers, and photosensitivity retention at the wafer level. Hybrid processes combining molding and lithographic exposure are demonstrated to realize proof of concept hierarchical structures, including submicron scale gratings on refractive microlens surfaces, and three-dimensional mesh microlenses. The methods described in this appendix form the basis for fabricating specific hierarchical systems discussed in the dissertation.

A.2 Polymer shrinkage characterization

A study of the shrinkage and expansion of PDMS and SU-8 is needed as size and duty cycle of features for micro-optics affect their functionality. Zygo scanning white light interferometer (SWLI) measurement values taken of PDMS mold templates were 4.11% smaller than master features. Measurements of SU-8 replica features were 3.17%

smaller than master features, leaving them 0.94% larger than PDMS mold template features. Zygo SWLI height measurements of master, mold and SU-8 replica of an eight level staircase structure are shown in Fig A-1. Measurements were taken of an original PDMS mold template and multiple SU-8 replicas over several molding cycles to determine dimensional behavior for multiple processing cycles. As shown in Fig A-2, there is a slow decrease in the PDMS and SU-8 vertical feature heights as more replica cycles are performed, though a decreasing rate of change is observed.

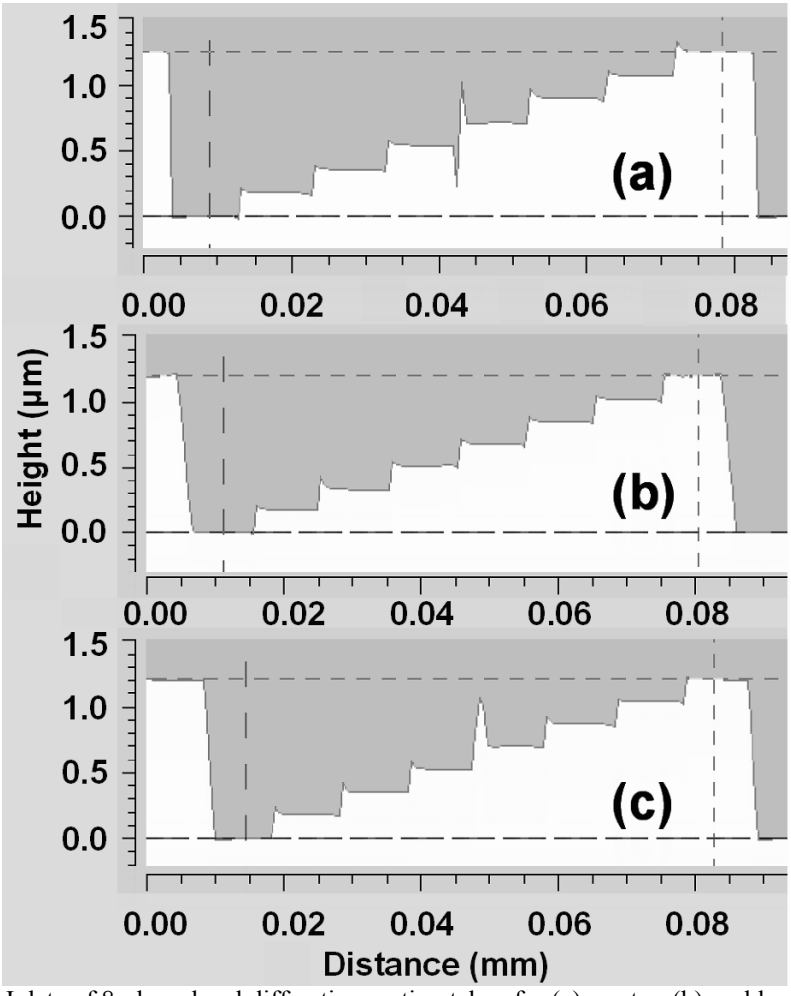

Fig A-1. SWLI data of 8-phase level diffractive grating taken for (a) master, (b) mold, and (c) replica, showing high molding fidelity.

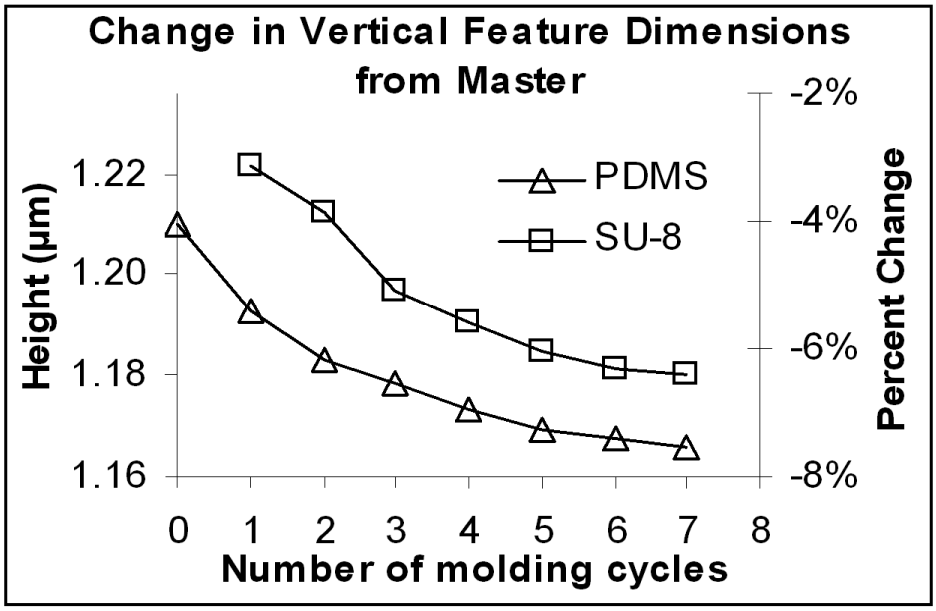

Fig A-2. Vertical feature size variation as function of number of molding cycles for PDMS mold, and corresponding SU-8 replica. A decrease in mold template dimensions is observed after each mold cycle, however the reduction in feature sizes decreases over continued use.

To explain the dimensional variation, several factors were taken into account. As the temperature of a material changes, materials expand or contract as a function of their coefficient of thermal expansion (CTE) [117]. While substrates such as fused silica have relatively low CTE values (0.54 ppm/°C [118]), polymers, such as PDMS and SU-8, have much higher CTE values, 310 ppm/°C and 50 ppm/°C respectively. Values calculated from the CTE imply PDMS mold templates generated at 70 °C should be 1.55% smaller than the master when measured at 20 °C. Because the PDMS mold template will swell when molding SU-8 at 95 °C, CTE calculations suggest replicated SU-8 features measured at 20 °C will be 0.41% larger than those on the corresponding PDMS mold template.

In addition to CTE as a cause of dimensional variation, polymers tend to shrink as they harden or crosslink. It is commonly reported that shrinkage of around 1% occurs as a result of PDMS fully crosslinking after molding has taken place [119]. Variation in mix

ratio for the two part elastomer can increase this effect by an additional 1% for an otherwise identical molding process [120]. This shrinkage occurs after the molded pattern has been generated, resulting in shrinkage that is in addition to that sustained by CTE variation. Therefore, combining these sources of shrinkage with CTE calculations can account for up to a 3.55% decrease in PDMS features to master features when measured at 20 °C. Sources of dimensional variation, in particular the cause of shrinkage of PDMS over several molding cycles, are not fully understood. However their consistency suggests characterization is possible and therefore processes can be adjusted to account for and correct dimensional error.

A.3 Molding resolution characterization

Depending on the material used and how it is processed, limitations may exist for the smallest features achievable through replication. Quantifying this resolution limit gives a greater understanding of a polymer's possible applications. Molding of features to below 10 nm has been achieved with multiple molding techniques and polymers [60, 121, 122]. However, little research has been performed on the limits with molding of SU-8. A nanoimprint molding template from the Molecular Imprints Inc. (MII) Imprio 100™ at UNC Charlotte containing sub-100 nm features was used to produce a master element of molded monomer on a 100 mm silicon wafer. A PDMS replica of this patterned wafer was then fabricated and used to mold the patterns into SU-8 using the hard-backed molding process. Series 2002 SU-8 was spun on a 100 mm silicon wafer at 3000 RPM for 60 seconds to generate a SU-8 thickness around 2 μm. Scanning electron microscope (SEM) images of successfully molded 90 nm posts and 100 nm lines are shown in Fig

A-3. While these tests are not exhaustive and do not define a lower size limit for SU-8 replication, they do indicate that nano-scale patterns are readily achievable in SU-8.

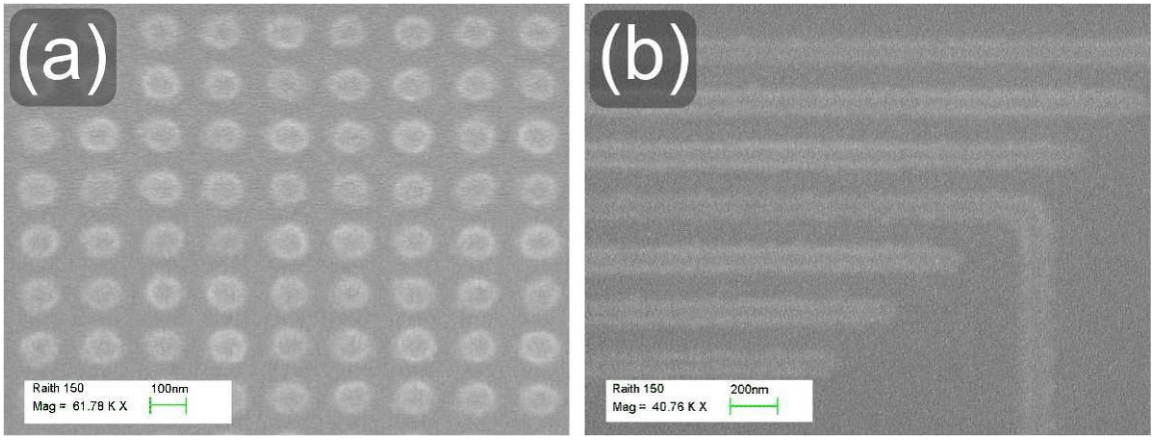

Fig A-3. SEM images of (a) 90 nm posts, and (b) 100 nm lines molded in SU-8.

A.4 Characterizing deviation from conventional processes

During the SU-8 softbake, solvent evaporation is a function of time and temperature. The solvent level should be monitored throughout the molding process to determine if there is a significant change following the conventional softbake (CSB). Solvent levels affect exposure dose, lithographic resolution, material strength, crack formation and the ability to develop the material. 10 μm thick layers of SU-8 on silicon wafers were monitored for weight variation. These wafers were then measured using a Sartorius BL60S scale with a repeatability of 0.1 mg. The results showed a 6.31% reduction in weight as a result of the initial softbake, followed by no significant change with additional bakes (less than ± 0.2%). This suggests solvent content will not be a major factor in SU-8 photolithography after molding.

The refractive index of SU-8 changes as the material crosslinks and solvent content varies. Crosslinking of SU-8 can occur during extended thermal exposure [80]. Our HB molding process uses conventional softbaking, but does subject SU-8 to additional

thermal exposure. This implied a need to monitor the refractive index of the resist as a function of our molding process. A JA Woolem VASE ellipsometer was used to measure the refractive index of SU-8 after resist spin, conventional softbake, and at various points through the molding process (Fig A-4). Silicon wafers were coated with Series 2000.5 SU-8 by spin coating with a top speed of 2000 RPM for 60 seconds to produce a thickness of 600 nm. After spin coating, the wafers were conventionally softbaked on a hot plate for 1 min at 95°C. Following the CSB, the wafers were baked inside an oven at 95°C with measurements taken at 15 min intervals. Multiple areas were measured on a single wafer. Significant variation was noticed between pre-softbake and post-softbake values with an increase in refractive index from 1.6031 to 1.6110 (an increase of 0.0079 at 500 nm), probably a result of reduction of the lower index cyclopentanone solvent (n=1.43494, [123]) through evaporation. Refractive index measurements taken after subsequent baking times showed little significant change, and variations on the order of the estimated precision of the measurement process (0.0006). This implies minimal solvent content change or thermal crosslinking. The measurements remained consistent across the spectrum of measured wavelengths. This data suggests that the additional thermal processing from our molding process has minimal effects on the refractive index of SU-8.

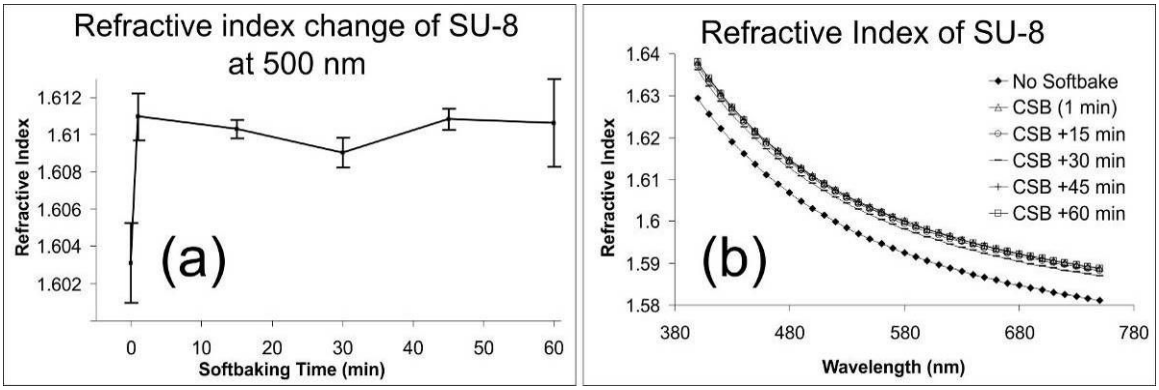

Fig A-4. Refractive index of 600 nm thick SU-8 layer on a silicon wafer undergoing increased thermal exposure in addition to conventional softbake (CSB) as experienced during molding. Ellipsometer measurement at (a) 500 nm showing little change after CSB, and (b) from 400 nm – 900 nm, showing consistent values across the spectrum.

Although no significant change in the post molded SU-8 was observed in weight or refractive index, additional characterization of the pre and post molded resist was performed to demonstrate the ability for hybrid combinations of molding and subsequent lithographic processing of SU-8. Wafers were coated with 7 μm of SU-8. One wafer was then soft-baked conventionally as given in the data sheet by Microchem (2 min 30 sec at 95° C). Another wafer was soft-baked conventionally and then molded with the blank PDMS template using the HB molding process described previously. Both wafers were then exposed for a dose of 145 mJ using an I-line Quintel model 4000 contact aligner with a chrome on glass binary lithographic mask. Features that were resolved with the conventional process are seen to be very similar to post molded structures, as seen in Fig A-5. The results show that little change occurs in the resolution ability of SU-8. These results corroborate previous data showing little change in SU-8 due to the molding process. Although contact lithography has its own exposure limitations, these results signify an ability to incorporate molded and lithographic features for hybrid processing with limited optimization of exposure and development of molded SU-8.

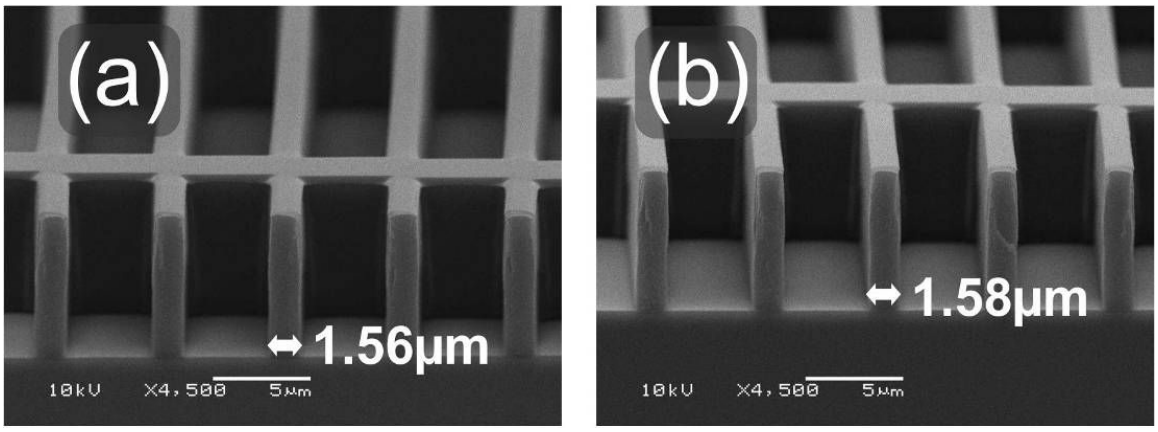

Fig A-5. Comparison of features from lithographic exposure in 7 µm thick (a) conventionally processed SU-8 and (b) post molded SU-8.

A.5 Results and discussion

Combining molding techniques with photolithographic processing offers many possibilities for functional integration and miniaturization of optical micro-systems [77]. With care in processing steps, SU-8 can be used to implement this combination of fabrication processes. Bake temperatures over 120 °C were avoided altogether, as this will thermally crosslink SU-8, disabling selective development [124]. Methods of interference lithography and a mask-based angled exposure process were used to demonstrate the possibilities of hybrid molding and lithographic processing.

As discussed in Chapter 2, interference lithography uses interference of multiple coherent laser beams to create a varying irradiance profile for use as the exposure mechanism for photoresist [43]. This process produces periodic structures over large areas with large depth of field, making it an excellent candidate for exposing resist structures containing topography. An expanded, collimated argon laser source operating at 364 nm was used at an angle $\theta = 20$ degrees to expose SU-8, producing gratings of 530 nm period while still maintaining a large exposure area. Molded resist volumes in the form of spherical and cylindrical refractive microlenses were exposed and developed

using this technique (Fig A-6). The interferometric exposure crosslinked the internal volumes of molded resist, but surface modulation (though limited to 100-200 nm) remained. This hybrid process could be used to generate similar micro-lenses with modulated surface relief to serve, for example, as an anti-reflective coating.

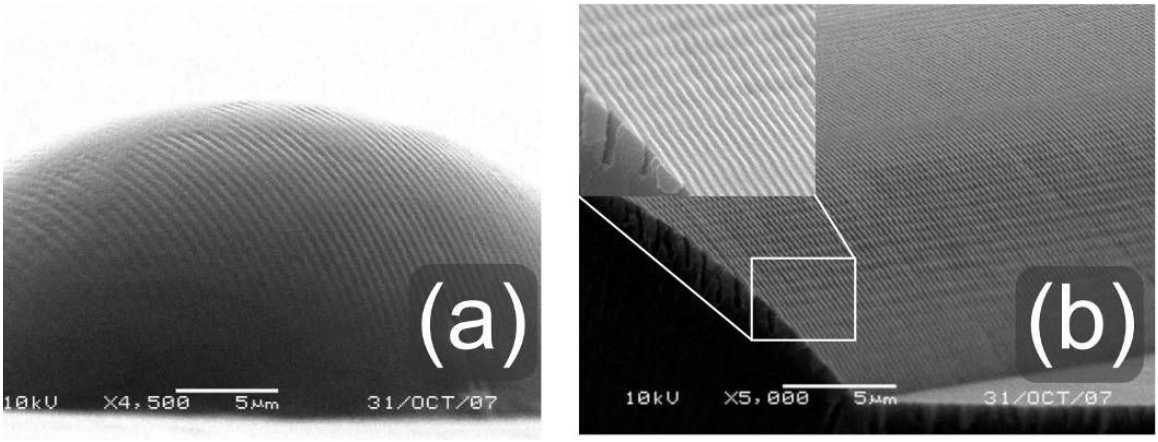

Fig A-6. SEM images of molded SU-8 (a) spherical and (b) cylindrical lenses incorporating submicron surface gratings through interferometric exposure.

Additional process development was needed to internally selectively expose a molded resist volume for 3D structures. In particular for SU-8 microlenses, molded surface topography can refract the light intended to expose the resist. To minimize this effect, an improvised setup using glycerol (n=1.473) as an index matching fluid was created to reduce the effects of the surface topography. Using a binary mask, molded SU-8 was exposed at a 45° angle by a collimated 363.8 nm Argon laser source, and then rotated and exposed at -45°, then the exposed resist was developed. Fig A-7 shows the mesh patterns generated by crossing exposure through a 9 µm period hole array mask overlaid onto the molded lens structure. The index matching fluid was observed to reduce refraction of the lens during exposure, and the individual angled posts retain the lens geometry. These results further illustrate the types of hierarchically structured micro-

optics and devices that can be created through the hybrid processing schemes that we have discussed.

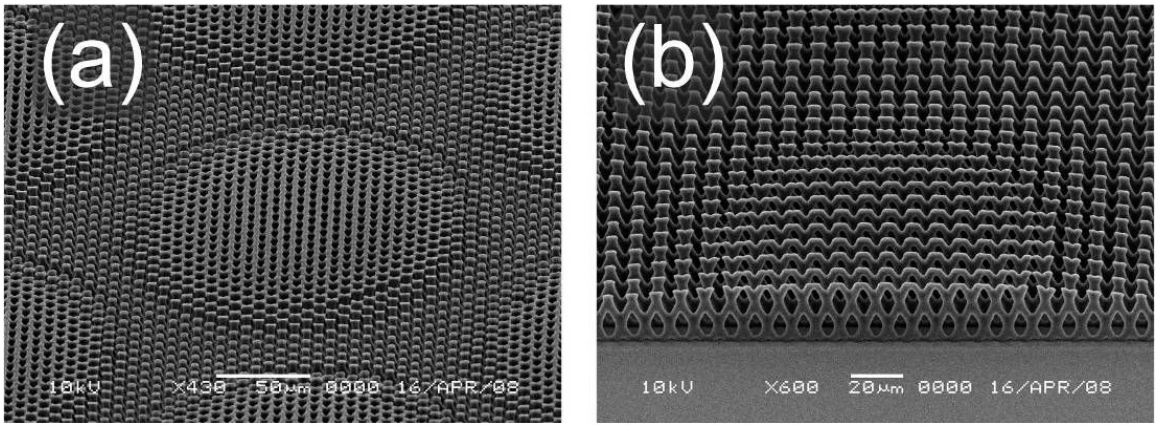

Fig A-7. SEM images of (a) spherical SU-8 microlens array and (b) single lens cross section fabricated through molding and subsequent angled mask exposures with an index matching liquid.

The Molded SU-8 micro-optics discussed in this appendix, including diffractive and refractive elements, have shown high fidelity, optical surfaces over a range of designs and dimensions. We show that with respect to mold fidelity, polymer shrinkage and expansion play roles in determining the final size of molded elements, due to coefficient of thermal expansion, crosslinking effects, and mold lifetime characteristics. By understanding these effects, adjustments can then be made to correct for sources of replicated feature variation. No significant changes in SU-8's photolithographic properties were evident from measurements of weight and refractive index of molded SU-8. Molded SU-8 was then subjected to lithographic evaluation, and showed lithographic resolution similar to conventionally processed SU-8. These results form the basis of hierarchical designs fabricated in Chapters 3 and 4. Multiplexing of micro-molding and lithographic patterning of SU-8 was also demonstrated, offering additional

possibilities for functional integration and miniaturization of 3D optical micro-systems and components.

APPENDIX B: CHARACTERIZATION OF GMR MEASUREMENT SETUP

To establish comparable values for measurements taken off flat and curved substrates, we characterized the test setup for system losses. The test setup was first configured with the output of the tunable laser connected to the input of the circulator, and the measurement end of the circulator was connected to a FC/PC to FC/APC patch cable "A" which was then connected to a gold terminated fiber as shown in Fig B-1. The gold tipped fiber is used by a Luna Optical Backscatter Reflectometer as a reference cable. Loss points are illustrated in red. The average reflectivity measured over the range of wavelengths was 66.5% or -1.769 dB.

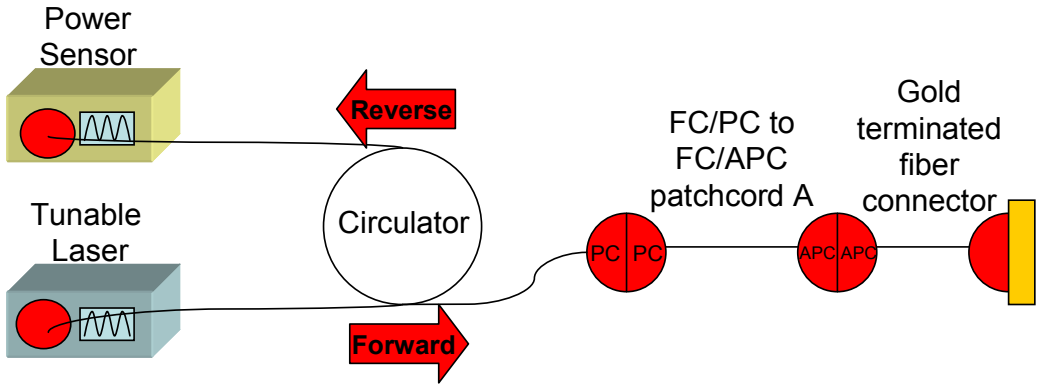

Fig B-1. Diagram of test setup terminated with reference cable to quantify system loss.
The measurement end of the circulator was then disconnected from the FC/PC to

FC/APC patchcord "A" (which was connected to the gold terminated fiber connector cable) and connected to the FC/PC to FC/APC patchcord "B" installed in the curved GMR measurement setup (a different patchcord modified to mount into the curved GMR setup must be used) as shown in Fig B-2. The average reflectivity measured over the range of wavelengths was 64.9% or -1.882 dB. A graph comparing the reflectivity of the

gold terminated cable and the curved gold mirror is shown in Fig B-3. The average reflectivity measured off the gold mirror is -0.113 dB less than the gold terminated fiber.

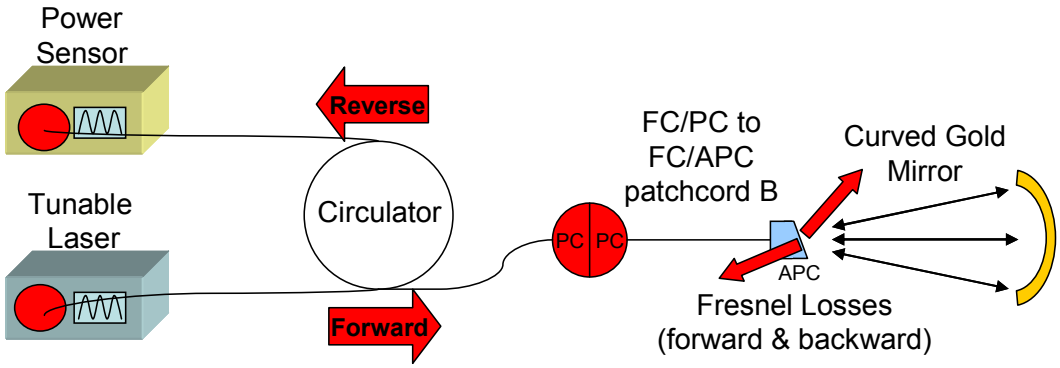

Fig B-2. Test setup with gold terminated reference cable replaced with FC/APC terminated fiber illuminating concave gold mirror.

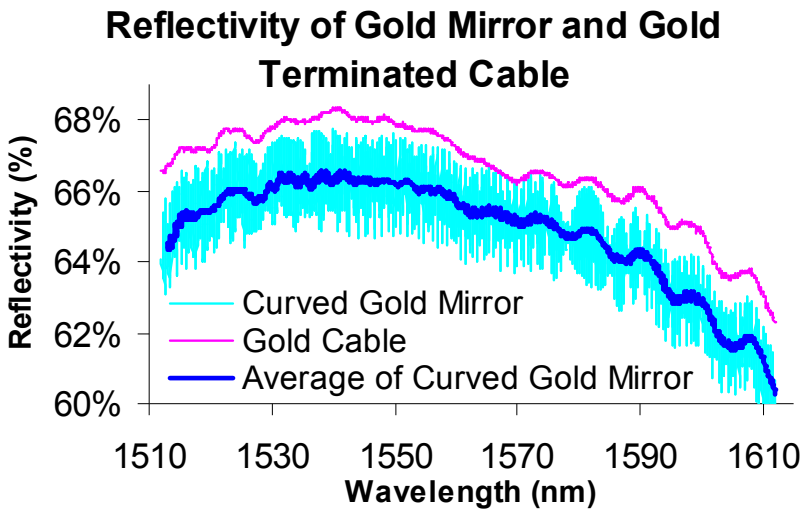

Fig B-3. Reflected power measured from gold terminated reference cable and concave gold mirror.

To quantify connector loss the setup was re-arranged to measure power loss when connecting the tunable laser directly to the power sensor with a single FC/APC to FC/PC patch cord. The average loss was -0.189 dB. Another patch cord was added to the setup to give a measured estimate of connector loss. The measured loss was -0.262 dB. A plot of the measured results is shown in Fig B-4. The average difference is 0.073 dB. The

nature of the FC connector allows for variation in connector loss dependent on how well the two surfaces make physical contact. This implies some uncertainty is introduced after any connections are made or broken in the system. Therefore this measured difference can only serve as a rough estimate for connector-based loss.

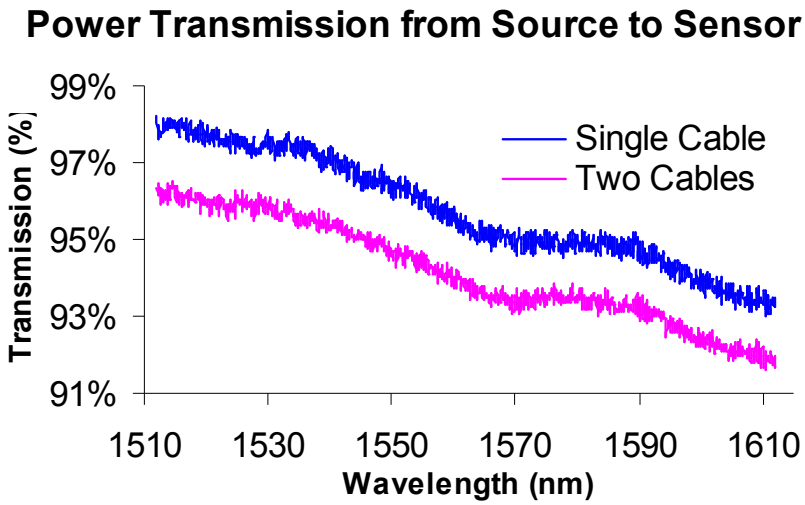

Fig B-4. Transmitted power measured when laser output is connected directly to power sensor.

By using an estimated connector loss of -0.073 dB (per pair of connectors) we can estimate the additional connector losses introduced when measuring the gold terminated fiber. If we assume light travels through the FC/APC connector of the gold terminated fiber, to the connectorized end coated with gold, and then back through both connectors, a total of 2 pair of connectors are added for a total estimated loss of -0.145 dB. By taking into account these additional connector losses of the gold terminated fiber setup and the Fresnel losses of the curved gold mirror setup we can make a better comparison of the two measurements (as given by the following loss budgets).

According to the data sheet, the insertion loss for the circulator in the forward direction is -0.7 dB, and -1 dB in the reverse direction. The calculated Fresnel loss from the angled cleave fiber used in the curved gold mirror test setup is -0.319 dB. The total

calculated loss is -2.019 dB or 62.8% neglecting other sources of loss. Measured values for both the gold terminated fiber and the curved gold mirror had values higher than this, suggesting a variation due to calibration of the tool. Despite this, the gold terminated fiber and curved gold mirror will both be scaled by the calibration error, leaving their comparisons intact.

A detailed table of measured values (and calculated values where using measured ones were not readily possible) used as a loss budget guide is shown in Table B-1. The "output and input" values correspond to loss when a cable is connected directly from source to sensor. Gold loss is calculated assuming 99% reflectivity. The difference in measured loss from estimated loss total of each arrangement is comparable with the curved gold mirror having 0.061 dB less measured loss than that of the gold terminated fiber using this method.

Table B-1:

Losses of every component for gold terminated fiber	dB	Losses of every component for curved gold mirror	dB	
Output and input	-0.189	Output and input	-0.189	
Circulator Forward	-0.7	Circulator Forward	-0.7	Calculated/ Datasheet
FC/PC to FC/PC	-0.0725	FC/PC to FC/PC	-0.0725	
FC/APC to FC/APC	-0.0725	FC/APC	-0.0363	
Gold termination	-0.0363	Fresnel Forward	-0.159	Measured
Gold Loss	-0.0437	Gold Loss	-0.0437	
Gold termination	-0.0363	Fresnel Reverse	-0.159	Combined
FC/APC to FC/APC	-0.0725	FC/APC	-0.0363	
FC/PC to FC/PC	-0.0725	FC/PC to FC/PC	-0.0725	
Circulator Reverse	-1	Circulator Reverse	-1	Difference of Fiber - Mirror =
Estimated Loss Total	-2.2952	Estimated Loss Total	-2.4682	0.173
Measured Loss	-1.769	Measured Loss	-1.882	0.113
Difference from est.	0.5262	Difference from est.	0.5862	

Table B-2 estimates a loss budget using only calculated values or values found in literature/data sheets. The change from the previous table is the value used for connector loss. The lowest value given by any available specification for connector loss was given to be -0.1 dB (value closest to that measured). By using this value (a change of only -0.03 dB from the measured estimate) the difference in measured loss from estimated loss total of each arrangement is reduced to only 0.005 dB (or 0.12%). This suggests that the uncertainty in connector loss combined with a calibration error (probably around 0.57 dB) is a very possible explanation for discrepancies between the estimated loss budget values and measured values.

Table B-2:

Losses of every component for gold terminated fiber	dB	Losses of every component for curved gold mirror	dB	
Output and input	-0.1	Output and input	-0.1	
Circulator Forward	-0.7	Circulator Forward	-0.7	Calculated/ Datasheet
FC/PC to FC/PC	-0.1	FC/PC to FC/PC	-0.1	
FC/APC to FC/APC	-0.1	FC/APC	-0.05	
Gold termination	-0.05	Fresnel Forward	-0.159	Measured
Gold Loss	-0.0437	Gold Loss	-0.0437	
Gold termination	-0.05	Fresnel Reverse	-0.159	Combined
FC/APC to FC/APC	-0.1	FC/APC	-0.05	
FC/PC to FC/PC	-0.1	FC/PC to FC/PC	-0.1	
Circulator Reverse	-1	Circulator Reverse	-1	Difference of Fiber - Mirror =
Estimated Loss Total	-2.3437	Estimated Loss Total	-2.4617	0.118
Measured Loss	-1.769	Measured Loss	-1.882	0.113
Difference from est.	0.5747	Difference from est.	0.5797	